eman ta zabal zazu

Universidad del País Vasco
Euskal Herriko Unibertsitatea

Fabrication and Near-Field Characterization of Mid-Infrared Transmission Lines

Paulo Sarriugarte Onandia

PhD Thesis

Supervisor: Rainer Hillenbrand

2017

Laburpena

Argi infragorria, materialen konposizio kimikoa edo egitura bezalako propietateak aztertzeko erabili ohi da, espektroskopia infragorria, kimikan, biologian eta materialen zientzian ezinbesteko tresna bihurtzeraino. Hala ere, ohiko mikroskopia eta espektroskopia infragorriek uhin elektromagnetiko hedakorrak erabiltzen dituzte eta honek, beren bereizmen espaziala uhin luzera erdi ingurura mugatzen du difrakzio efektuaren eraginez. Infragorri ertainarentzat, bereizmen espazila 5-10 μm ingurukoa da, laginak nanoeskalan aztertzea eragotziz.

Difrakzio muga gainditzeko era bat irrati-uhin teknologiako antena eta transmisiolerro (TL) kontzeptuak argi ikuskor eta infragorriaren maiztasunetara transferitzea da. Antenek erradiazio elektromagnetikoa jaso eta biziki indartutako eta uhin-luzerapeko neurrietara murriztutako eremuetan bihur dezakete. TLak berriz, antenak jaso eta murriztutako erradiazioa era eraginkorrean garraiatzeko diseinatutako gailuak dira. Gaitasun hauek erregimen infragorrian erabili ahal izateko, antena eta TLak miniaturizatu eta maiztasun infragorrietan jarduteko egokitu behar dira. Alabaina, erronka esanguratsuak ageri dira antena eta TL kontzeptuak irrati maiztasunetatik maiztasun infragorrietara transferitzeko. Erronka nagusia, metalek irrati-uhinekiko eta argi infragorriarekiko duten erantzun desberdinean datza. Izan ere, metalek eroankortasun elektriko urria dute maiztasun infragorrietan, irrati maiztasuneratan ordea, eroale elektriko perfektutzat jo daitezke. Azken urteotan lan teoriko gutxi batzuek, irrati-uhin teknologiako oinarrizko kontzeptuak argi ikuskor eta infragorriaren maiztasunetara nola transferitu ikertu dute. Honen adibide garrantzitzuak dira antena optikoetan aplikatutako karga eta inpedantzia kontzeptuak edota antena optikoen eskalatze legea. Gainera, esperimentalki erakutsi da miniaturizatutako TLetan argi infragorri ertaina akoplatzea posible dela. Hala ere, TLetan akoplatutako argi infragorriaren hedapena arakatu gabeko gaia da oraindik.

Tesi honetan zehar, infragorrirako antena eta TLak fabrikatu ditugu, eta transmisio-moduko sakabanaketa motako eremu-hurbileko eskaneatze mikroskopio optikoa (transmisio-moduko s-SNOM) erabiliz karakterizatu. Antena dipolar baten bitartez bi kabledun TLetara argi infragorri ertaina aklopatu dugu eta bere hedapen propietateak ikertu ditugu, hala nola, eremuaren indartze lokala, eremu murrizketa, modoaren uhin luzera (eraginkorra) eta hedapen luzera. Horrez gain, aurrenekoz argi infragorrira egokitutako Arkimedesen kiribil antenak bezalako antena egitura konplexuak aztertu ditugu eremu hurbileko mikroskopiaz. Antena hauek irrati-uhin teknologian ezagunak diren banda zabaleko uhin hedakor motako antenak dira. Arkimedesen kiribil antenak eta bestelako egitura bidimentsionalak aztertzeko, nanoGUNEn genuen transmisio-moduko s-SNOM konfigurazioa aldatu dugu laginak zirkularki polarizatutako argiaz kitzikatzea ahalbidetu dezan. Esperimentalki lortu diren antena eta TLen eremu hurbilaren distribuzioak balioztatzeko FDTD eta FDFD simulazioak egin ditugu, simulazioetatik lortutako eremu hurbilaren distribuzioak esperimentalki lortutakoekin bat datozela berretsiz.

Tesi hau sei kapitulutan bananduta dago.

Lehenengo kapituluan irrati-uhin teknologiako antena eta TL kontzeptuak aurkezten dira. Antenen teorian oinarrituta, infragorrira egokitu ditugun egituren (bi kableko TLak, antena dipolar linealak eta Arkimedesen kiribil antenak) funtzionamendu printzipioak azaltzen dira. Irrati maiztasunetarako sortutako antena eta TLen diseinuak maiztasun infragorrietara egokitzeko hain beharrezko diren metalen propietate optikoen deskripzio labur bat ere ematen da Drude-Sommerfeld ereduan oinarrituta.

Bigarren kapituluak, infragorrirako antena eta TLen karakterizaziorako erabili den teknika nagusia aurkezten du: transmisio-moduko sakabanaketa motako eremu-hurbileko eskaneatze mikroskopio optikoa (transmisio-moduko s-SNOM). Teknika esperimental honek egitura plasmonikoetan ageri diren eremu hurbilaren distribuzioak irudikatzea ahalbidetzen du bereizmen espazial nanometrikoaz. Kapitulu honetan, s-SNOMaren funtzionamendu printzipioak azaltzen ditugu, transmisio-moduko s-SNOMean sakonduz eta bien arteko desberdintasunak aipatuz. Konfigurazio esperimentalean egindako hobekuntzak ere lantzen dira eta transmisio-moduko s-SNOMaren inplementazio gisa, egitura hedatuekin burututako esperimentuen bi adibide erakusten dira.

Hirugarren kapituluan, erabilitako substratuak TLetan akoplatutako argi infragorriaren hedapen propietateetan duen eragina aztertzen da. Honek, euskarri bezala

erabiltzen den substratua era egokian aukeratzen lagunduko digu, eta horrela aurretik fabrikatutako infragorrirako TLak hobetzea ahalbidetu. Kaltzio fluorurozko (CaF_2) substratuetan fabrikatutako TLetan argi infragorriaren hedapen luzera bikoiztu egiten dela aurkitu dugu, siliziozko (Si) substratuetan fabrikatutakoekin alderatuz. Hedapen luzeraren bikoizketa, CaF_2-ak duen errefrakzio indize baxuagoren (Si-a baino) ondorioa da. Frogatu dugunez, CaF_2 substratuetan fabrikatutako TLen bukaera pixkanaka estutuz (ikus 1 Irudia) bertan hedatzen den argi infragorria nanofoka daiteke. Horrez gain, esperimentalki baieztatu dugu CaF_2 substratuetan fabrikatutako TLetan lortutako nanofokuan argi infragorriaren intentsitatea lau aldiz indartsuagoa dela. Beti ere Si substratuan lortutakoarekin alderatuz.

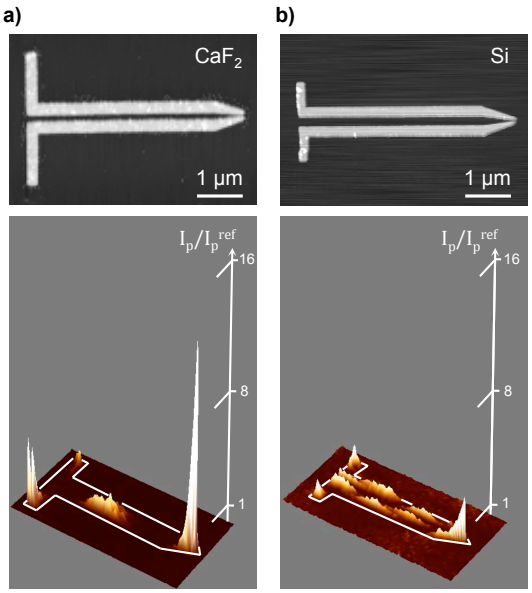

1 Irudia: **Argi infragorriaren nanofokatzea mutur estutudun TLen bidez.** **(a)** CaF_2 substratuan fabrikatutako mutur estutudun TLaren topografia irudia (goian) eta eremu hurbilaren intentsitatea $I_p = |E_p|^2$ (behean). **(b)** Aurreko ataleko berdina Si substratuan fabrikatutako mutur estutudun TLarentzat.

Laugarren kapituluan, tesfokai honetan zehar substratu isolatzaileetan egitura plasmoniko funtzionalak fabrikatzeko garatu den estrategia berri bat aukezten da. Fabrikazio estrategia berri honek fokatutako ioi izpien (FIB) bidezko ehoketa darabil eta elektroi izpi bidezko litografiaz (EBL) fabrikatzerakoan dauden berezko arazoei aurre egiteko garatu da. Esaterako, bi kable paralelodun TLak fabrikatzean, kable paraleloak banantzen dituen tarte estu eta luzeak lortzea eragozten du EBL fabrikazio teknikak. Estrategia berria, ehoketa-pauso anitzez dago osatua, ehotzen den gainazala lurrari konektatuta dagoelarik ehotu bitartean. Honek, egitura polikristalinodun urre

geruza ehotzeko fabrikazio parametro egokiak erabiliaz, EBL bidez ezin lor genitzakeen Arkimedesen kiribil antenak eta tarte estu eta luzedun TLak fabrikatzea ahalbidetzen du.

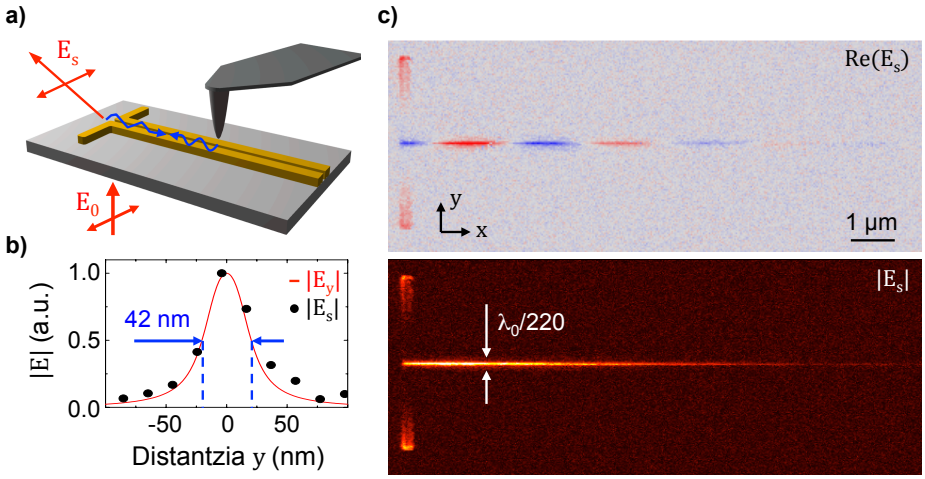

2 Irudia: **Eremu hurbileko neurketa s-polarizaziorako (E_s).** **(a)** Esperimentuaren eskema. **(b)** Kalkulatutako (marra) eta esperimentuko (puntuak) datuak $D_m = 42$ nm lortzeko. **(c)** Eremu hurbilaren irudiak E_s-ren zati erreala (goian) eta amplitudea (behean) 25 nm-ko tartedun TLarentzat.

Bostgarren kapituluan garatu berri den fabrikazio estrategia darabilgu, Galio eta Helio ioien izpi bidezko ehoketa konbinatuz, 25 nm eta 5 nm-ko tartedun urrezko TL funtzionalak fabrikatzeko CaF_2 substratu isolatzailean. Argi infragorria horren tarte txikidun TLetara akoplatuz, TL modoaren murrizketa espazialaren eta era berean argi infragorria espazialki hain mugatuta hedatzearen mugak arakatzea zen helburua. Horrez gain, murriztuta hedatzen den TL modoaren propietateak (hedapen luzera, uhin luzera, hedapen abiadura) ikertzea ere bagenuen xedetzat. Transmisio-moduko s-SNOMa erabiliz, argiaren polarizazio ezberdinetarako interferometrikoki aztertu ditugu TLak eta espazio errealean irudikatu ditugu uhin infragorriaren hedapena eta murrizketa. Lortutako eremu hurbilaren irudiek TLak funtzionalak direla frogatzen dute eta esperimentalki baieztatzen dute TLetan zehar hedatzen den modoaren uhin-luzerapeko murrizketa. Esate baterako, 42 nm-tako modo diametroa (erabilitako argi infragorriak hutsean duen uhin luzera baino 220 aldiz txikiagoa) eta 10 μm inguruko hedapen luzera erakutsiz (ikus 2 Irudia). Gainera, s-polarizazioko argia detektatzean s-SNOMaren bidezko irudikapen kontraste berri bat aurkitu eta azaldu dugu: eremu hurbilak sakabanatzeko darabilgun puntak islagailu lokal bezala jokatzen du TL modoa antenarantza islatuz honek igor dezan (ikus 2 Irudia).

Seigarren kapituluan ezker- (LCP) eta eskuinetara (RCP) zirkularki polarizatutako argiaz kitzikatutako Arkimedesen kiribil antenak eta metagainazal lauak aztertzen dira. Transmisio-moduko s-SNOMak, nanoegitura bidimentsionalen eremu hurbilaren irudiak zuzenean eta espazio errealean lortzea ahalbidetzen duela frogatu dugu. Aztertutako kiribil antenek eta metagainazal lauek LCP eta RCP argiarekiko erakusten dituzte. Lortutako eremu hurbilaren irudietatik erantzun erantzun desberdin hauen jatorri mikroskopioaren xehetasunak aurki ditzakegu. Hala nola, dikroismo zirkular mespretxagarria (esanguratsua) duten metagainazal lauek, eremu hurbileko kontraste kiral mespretxagarria (esanguratsua) dutela aurkitu dugu. Bestalde, polarizazio zirkularrarekiko nanofokatze selektiboa aurrenekoz bistaratu dugu Arkimedesen kiribil antenetan (ikus 3 Irudia). Efektu hau antena teoria kontuan izanik, antenan eragiten den uhin hedakorren kitzakapen direkzionalaz baliatuz azaldu dugu.

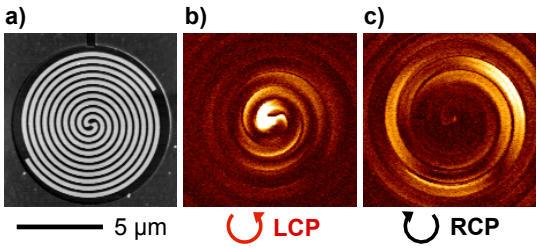

3 Irudia: **5 biratako Arkimedesen kiribil antena. (a)** Topografia irudia. Antena LCP **(b)** eta RCP **(c)** argiarekin kitzikatzean hartutako eremu hurbilaren (E_p) irudiak non kiribilaren zentrua ikus daitekeen.

Summary

Infrared light is widely used to study different material properties such as chemical composition or the structure of matter. Infrared (IR) spectroscopy is thus an important analysis tool in materials sciences, chemistry and biology. However, conventional IR microscopy and spectroscopy use propagating electromagnetic waves to study the samples, which limits the spatial resolution because of diffraction to about half of the wavelength. In the mid-IR spectral range, the spatial resolution is of about 5-10 μm, which prevents studies on the nanometer scale.

A recent trend to circumvent the diffraction limit is to transfer radio-wave technology concepts such antennas and transmission lines (TLs) into IR and visible frequency regimes. Antennas are able to capture electromagnetic radiation and to convert it into fields that are strongly enhanced and confined on the deep subwavelength scale. TLs are designed to transport the radiation captured and confined by antennas in an efficient way. In order to transfer these capabilities to the IR regime, antennas and TLs need to be miniaturized and adapted to operate at IR frequencies. However, there are also significant challenges for the transfer of antenna concepts from RF to IR frequencies. The main challenges arise from the different response of metals to electromagnetic radiation in RF and IR frequencies. While metals are commonly assumed as perfectly conductors at RF, at IR frequencies their conduction is rather poor in comparison. In recent years, few theoretical works have investigated how to transfer basic RF concepts to the IR and visible regimes. Important examples are the application of concepts such as antenna loading and antenna impedance to optical antennas and the scaling law for optical antennas. Furthermore, it has been also shown that mid-IR light can be coupled to miniaturized TLs. However, the propagation of IR light on TLs is still widely unexplored.

During this thesis, we fabricated IR antennas and TLs, and characterized them by transmission-mode scattering-type scanning near-field optical microscopy (transmission-mode s-SNOM). By means of dipolar antennas we coupled mid-IR light into two-wire TLs and we investigated propagation properties such as local field enhancement, field confinement, mode (effective) wavelength or propagation length. In addition, we studied for the first time more complicated antenna structures such as Archimedean spiral antennas, which are well-know travelling wave broadband antennas for radio-wave technology. To that end, we modified the transmission-mode s-SNOM setup available at nanoGUNE to be able to illuminate the samples with circularly polarized light. In order to support the experimentally obtained near-field distributions, we have performed FDTD and FDFD simulations, which are in excellent agreement with the experimental data.

This thesis is divided into 6 chapters.

Chapter 1 introduces antenna and TL concepts in radio-wave technology. Based in antenna theory, the working principles of the structures that are adapted to IR frequencies (two-wire TLs, linear dipole antennas and Archimedean spiral antennas) are presented. A brief description of optical properties of metals, based on Drude-Sommerfeld model is also given, which is fundamental to transport antenna and TL designs for radio frequencies to the IR regime.

Chapter 2 describes the main technique employed to characterize IR antennas and TLs during this thesis: transmission-mode scattering-type scanning near-field optical microscope (transmission-mode s-SNOM). This technique provides both nanoscale optical resolution and allows imaging the near-field distribution on plasmonic structures. In this chapter we explain the general working principles of s-SNOM and differences with transmission-mode s-SNOM. We present the improvements carried out in the setup and we present two examples of the implementation of transmission-mode s-SNOM on extended structures.

Chapter 3 investigates the effect of the substrate on the propagation properties on IR light coupled to TLs. In this way we can improve the already implemented IR TL by choosing an adequate supporting substrate. We find that IR light propagates twice as long as on TLs fabricated on CaF_2 compared to TLs on Si, due to the lower refractive index of CaF_2. We demonstrate that tapered TLs on CaF_2 nanofocus IR light at the taper apex and experimentally verify that a stronger local field enhancement is

obtained compared to tapered TLs on Si.

Chapter 4 presents a new fabrication strategy developed during the thesis to fabricate functional plasmonic structures on insulating substrates by focused ion beam (FIB) milling. The need to develop a new fabrication strategy arose from the impracticality of electron beam (e-beam) lithography to fabricate TL with high aspect ratio (long and narrow) gaps. The new strategy consists of multi-step milling process that keeps the exposed area grounded while being milled, which in combination with optimized parameters for structuring polycrystalline gold, allows fabricating functional spiral antennas and TLs with high aspect ratio gaps that we could not get by e-beam lithography.

Chapter 5 exploits the newly developed fabrication strategy combining Gallium and Helium ion beam milling to fabricate TLs with gap widths down to 5 nm. By coupling IR light into TLs with such small gaps we aimed to explore the limits of channeling extremely confined IR light and investigate the propagation properties (propagation length, mode wavelengths, propagation velocity) of such confined modes. We apply interferometric and polarization-resolved transmission-mode s-SNOM to image in real space the propagation and confinement of the TL modes. Obtained near-field images demonstrate that the TLs are functional and experimentally verify extreme subwavelength-scale infrared guiding with a mode diameter of about 30 nm (310 times smaller than the wavelength λ_0 of the incident light) and a propagation length of about 4 μm. We also discover and describe a new image contrast mechanism in s-SNOM when s-polarized light is detected: we conclude that the tip acts as a local reflector of the TL mode, which is then scattered via the antenna.

Chapter 6 studies Archimedean spiral antennas and planar metasurfaces which are excited with left- (LCP) and right-handed circularly polarized (RCP) light. We demonstrate that the near-field distributions in extended two-dimensional nanostructures can be mapped directly and in real space with transmission-mode s-SNOM. Acquired near-field images provide insights into the microscopic origin of the different optical response to LCP and RCP light of the studied spiral antennas and planar metasurfaces. We find that metasurfaces with negligible and strong circular dichroism have a negligible and strong chiral optical near-field contrast. We visualize, for the first time, the circular-polarization selective nanofocusing of infrared light in Archimedean spiral antennas, and explain this chiral optical effect by directional launching of travelling waves.

Contents

Chapter 1

Introduction

Infrared light is widely used to study different material properties such as chemical composition or the structure of matter [1, 2]. Infrared (IR) spectroscopy is thus an important analysis tool in materials sciences, chemistry and biology. However, conventional IR microscopy and spectroscopy use propagating electromagnetic waves to study the samples, which limits the spatial resolution because of diffraction to about half of the wavelength. In the mid-IR spectral range, the spatial resolution is of about 5-10 μm, which prevents studies on the nanometer scale [3, 4].

An efficient route to circumvent the diffraction limit is based on plasmonic antennas [5, 6] and plasmonic waveguides [7–9]. Plasmonic antennas make use of localized surface plasmon (LSP) resonances to efficiently convert free-space radiation into nanoscale-confined and strongly enhanced near fields, also called hot spots or nanofoci [10], and vice versa. This capability has been essential, among others, in applications such as surface enhanced Raman spectroscopy (SERS) [11] of even single molecule [12–14], surface and antenna-enhanced IR absorption spectroscopy (SEIRA) [15, 16] and nanoscale resolved Fourier transform IR spectroscopy (nano-FTIR) [17]. Alternatively, nanofocusing of light can be achieved by adiabatic compression of surface plasmon polaritons (SPPs) propagating on tapered metal nanowires [18–22] or slot waveguides [23–26], yielding a strongly concentrated field at the taper apex. The strongly confined SPP modes could find application for guiding of light on the nanoscale and in integrated plasmonics circuits [27] where SPPs are the carriers of information. At THz frequencies, where surface plasmon polaritons are generally weakly bound, specialized geometries such as corrugated metal nanowires [28, 29], coaxial waveguides [30] or two-

wire transmission lines [31,32] improve the confinement of the SPPs, while allowing for mode propagating over several micrometers.

Many of the above mentioned principles are analogous to telecommunication technology, where the interaction between electromagnetic waves and antennas has been widely studied. In communication applications, the antennas are used to emit or receive electromagnetic waves on the radio frequency (RF) range, from about 3 kHz up to hundreds of GHz. The antennas are able to convert the electromagnetic waves travelling in free space into electric currents which are then transported through transmission lines (TLs) to the receiver (e.g. a TV) [33]. As IR light is also part of the electromagnetic spectrum (from about 1 THz up to 400 THz), in principle it should be possible to adapt RF antennas and TLs to IR frequencies. However, the metals at RF behave has nearly perfect conductors, while in IR frequencies metals show much poorer conduction properties. As a consequence, one needs to take into account the optical response of metals at IR frequencies in order to translate RF antenna concepts into the IR frequency range. Prominent examples of concepts that have been transferred from RF to IR and visible frequency regimes are the scaling law for optical antennas [6], the application of concepts of antenna loading and antenna impedance of an optical antenna [34] and the miniaturization of TLs to obtain functional IR TLs [31,32].

This Chapter gives a short introduction on basic antenna theory concepts and a brief overview on the optical response of metal nanoparticles. The Chapter follows the introductory chapters of ref. [35], which is mainly based on textbooks and handbooks [33,36,37].

1.1 Antennas and transmission lines

Along the last century, a complete theoretical framework called antenna theory has been developed to analyse, design and characterize RF antennas and TLs [33]. Based on antenna theory, we present in the following the well-known working principles of RF antenna and TL designs (two-wire TLs, linear dipole antennas and Archimedean spiral antennas) which in this thesis were adapted to mid-IR frequencies.

1.1.1 Transmission Lines

Transmission lines (TLs) are the components that transport RF currents fed by an electric device (e.g. a generator) to the antenna, where they are radiated into free space [33]. They are also used for the inverse process, i.e. to transport the electromagnetic energy captured by the antenna to a receiver [37]. The simplest approach is to use a single metallic wire coated by a dielectric, called Goubau line (G-lines) [38]. The dielectric coating maintains the energy propagating on the wire entrained [37]. However, the G-lines are not practical because they tend to radiate when the wire is bended sharply or external objects are placed on the line. In order to prevent radiation loses, TLs such as two-wire TLs (Fig. 1.1a) or coaxial lines [37] are used. With these type of TLs, the electromagnetic field from each wire is balanced by the field of the other, which results in a zero radiation from the wires [35]. Nowadays the most commonly used TLs in RF technology are coaxial cables, while in former times two-wire TLs were use to transport TV and radio signals [33]. The simplicity of the two-wire TL converts it in a perfect candidate to bring the TL concept to the nanoscale.

The two-wire TL consists of two parallel metal wires separated by a dielectric space (e.g. air) between them (Fig. 1.1a) [33,37]. When an alternate current generator is connected to one end of the TL (left side of Fig. 1.1a), an electromagnetic wave is launched in each wire. While the electromagnetic wave propagates along the wires, the associated current on the wires oscillates accordingly. In Fig. 1.1a the instantaneous direction of the currents along the wires are illustrated by black arrows. The distance along the wires between neighbouring positions with the same instantaneous current defines one wavelength λ (see Fig. 1.1a). Because the wires are driven with oppositely oscillating alternate current, the associated electromagnetic mode that is generated in the TL is antisymmetric. This means that the current flow generated at the wires is opposite to each other for every cross section along the wires, i.e. the current in one wire oscillates 180° out of phase with respect to the current on the other one (see Fig. 1.1a). When the distance between the wires is kept sufficiently small (less than 1% of the free-space wavelength), a nearly complete cancellation of the radiating electromagnetic fields can be achieved [35,37]. Thus the TL does not radiate [33]. However, close to the wires (at a distance of the order of the separation between the wires), the fields created by the local charge flow do not cancel each other [39]. These are the so-called evanescent fields or near fields, which will be briefly introduced and compared to radiating fields (so called far fields) in Section 1.2.

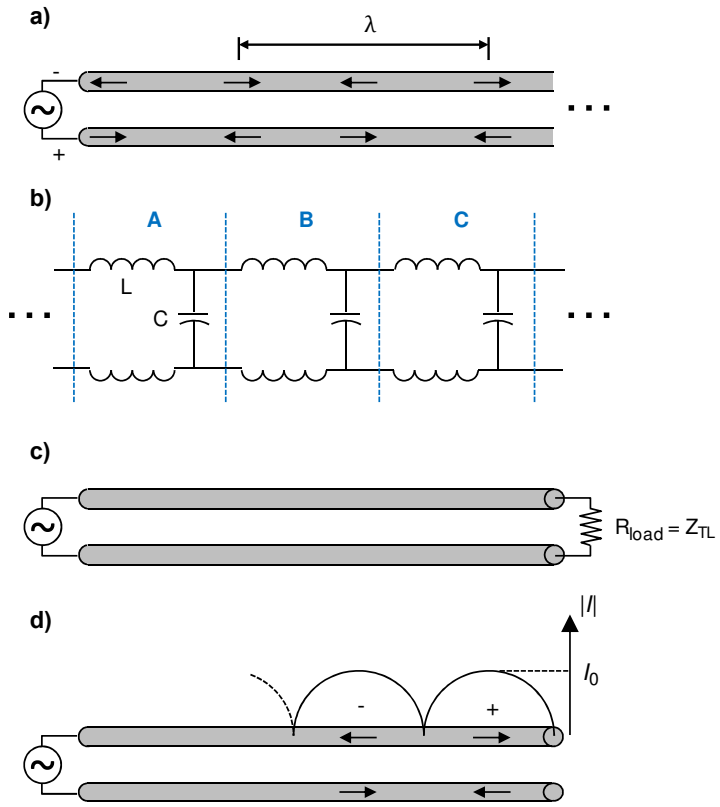

Figure 1.1: **Two-wire TLs.** **(a)** Instantaneous current on a two-wire TL, the arrows mark the direction and position of the maximum current at the plotted instant of time. **(b)** Equivalent circuit for an ideal TL of impedance Z_{TL}. **(c)** Two-wire TL terminated with a resistive load. **(d)** Open ended two-wire TL. Adapted from [37], taken from [35].

In order to understand the working principle of the TLs, let us consider an ideal TL, i.e. a TL with neither resistive nor radiative losses ($R = 0$). When a generator applies a voltage to an ideal TL, the obtained current is not infinite as one could expect form the Ohms law ($I = V/R$) because the TL, although ideal, has an impedance Z_{TL}. As a consequence, the current on the TL depends on the applied voltage and on the impedance of the TL. Assuming $R = 0$, the TL can be described by a series of inductors of inductance L and capacitors of capacitance C: each wire section contribute to the inductance, due to self inductance and the coupling between each pair of neighbouring wire sections contribute to the capacitance, due to their opposite instantaneous charge densities. Thus, each section of the TL can be described by a pair of inductors and a capacitor (illustrated in Fig. 1.1b). In this picture, an electromagnetic wave propagating along the TL is represented by a power transfer from one section to its adjacent section (i.e. from A to B, from B to C and so on) [35]. When the TL is infinitely long, the

power is transferred only in one direction, away from the source [37]. For an ideal TL, the characteristic impedance Z_{TL} is given by [37]

$$Z_{\mathrm{TL}} = \sqrt{L/C} \tag{1.1}$$

where L and C are the inductance and capacitance, respectively, per unit length of TL [37]. Note that the impedance of a lossless TL is purely real valued [37]. Z_{TL} depends on the TL's cross sectional geometry because the inductance L decreases with increasing wire diameter, and the capacitance C decreases with increasing spacing between the wires. Thus, a TL with small separation between thick wires has a relatively small impedance, while a TL with large separation between thin wires has a large impedance [37]. The impedance of a TL can be measured, for example via the voltage-to-current-ratio at the generator. Practical values of Z_{TL} range from about 200 Ω to 800 Ω for two-wire TLs, and from 30 Ω to 100 Ω for coaxial cables [37].

When the TLs have resistive loses ($R \neq 0$), their characteristic impedance Z_{TL} is complex valued and according to the distributed model of a TL [40] is given by

$$Z_{\mathrm{TL}} = \sqrt{\frac{R + i\omega L}{G + i\omega C}} \tag{1.2}$$

where ω is the frequency of the current, R is the resistance per unit wire length and G is the conductance per unit length of the dielectric around the wires.

TLs have usually a finite length and they are terminated in a load to which the power is delivered (e.g. Fig. 1.1c). If the load matches the complex characteristic impedance Z_{TL} of the TL ($R_{\mathrm{load}} = Z_{\mathrm{TL}}$), the TL is said to be matched [37] and the current travelling along the TL finds that the load looks like an infinitely long TL of the same characteristic impedance [37] (Fig. 1.1c). Then, all of the power is dissipated in the load and the current in such a TL is equal to the applied voltage divided by the characteristic impedance [37]. If the load (Z_{load}) is not equal to Z_{TL}, the TL is said to be mismatched. As $Z_{\mathrm{TL}} \neq Z_{\mathrm{load}}$, the voltage-to-current-ratio (V/I) is also different in the TL and in the load. As a result, when the power being transported on TL reached the load, it is not totally absorbed but partially backreflected towards the generator [37]. The larger the mismatch between Z_{TL} and R_{load}, the larger is the percentage of the incident power that is reflected. In the extreme cases, where the load is zero (a short circuit, $R_{\mathrm{load}} = 0$) or infinity (an open circuit, $R_{\mathrm{load}} = \infty$), all of the power reaching

the end of the TL is backreflected. An open-circuited ideal TL is shown in Fig. 1.1d, where the current reaching the end of the TL exhibits a 180° phase shift in order to satisfy the zero-current condition at the open end [35]. As a consequence of the total back reflection, the current wave forms a standing wave pattern, which is illustrated in Fig. 1.1d.

1.1.2 Linear dipole antenna

A linear dipole antenna can be constructed by bending apart the wires of the open-circuited TL by 90° (Fig. 1.1d). In this configuration (see Fig. 1.2a), the radiation related to the currents along the bended wires does not cancel but reinforce each other [33]. Thus, the signal carried by the TL from a generator is radiated by the dipole antenna. Conversely, a free-space electromagnetic wave can generate currents in the antenna, which are then delivered by the TL to a receiver. Note that the standing wave pattern of the open-circuited TL in Fig. 1.1d is maintained in the antenna[1] [35].

The efficiency of the the radiation (and reception) of free space electromagnetic waves depends on the dipolar antenna's length l (measured from antenna end to end). For antenna lengths l equal or smaller than the wavelength λ ($l \leqslant \lambda$), the currents along both antenna arms points in the same direction (Fig. 1.2b,c). This implies that the segments of the antenna reinforce each others radiated fields in most directions [33,35]. The maximum radiation is achieved when the total length of the dipolar antenna l (Fig. 1.2c) is equal to the half of the wavelength λ, $l = \lambda/2$ [33]. For antenna lengths l larger than the wavelength λ ($l > \lambda$), the current standing wave pattern on the antenna arms undergoes a 180° jumps between adjacent half-cycles, i.e. every $\lambda/2$ distance starting from the antenna ends, yielding antenna segments where the current points in the opposite direction. This situation is illustrated in Fig. 1.2d for $\lambda < l < 3\lambda/2$. Hence, the segments with the current pointing in one direction do not reinforce the radiation from segments with the current pointing in the opposite direction. As a consequence, significant interference and cancelling effects occur in certain directions (see e.g. Fig. 1.3b) [33].

In Fig. 1.3 the pattern of the radiated power is compared for dipolar antennas with length $l = \lambda/2$ and $l = 5\lambda/4$ oriented vertically (z axis). It can be observed that both radiation patterns exhibits cylindrical symmetry around the antenna's long

[1] If the radius a of each wire is very small ($a \ll \lambda$), the standing wave pattern of the current along the antenna arms is sinusoidal with zero-current at the ends [33]

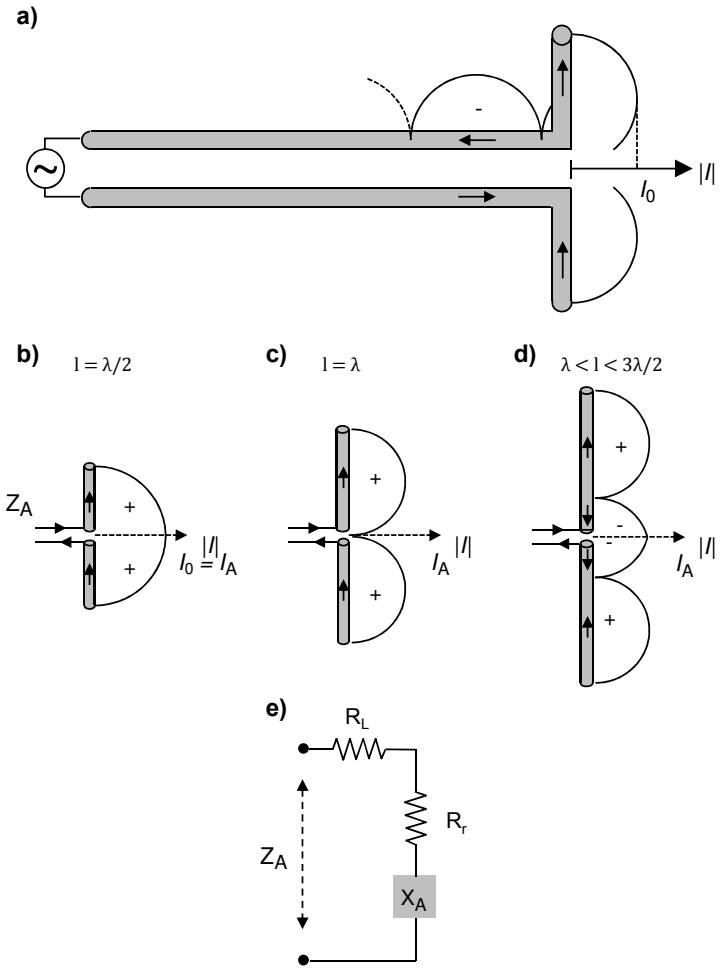

Figure 1.2: **Linear dipole antenna.** **(a)** Current distribution on a lossless bended two-wire TL forming a dipole antenna. Current standing wave patterns on linear dipole antennas of length **(b)** $l = \lambda/2$, **(c)** $l = \lambda$ and **(d)** $\lambda < l < 3\lambda/2$. **(d)** Illustration of antenna equivalent circuit. Adapted from [33], taken from [35].

axis, with a node on the radiation pattern along the symmetry axis. In the case of the antenna with $l = \lambda/2$ (Fig. 1.3a), one single lobe is observed, where the radiated power is maximum at the polar angle $\theta = 90°$ (in the xy plane). For the antenna with $l = 5\lambda/4$, the radiation pattern exhibits three lobes in the directions $\theta = 30°$, $\theta = 90°$ and $\theta = 150°$. The three lobes are separated by two nodes along directions $\theta \simeq 50°$ and $\theta \simeq 130°$, which are a consequence of the destructive interference of the radiated fields by antenna segments with opposite current flows.

One of the major characteristics to define an antenna is its self impedance Z_A, which is used to determine the efficiency of the antenna [33, 37]. The self impedance

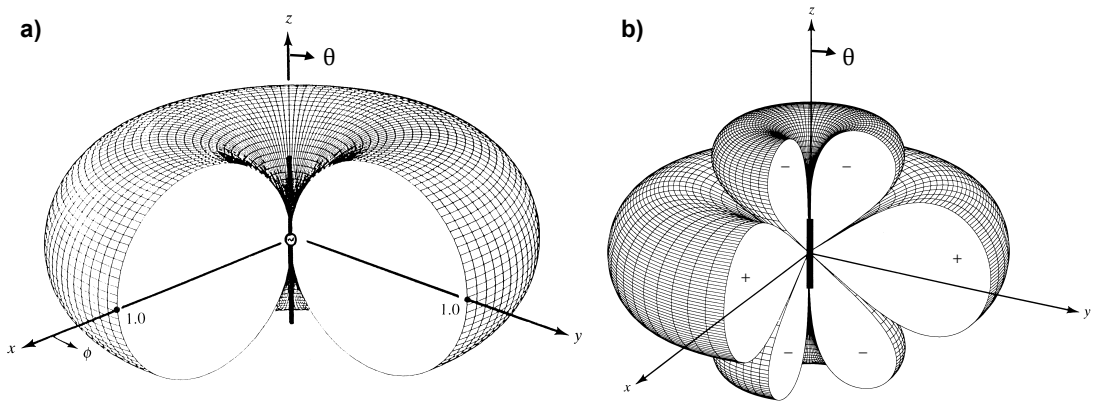

Figure 1.3: **Three-dimensional amplitude patterns for thin dipolar antennas.** Averaged Poynting vector integrated over a sphere of arbitrary radius r yielding the total power of radiated by the dipolar antennas. **(a)** Antenna of length $l = \lambda/2$ showing a single radiation lobe which is directed mainly along $\theta = 90°$ (on xy plane). **(b)** Antenna of length $l = 5\lambda/4$ showing one major lobe along $\theta = 90°$ and two minor lobes along $\theta = 30°$ and $\theta = 150°$. Taken from [33].

$Z_A = V_{\text{in}}/I_{\text{in}}$ is measured at the feed point of the antenna and is given by the ratio between the voltage applied at its feed point, V_{in}, and the current flowing into the feed point, I_{in} [33,37]. In order to account only the contributions of the antenna itself, Z_A is measured with the antenna located out of the influence of any other conductors. The antenna self impedance Z_A is composed by three impedance components, which are illustrated in Fig. 1.2e:

$$Z_A = R_A + iX_A = R_r + R_L + iX_A \tag{1.3}$$

The resistance R_r is called radiation resistance. It is related with the energy radiated by the antenna. The loss resistance R_L of the antenna is related with the energy dissipation in form of heating at the antenna and nearby dielectrics. The antenna resistance R_A is formed by the sum of both radiation and loss resistances, $R_A = R_r + R_L$ [33]. The antenna reactance X_A describes a possible inductive or capacitive behavior of the antenna and is related to the presence of resonances in the antenna [35]. When $X_A = 0$, the antenna is said to be in resonance and its impedance is purely resistive.

The antenna impedance Z_A of a linear dipole antenna strongly depends on the employed frequency. This dependence is observed in the expression of R_r and X_A shown in Eqs. 1.4 and 1.5, which are the result of an analytical treatment of the linear dipole antenna applying the induced EMF method. In this method, the electric and magnetic

fields of the dipole antenna are calculated assuming a zero antenna radius [33]. Then, the Poynting vector is integrated over a cylindrical surface that coincides with the actual antenna radius a [35]. As a result, the self impedance of the antenna $Z_A = R_r + iX_A$ (assuming a lossless antenna, i.e. $R_L = 0$) related to the current at the feed point of the antenna is obtained (see Eqs. 1.4 and 1.5) [33]. Note that the induced EMF method yields good results only for small radii (usually limited to $a < \lambda/200$), because for small antenna radii we can assume a sinusoidal standing wave pattern of the current along the antenna arms with zero-current at the antenna ends if the antenna is center fed and $a \ll \lambda$ [33]. A different method called Integral Equation-Moment Method can be used in order to obtain more accurate expressions for antennas with larger radii [33].

Applying the induced EMF method for a linear dipole antenna, the following expressions of R_r and X_A are obtained

$$\begin{aligned} R_r(k,l,\eta) = & \frac{\eta}{2\pi \sin\left(\frac{kl}{2}\right)^2} \Bigg\{ C + \ln(kl) - C_i(kl) \\ & + \frac{1}{2}\sin(kl)\left[S_i(2kl) - 2S_i(kl)\right] \\ & + \frac{1}{2}\cos(kl)\left[C + \ln\left(kl/2\right) + C_i(2kl) - 2C_i(kl)\right] \Bigg\} \end{aligned} \tag{1.4}$$

$$\begin{aligned} X_A(k,l,a,\eta) = & \frac{\eta}{4\pi \sin\left(\frac{kl}{2}\right)^2} \Bigg\{ 2S_i(kl) + \cos(kl)\left[2S_i(kl) - S_i(2kl)\right] \\ & - sin(kl)\left[2C_i(kl) - C_i(2kl) - C_i\left(\frac{2(ka)^2}{kl}\right)\right] \Bigg\} \end{aligned} \tag{1.5}$$

where $C = 0.5772$ is Euler's constant, k is the wave vector of the electromagnetic wave, l is the antenna length, a is the antenna radius, η the impedance of the surrounding medium (for free-space $\eta = 377\ \Omega$) and $C_i(x)$ and $S_i(x)$ are the cosine and sine integrals given by [33]

$$S_i(x) = \int_0^x \frac{\sin(\tau)}{\tau} d\tau \tag{1.6}$$

$$C_i(x) = -\int_x^\infty \frac{\cos(\tau)}{\tau} d\tau \tag{1.7}$$

In Fig. 1.4a the antenna impedance $Z_A = R_A + iX_A$ ($R_A = R_r$ as we assume $R_L = 0$) of linear dipole antenna is plotted as a function of antenna length l and for different antenna radius a [35]. Note that l and a are expressed in units of the wavelength λ. It can be observed that the antenna reactance X_A is zero at about $l = \lambda/2$, 1λ and $3\lambda/2$ which corresponds to half-wave, full-wave and 3/2-wave resonances of the linear dipole antenna. The half-wave and 3/2-wave resonances show a low antenna resistance R_A, while the full-wave resonance shows a infinite antenna resistance R_A because the denominator in Eq. 1.4 becomes zero. For a real dipolar antenna, this is not the case, but the antenna resistance R_A can still reach very high values [33, 35]. In general, the antenna resonances can be classified in odd resonances with a low antenna resistance R_A appearing near $l = (2n + 1)\,\lambda/2$ and in even resonances with a high antenna resistance R_A, appearing near $l = n\lambda$, where n is an integer number [35]. As the resonances with high R_A require high voltages to drive the antenna with sufficient power, the dipole antennas are usually operated at odd resonances, most often at half-wave resonance $l = \lambda/2$ due to its higher emission.

In order to visualize the influence of the antenna radius a, we show in Fig. 1.4b the antenna resistance R_A and reactance X_A reactance around the half-wave resonance length for the three antenna radii $a = 10^{-2}\lambda$, $10^{-3}\lambda$ and $10^{-5}\lambda$. For the antenna resistance R_A we observe a slowly increasing resistance for increasing relative length l/λ. Note that only one curve is shown for R_A because R_r is independent of the antenna radius a. The plot for the antenna reactance X_A shows three straight lines of different slopes. The thin antenna (blue curve) shows a steeper slope than the thick antenna (red curve), indicating that thin antennas have a sharper antenna resonance than thick antennas [35]. Surprisingly, the zero crossing of the antenna reactance X_A does not occur at $l = \lambda/2$ but for slightly smaller values, in the range between 0.45λ and 0.5λ (see Fig. 1.4b). The thinner the antenna is, the closer the antenna resonance is located to $\lambda/2$. The resonance only occurs exactly at $l = \lambda/2$ only for infinitely small antenna radii [37]. For odd resonances ($l \simeq (2n + 1)\,\lambda/2$), when the antenna length is smaller than the resonant length, X_A becomes negative meaning that the antenna has a capacitive reactance. On the contrary, when the antenna is longer than the resonant length, the antenna reactance becomes positive and hence, inductive [35]. As it can be observe in Fig. 1.4b, X_A is inductive for all three antenna radii at $l = \lambda/2$ where three lines coincide at reactance value of $X_A = 42.5$.

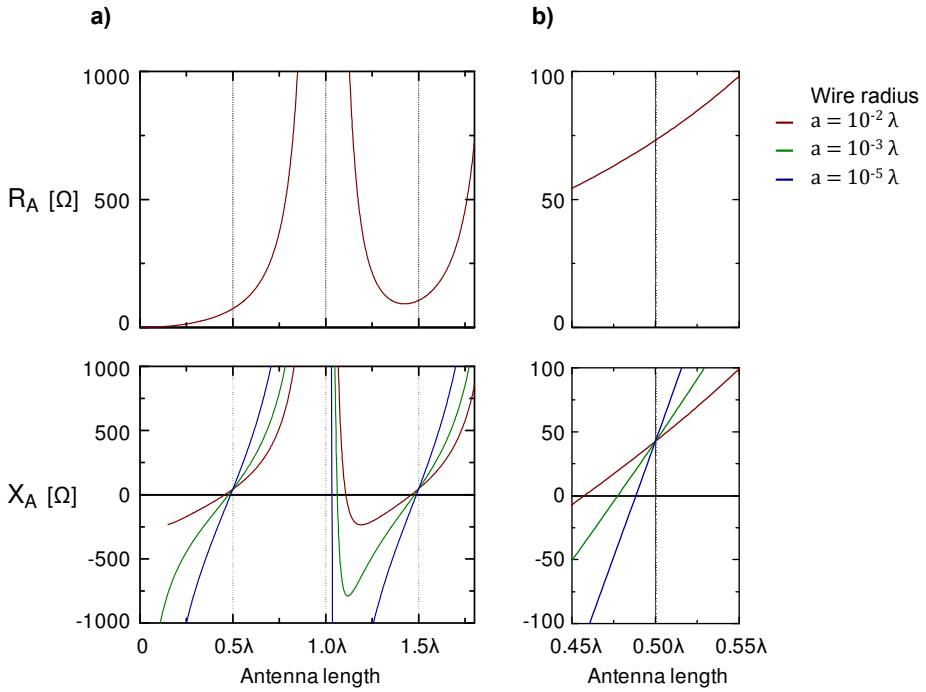

Figure 1.4: **Antenna resistance R_A and antenna reactance X_A of an ideal linear dipole antenna evaluated with Induced EMF Method.** **(a)** R_A and X_A is plotted as a function of antenna length l (in units of the wavelength λ in the range $0 \leqslant l \leqslant 1.8\lambda$. **(b)** same as **(a)**, but the antenna length is varied only around the first half-wave resonance at $\lambda/2$. There antenna resistance R_A and reactance X_A is plotted for three different antenna radii a. Note that $R_A = R_r$ as we assume loss resistance to be zero $R_L = 0$. Note also that all three curves coincide for R_A because R_r is not dependent on the radius a. Taken from [35].

1.1.3 Archimedean two-wire spiral antenna

An Archimedean two-wire spiral antenna [33,41,42] (see Chapter 6) can be constructed by winding a two-wire TL in a spiral shape as it is shown in Fig. 1.5. Spiral antennas are traveling wave antennas [33], i.e. the radiation is generated by propagating current along the folded wires, not by generating standing waves as dipolar antennas. Because of the spiral winding geometry, the two-wire TL transforms itself into a radiating structure, i.e. into an antenna [42].

In order to explain the working principle of an Archimedean two-wire spiral antenna, let us consider a two-wire TL wound in a spiral configuration as shown in Fig. 1.5a. When we select an arbitrary position P on the wire (located at a given distance measured along the wire from the input terminal A), we can find a position P' diametrically opposite to P and located at the same distance along the other wire from the

input terminal A'. Then, P and P' lie on the same circle of radius r centered at O and the currents in P and P' are out of phase by $\Delta\phi_0 = 180°$. Thus, the phase difference between neighboring positions P and Q' (on different wires) is given by

$$\Delta\phi = \Delta\phi_0 + d_{\mathrm{P'Q'}} 2\pi/\lambda \tag{1.8}$$

where $\Delta\phi_0 = \pi$ is the input phase difference and $d_{\mathrm{P'Q'}}$ is the arc length P'Q'. If the spacing between wires Δr is much smaller than r, $\Delta r \ll r$, the arc length P'Q' is approximately πr [42]. If P is located at a radial distance of $r = \lambda/2\pi$, the arc length P'Q' is $\lambda/2$. As a result, the phase difference between neighbouring positions P and Q' is $\Delta\phi = 2\pi$. Thus, the currents in P and Q' are in phase and the radiation is maximum because each wire reinforces the radiation of the neighboring wire. Moreover, the condition for precisely in phase currents occurs at two positions where a circle of circumference λ centered in O crosses the wires (positions M and M' in Fig. 1.5b). The turns of the spiral that are at or close to the radial distance $r = \lambda/2\pi$ from O compose the so called active region of the antenna, where the light is radiated or absorbed (marked my a red circle in Fig. 1.5b).

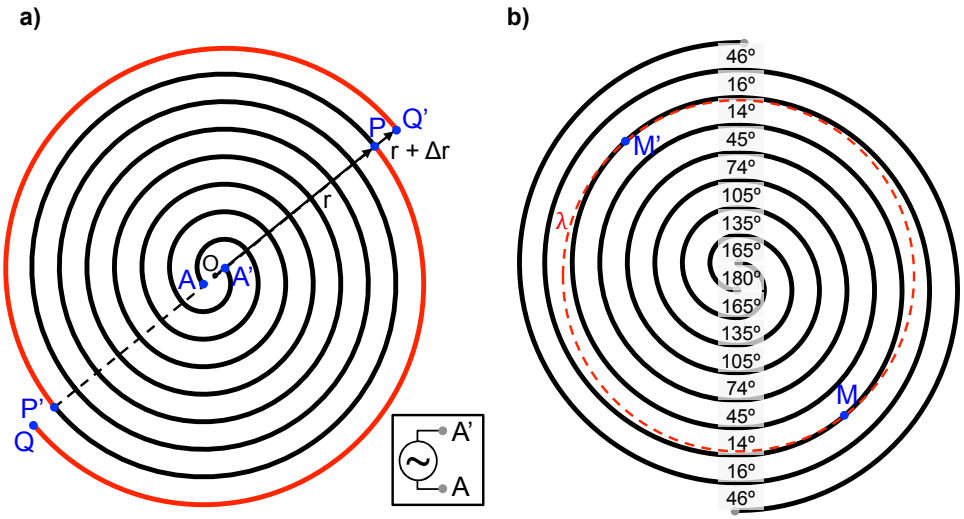

Figure 1.5: **Archimedean spiral antenna formed by a wound two-wire TL. (a)** A source of alternating current is connected to the central terminals of the folded TL (see inset) providing a current which is 180° out of phase for every pair of positions located diametrically opposite (P and P' or Q and Q'). The last half turn (in red) is the path difference between the adjacent positions P and Q' (or P' and Q) located at r and $r + \Delta r$ distance from the spiral center O respectively. **(b)** The same as in **(a)** but rotated, showing the phase difference between adjacent wires for a wavelength of $\lambda = 0.3$ m on a spiral with a pitch of 0.25 m/turn. The red circle of circumference λ outlines the active region of the spiral antenna, where both absorption and radiation are maximum. Adapted from [42].

In Fig. 1.5b we show the phase difference between adjacent wires. It can be observed how neighboring current elements start at anti-phase ($\Delta\phi = \Delta\phi_0 = \pi$) at the feed positions A and A'. As the current propagates outwards along the wires, they gradually come into phase ($\Delta\phi = 2\pi$) and the phase difference continues increasing ($\Delta\phi > 2\pi$).

When the spiral antenna is connected to a source of alternating current (see inset of Fig. 1.5a), it radiates a circularly polarized beam to each side of the spiral [42]. Each radiated beam is normal to the plane of the spiral, and the rotating sense of the circularly polarized light on one side corresponds to the winding sense of the spiral as viewed for the opposite side [42]. Consequently, both radiated beams are identical except for the rotational senses of polarization, which are opposite. Furthermore, a spiral antenna is able to radiate in a broad spectral range as long as the active region for a given wavelength λ is laxly contained within the outer turns of the spiral antenna[2] [42].

The radiation process of Archimedean spiral antennas described above serves to understand the reception process of electromagnetic radiation. When the antenna is illuminated with light that is circularly polarized in the same (opposite) sense of the spiral winding viewed from the illuminating direction, the light is absorbed on the active region and excites a current that propagates inwards (outwards). Subsequently, the current reaches (does not reach) the center terminals from where the signal can be transported to a receiver. This selectivity upon circular polarized light is experimentally verified in Chapter 6 with Archimedean spiral antennas for mid-IR frequencies. Note that linearly polarized light can be described as the interference of left and right circularly polarized beams. As a consequence, when the spiral antenna is illuminated with light polarized linearly along any direction on the spiral plane, the generated current on the antenna reaches the center terminal.

[2]When the active region is of the order or smaller than the outer turns the antenna still radiates. However, the radiation mechanism is similar to a linear dipolar antennas, i.e. based on standing waves. See Chapter 6 for details.

1.2 Characteristics of near-field and far-field regions

In telecommunications technology the space around the antennas is usually divided into three regions, (i) the reactive near-field region, (ii) the radiative near-field region and (iii) the far-field region (see Fig. 1.6). The criteria to define the boundaries between regions is not unique and for some antenna geometries the radiative near-field region may even not exist, e.g. "if the antenna has a maximum dimension that is not large compared to the wavelength" [33]. In the following we will focus on the region in the close proximity of the antenna and the region far away from the antenna, i.e. reactive near-field region and the far field region.

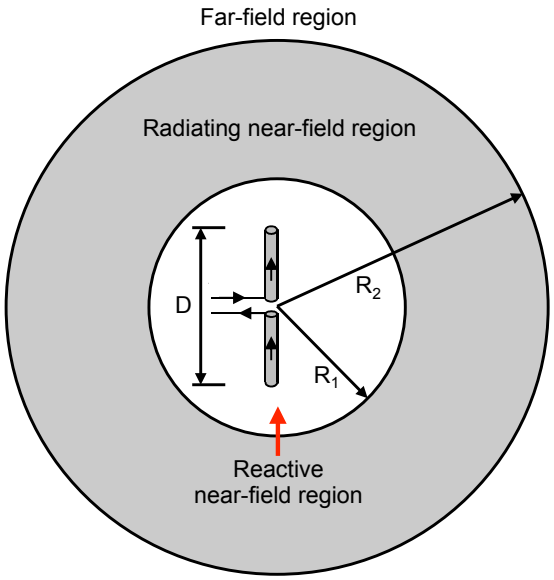

Figure 1.6: **Field regions of an antenna.** According to most commonly used criteria, the three field regions of an antenna are separated as: (i) reactive near-field region for $R < R_1$, (ii) radiative near-field region for $R_2 < R < R_2$ and (iii) far-field region for $R > R_2$, where R is the distance from the antenna surface. $R_1 = 0.62\sqrt{D^3/\lambda}$ and $R_2 = 2D^2/\lambda$, where λ is the wavelength and D is the largest dimension of the antenna. Taken from [33].

In order to explain the difference between electromagnetic near fields and far fields, we analyse the fields around the most simple radiating object, i.e. an oscillating point dipole in vacuum. If the point dipole $\mathbf{p}$ oscillates at frequency ω, it radiates an electromagnetic wave of wavelength λ according to $\lambda = 2\pi c/\omega$, where c is the speed of light in vacuum. The electric field of an oscillating point dipole is given by [43]

$$\mathbf{E} = \frac{1}{4\pi\epsilon_0}\left[k^2\left(\mathbf{n}\times\mathbf{p}\right)\times\mathbf{n}\frac{e^{ikr}}{r} + \left[3\mathbf{n}(\mathbf{n}\cdot\mathbf{p}) - \mathbf{p}\right]\left(\frac{1}{r^3} - \frac{ik}{r^2}\right)e^{ikr}\right]e^{i\omega t} \tag{1.9}$$

where k is the wavevector, $\mathbf{n}$ the unit vector in the direction of the position vector $\mathbf{r}$ ($\mathbf{r} = r\mathbf{n}$).

In the region far from the point dipole, where $kr \gg 1$, the field is given by

$$\mathbf{E} = \frac{1}{4\pi\epsilon_0}k^2\left(\mathbf{n}\times\mathbf{p}\right)\times\mathbf{n}\frac{e^{i(kr-\omega t)}}{r} \tag{1.10}$$

This equation describes a propagating spherical wave which decays slowly with increasing distance from the dipole. It describes the field distribution for the so-called far field of the dipole.

Close to the point dipole, when $kr \ll 1$, the electric field can be approximated by

$$\mathbf{E} = \frac{1}{4\pi\epsilon_0}\frac{\left[3\mathbf{n}(\mathbf{n}\cdot\mathbf{p}) - \mathbf{p}\right]}{r^3}e^{i\omega t} \tag{1.11}$$

This equation describes the so called near field of the dipole. Note that this field oscillates in time but that it does not propagate, i.e. does not transport energy from the dipole. The field distribution at a given time t is that of a static electric dipole [43].

In general, the near fields are characterized by having at least one imaginary component on the wavevector $\mathbf{k}$ describing the direction of propagation. Meaning that the wave does not propagate in the direction described by the imaginary component of $\mathbf{k}$, but rather decays exponentially [36].

In Fig. 1.7 we show the field distributions for both near field (Fig. 1.7a) and far field (Fig. 1.7b) of a point dipole $\mathbf{p}$. We observe that the near fields are strongest at the pole regions of the dipole and that they are strongly confined to the close proximity of the dipole position (beyond the diffraction limit $\sim \lambda/2$). The far fields, in contrast, are strongest perpendicular to the direction of the dipole and propagate away from it. Note that the fields on the near field (far field) region are masked by a disc of radius $r = \lambda/10$ ($r = \lambda$) centered at the position where the point dipole $\mathbf{p}$ (marked by the green arrow) is located.

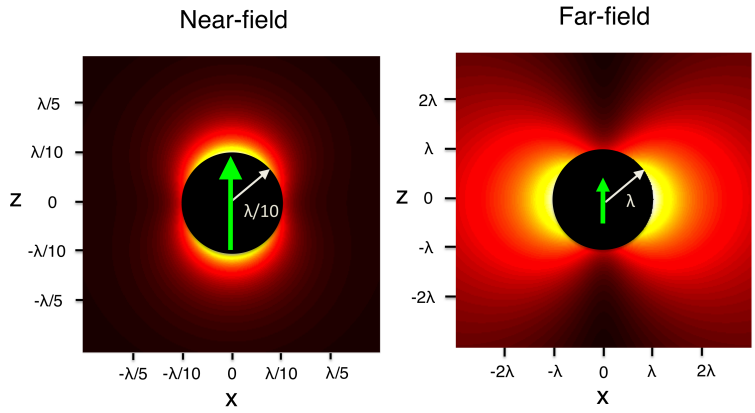

Figure 1.7: **Electric field amplitude of an oscillating electric point dipole.** **(a)** Near field distribution and **(b)** Far field distribution of an oscillating point dipole. The green arrow indicates the dipole orientation and location. The black disc of radius $r = \lambda/10$ in **(a)** and $r = \lambda$ in **(b)** masks the fields around the dipole for clarity. Taken from [44]

Far fields are free-space propagating waves which after being emitted can propagate for ever, although the radiation source stops radiating. In contrast, the near fields do not propagate but store the energy that drives the dipole oscillation, and thus when the dipole stops oscillating (or in general source is turned off), the near field vanish [35]. In the same way, the dipole oscillation (the source) is affected by any change in the near fields such as a external object entering the near field region. For that reason, the near field are also called reactive fields or storage fields. This also implies that measuring near fields is inherently difficult because the near-field probe can interact with the source of near fields, disturbing the measurement [35].

During this thesis, we investigate TLs which are by design non-radiating structures, i.e. the TLs do not have a far field distribution. As a result, only near fields close to the wires surface reveal the presence propagating electromagnetic mode along the TL. These near fields, as the ones for the point dipole shown in Fig. 1.7, are localized in the close proximity of the wires. Thus, in order to visualize the mode along the TL we need to map the near field distribution of the TL. To do so, we take advantage of the fact that near fields can be converted into propagating waves when they interact with matter [45]. This phenomenon explains how information about subwavelength features can be transferred into the far-field [36]. In Chapter 2 we describe the technique we use for near-field imaging.

1.3 Optical response of metal structures

In RF regime metals behave as nearly perfect electric conductors, which implies that negligible amount of field penetrates into the conductor. As a result one can assume lossless conductors can be assumed when theoretically describing antennas and TLs at RF range. In IR and visible frequency ranges however, the field penetration into the metal is significant and the subsequent increase of damping is strong. Thus, a different theoretical approach, where these effects are taken into account, is needed in order to describe metals' response at IR and visible frequencies.

At RF, electromagnetic radiation can generate currents in metallic wires. Similarly, at visible and and IR frequencies, collective oscillations of conduction electrons can be excited on metallic surfaces. However, the electromagnetic radiation couples more strongly to these collective oscillations on the metal surfaces. The generated surface waves are called surface plasmon polaritons (SPPs) [46] and provide strong confinement and channeling of light on the subwavelength scale, i.e. beyond the diffraction limit [47]. On finite structures such as metallic nanoparticles, SPPs are confined within the particles's boundaries and can built up resonances called localized surface plasmon (LSP) resonances. These metal nanoparticles, also called nanoantennas, are capable of capturing electromagnetic waves and convert them into strongly enhanced and subwavelength-scale confined optical fields (and vice versa). Note that RF antennas also convert the incident electromagnetic radiation into subwavelength-scale localized fields and that the electromagnetic wave associated to the current along RF TLs is also confined in the subwavelength scale. For example a Radio signal at wavelength 500 m can be transported in a coax cable with a diameter of few millimetres.

The response of metals to an incident electromagnetic radiation is largely governed by the free electrons in the metal [35]. The electric field $\mathbf{E}$ displaces the electrons in the conduction band. The cumulative effect of all individual displacements of the conduction electrons results in a macroscopic polarization $\mathbf{P}$ of the metal [36]. The electric field $\mathbf{E}$ and the polarization $\mathbf{P}$ are related through a complex dielectric function ϵ according to $\epsilon = 1 + |\mathbf{P}|/\left(\epsilon_0|\mathbf{E}|\right)$ [36]. The dielectric function ϵ depends on the frequency of light ω ($\epsilon(\omega)$) and serves to describe the optical properties of metals. The optical properties are mainly determined (i) by the fact that the conduction electrons can move freely in the bulk material and (ii) that interband transitions can occur when the energy of the incident photons exceeds the band gap energy of the respective metal [36].

A simple model to describe the dielectric function of metals is the Drude-Sommerfeld model for the free- electron gas, which assumes that the conduction electrons are allowed to move freely within the bulk of the metal. Experimental measurements of the dielectric function of metals [48–51] show that although simple, this model gives accurate results in certain frequency ranges, e.g. in the IR regime (see Fig. 1.8b). Applying this model we obtain a complex dielectric function $\epsilon_{\text{Drude}}(\omega)$ which depends on the on the frequency ω of the incident electric field $\mathbf{E}$:

$$\epsilon_{\text{Drude}}(\omega) = \epsilon_{\text{inf}} - \frac{\omega_p^2}{\omega^2 + i\Gamma\omega} \tag{1.12}$$

where ω_p is the plasma frequency and Γ a damping term because of electron-electron and electron-phonon scattering [36]. The term ϵ_{inf} is a constant offset which accounts for interband transitions that are not considered in the model [36]. In Figs. 1.8a and 1.8b the dielectric function of the noble metal gold is shown according to the Drude-Sommerfeld model (line) [35] which is compared to the experimental values taken from Johnson & Christy [48] and Palik [49] (circles), respectively. Good agreement is found confirming the validity of the Drude-Sommerfeld model for wavelengths $\lambda \geqslant 600$ nm.

To plot the dielectric function of gold $\epsilon_{\text{Au}}(\omega) = \epsilon' + i\epsilon''$ at visible frequencies (Fig. 1.8a), the following constants for gold taken from [6] are used in Eq. 1.12:

$$\epsilon_{\text{inf}} = 11,\ \omega_p = 8.95\,\text{eV and } \Gamma = 65.8\,\text{meV} \tag{1.13}$$

In Fig. 1.8a, the real part ϵ' of the dielectric function is always negative leading to an imaginary part of the refractive index n ($n = \sqrt{\epsilon}$). This is a consequence of the fast response of the free electrons to the electric field $\mathbf{E}$, which allows the electron to screen the incident fields and limit the penetration of light to a very small extent [36,52]. Hence, most noble metals appear opaque and highly reflective at visible frequencies [35]. At shorter wavelengths $\lambda < 600$ nm interband transitions take place, leading to absorption losses in the metal. This can be seen with the strong increase in the metal in the experimental values [48] (circles) of the imaginary part ϵ'' accounts for the dissipation of energy associated to the movement of electrons. Note that the Drude-Sommerfeld model does not reproduce the strong increase in ϵ'' because it does not directly take into account the interband transitions.

In Fig. 1.8b, the dielectric function of gold $\epsilon_{\text{Au}}(\omega) = \epsilon' + i\epsilon''$ at mid-IR frequencies

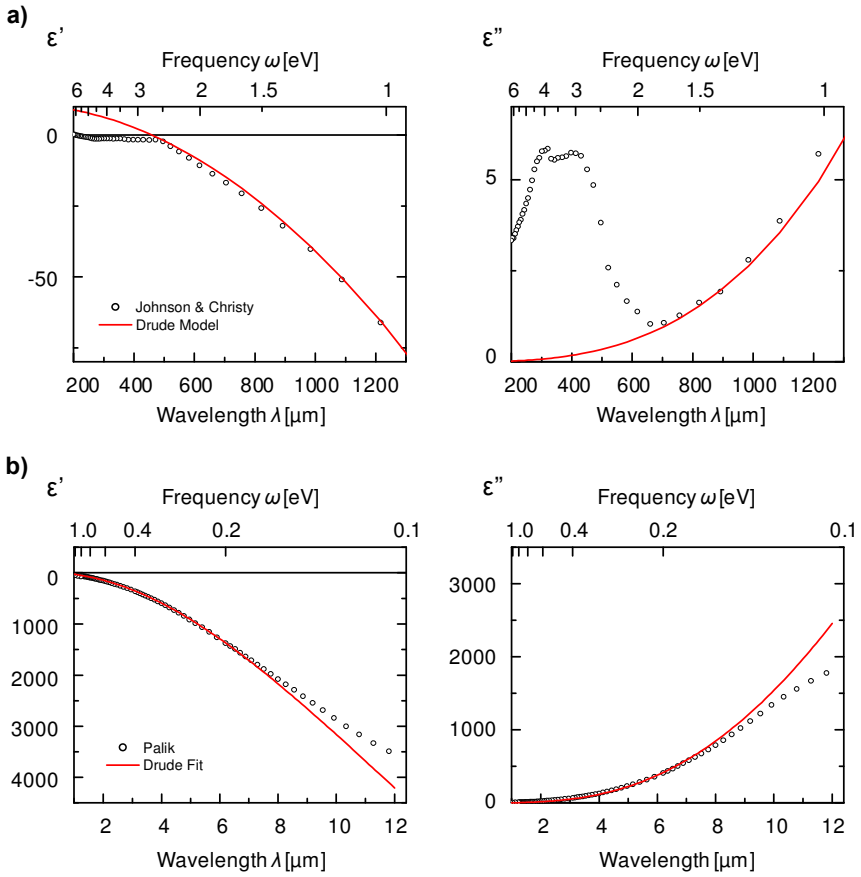

Figure 1.8: Plot of the dielectric constant $\epsilon = \epsilon' + i\epsilon''$ of the noble metal Gold as a function of wavelength (lower x-axis) and frequency (upper x-axis). **(a)** Drude model (line) and experimental values (circles) from Johnson & Christy [48] for the visible and near-infrared spectral range. **(b)** Experimental values from Palik [49] (circles) and Drude model fitted to the experimental values (line), plotted for the mid-infrared spectral range. Note that the frequencies ω_p and Γ are expressed in units of energy (eV). Taken from [35].

is shown. The Drude-Sommerfeld model is compared to experimental values from Palik [49] in the wavelength range from 1 μm to 12 μm. In order to describe the data from Palik [49], the Drude-Sommerfeld model was fitted to the experimental data for the wavelength range from 1.5 μm to 7.1 μm, yielding the new values [35]:

$$\epsilon_{\text{inf}} = 11,\ \omega_p = 7.77\,\text{eV and } \Gamma = 60.2\,\text{meV (for mid-IR)} \tag{1.14}$$

where ϵ_{inf} was held constant during the fitting. As it can be seen form the the Fig. 1.8b, the optical properties of gold in the mid-infrared range are well described by the Drude-Sommerfeld model at wavelengths from 1 μm to about 7 μm. Only for wavelengths

longer $\lambda = 7.1$ μm, the model slightly differs form experimental [35]. This is related to a decreasing slope at these wavelengths, not observed with other experimental data (e.g. Ordal et al. [50]).

Chapter 2

Transmission-mode s-SNOM

Near-field imaging of plasmonic structures provides complementary information to far-field studies. For example, it enables the direct visualization of localized plasmonic modes. Scattering-type Scanning Near-field Optical Microscopy (s-SNOM) is a technique that allows for high resolution near-field imaging. A sharp tip scans the sample surface and scatters the near-fields close to it. Recording the near-field signal as a function of position yields near-field images with nanoscale resolution from THz to visible frequencies. The aim of this work is the near-field characterization of extended plasmonic structures, such as spiral antennas and transmission lines (TLs) which requires homogeneous sample illumination (i.e. avoiding retardation effects) with linearly and as well as circularly polarized light. To that end we improved a homebuilt transmission-mode s-SNOM at nanoGUNE. We tested the microscope with heptamer antenna structures and L shaped antennas. Comparing the experimental near-field images with numerically calculated modal field distributions, a good agreement is found. These first near-field maps of extended structures pave the way for characterization of complex plasmonic structures under various excitation configurations, as will be demonstrated in Chapters 3, 5 and 6.

2.1 Introduction

Optical microscopy allows for imaging samples by collecting the light reflected from or transmitted through them. In conventional optical microscopy, the imaging is based on propagating electromagnetic waves, which restricts the spatial resolution due to

diffraction [53]. In order to distinguish two point-like objects from each other, the separation needs to be larger than

$$d \simeq \frac{\lambda}{2} \tag{2.1}$$

where λ is the wavelength of the light [53]. The diffraction limit also prevents imaging of subwavelength-scale near-field distributions at the surface of plasmonic nanostructures, antennas, TLs and metasurfaces.

There are several techniques that can overcome the problem of the diffraction limit, to map the nanoscale near-field distributions of the plasmonic structures: Cathodoluminescence (CL) [54–56], Electron Energy Loss Spectroscopy (EELS) [57–61], Two-Photon-induced Luminescence microscopy (TPL) [5, 62–67], Photoemission Electron Microscopy (PEEM) [68–72] and Scanning Near-field Optical Microscopy (SNOM) [73–79]. In this thesis scattering-type Scanning Near-field Optical Microscopy (s-SNOM [77–81] also called apertureless SNOM) was employed. The s-SNOM belongs to the family of Scanning Probe Microscopies (SPM).It utilizes a sharp tip to scan the sample surface, yielding topography simultaneously to information on the spatial near-field distribution. We have used the s-SNOM to investigate the near-field distribution of antennas and TLs operating at infrared frequencies. In the following we explain the working principles of s-SNOM.

2.2 s-SNOM for antenna mapping

2.2.1 Near-field probing and interferometric detection

The s-SNOM is based on an Atomic Force Microscope (AFM) [79,82,83], which lets us control the tip-sample distance with sub-nanometer precision. The sample and the tip are illuminated by a focused laser beam, which generates near fields on the sample surface. In Fig. 2.1 we show, as an example, a gap antenna illuminated with light polarized along the antenna's long axis. As a consequence the first dipolar mode has been exited, generating strong near-fields in the close proximity of the antenna surface because of the oscillating charge distribution. The AFM tip is brought into close proximity to the sample, into the so called near-field region. The tip is able to locally convert the near-fields at the sample surface into propagating fields which are collected and directed to

the detector to be recorded [84,85]. In Fig. 2.1 a silicon tip is used to scatter the near fields on the antenna surface. It is a common choice to use commercial AFM silicon tips as near-field probes [77,86,87]. Owing to their weak polarizability, the silicon tips act as weak scatterers and disturb the near field to be mapped only negligibly [84,87,88]. Because the illuminating laser beam is diffraction limited, the illuminated area includes the area that is probed by the tip and its surroundings. Analogously, the collected scattered field E_{tip} is a sum of the near-field scattered light by the tip apex E_{nf} and an unwanted background scattered by the tip shaft, the cantilever carrying the tip, and the sample surface E_{bkg} [89]:

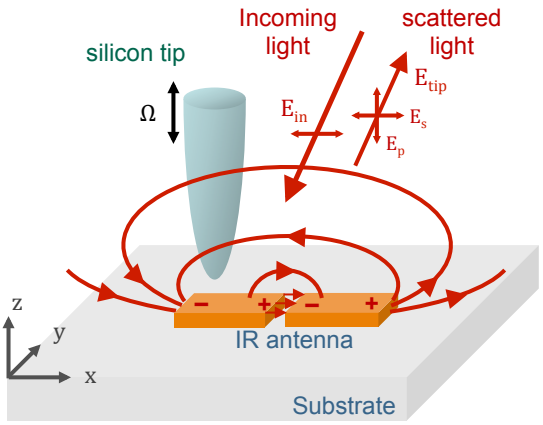

Figure 2.1: **Mapping the near-field distribution of a gap antenna with side-illumination s-SNOM.** Incoming field E_{in} polarized along the long antenna axis excites the first longitudinal dipolar mode of the gap antenna. A silicon AFM tip oscillating at frequency Ω scatters the near-fields (red field lines) of the antenna when is brought close to the antenna surface. The scattered field E_{tip} contains E_s and E_p components.

$$E_{tip} = E_{nf} + E_{bkg} \tag{2.2}$$

where both E_{nf} and E_{bkg} depend on the tip sample distance: E_{nf} decays exponentially with increasing distance from the sample [93], while E_{bkg} exhibits a distance dependence given by the wavelength of the light, caused by interference of incident and sample reflected waves [89]. If the tip oscillation amplitude (tapping amplitude) A is much smaller than the wavelength λ_0 ($A \ll \lambda_0$), E_{bkg} remains nearly constant. Hence, the different dependence upon tip-sample distance of the of E_{nf} and E_{bkg} can be used to extract the scattered near-fields E_{nf} from the collected scattered field E_{tip}. To that end the AFM is operated in tapping mode with a tapping frequency Ω. As a consequence, the scattered signal $E_{tip} = E_{nf} + E_{bkg}$ is also modulated, and the contribution of

E_{nf} and E_{bkg} carry higher harmonic terms appearing at $n\Omega$ with $n = 1, 2, ...$ Thus, demodulation of the detector signal at higher harmonics $n\Omega$ ($n > 1$) allows extracting the near-field signal [90–93] as it is explained in 2.2.2.

Additionally, the the scattered light is detected interferometrically in order to resolve the amplitude and phase of the near-field E_{nf}. To that end a Michelson interferometer is built around the AFM.

In Fig. 2.2 we show the setup of a s-SNOM. As it can be observed, the incoming light is separated by the beam splitter BS into a reference beam and a probing beam. The sample is located in the probing arm of the Michelson interferometer where the sample and tip are illuminated by the parabolic mirror from above with an angle of incidence of around 30° relative to the surface (side-illumination scheme). The incident field E_{in} is s-polarized, along the long antenna axis to provide efficient excitation of the antenna. The backscattered light (green beam in the probing arm) is collected by the parabolic mirror and reflected into the detector. In the reference arm, a piezo-actuated mirror (PMZ) oscillating at frequency M modulates the phase of the reference beam. Furthermore, there might be some infrared attenuators (not shown in Fig. 2.2) in the reference arm in order to avoid possible saturation of the detector. The phase-modulated reference beam is recombined with the backscattered light in the beam splitter and the interference of both beams is recorded by the detector. This interferometric detection in combination with higher harmonic demodulation at $n\Omega$ of the detector signal yields the amplitude $|E_n|$ and phase φ_n of the scattered near-field E_{nf}.

Polarizers P1 and P2 are inserted to select the s- or p-polarized component contained in the scattered light (indicated by E_s and E_p in Fig. 2.1). Polarizer P1 is kept fixed at 45° to provide an equal interference with both p- and s-polarized components. Polarizer P2 can be rotated freely to select either the p-polarized component E_p (when aligned vertically) or s-polarized component E_s (when aligned horizontally) of the scattered field.

In order to get an image of the near-field distribution of the antenna the tip is kept fixed on the focal point of the parabolic mirror and the sample is scanned using a sample scanner based on piezoelectric crystals. Both, AFM and near-field signals are recorded as a function of the scan position, yielding topography and near-field images simultaneously. It is important to note that both the mechanical and optical resolutions are determined by the radius of curvature of the tip apex, typically around

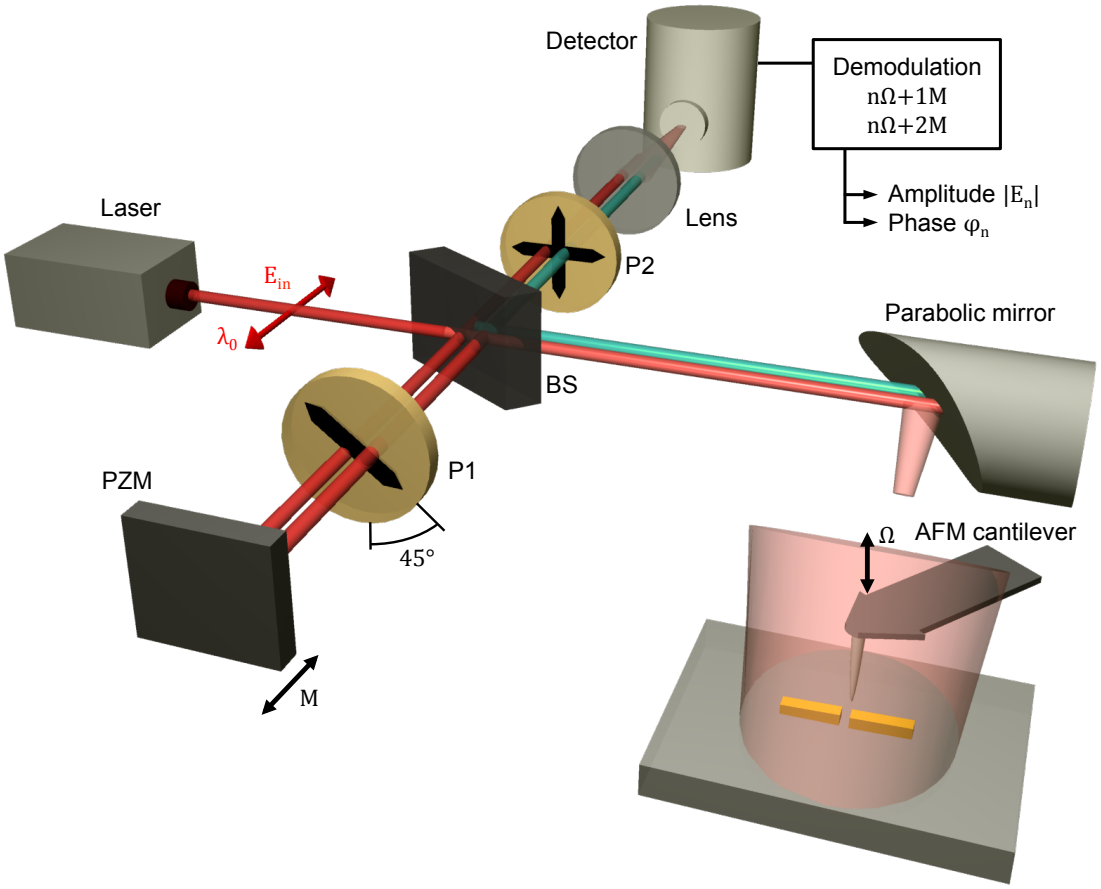

Figure 2.2: **Schematics of the Side-illumination s-SNOM.** The components are: beam splitter BS; Polarizers P1 and P2; Piezo-actuated mirror PZM, driven at frequency M; Parabolic mirror; AFM operated in tapping mode with a tapping frequency Ω. A Michelson interferometer with the sample located in one of the arms is used for interferometric detection.

10-20 nm [79]. Thus, we have a wavelength-independent optical resolution, which allows nanoscale imaging at visible [90], infrared [94] and terahertz [95] frequencies, well beyond diffraction limit.

2.2.2 Signal acquisition

In this section we describe the demodulation process at higher harmonic to obtain the near-field signal form the interferometrically detected scattered signal base mainly on the references [91] and [35].

The detected signal is a coherent superposition of the scattered near-fields E_{nf}, the background scattering E_{bkg} and the reference field E_{ref} (the electric field of the

reference beam). Because the detector is sensitive to the field intensity I_d, these three contributions get mixed in the detector signal S.

$$S \propto I_d = E_d E_d^* = \left(E_{ref} + E_{nf} + E_{bkg}\right)\left(E_{ref} + E_{nf} + E_{bkg}\right)^* \tag{2.3}$$

where E_d^* is the complex conjugate of E_d. Because the PZM vibrates at frequency M the electric field of the reference beam can be expressed as

$$E_{ref} = E_{in} e^{i\gamma \cos(Mt)} \tag{2.4}$$

where γ is the amplitude and the M is the frequency of the phase modulation. The scattered near-field E_{nf} and the background scattering E_{bkg} can be written as

$$E_{nf} = \sigma_{nf} E_{in} \tag{2.5}$$

$$E_{bkg} = \sigma_{bkg} E_{in} \tag{2.6}$$

where σ_{nf} and σ_{bkg} are the scattering coefficients for the near-fields and the background respectively. Due to the non linear distance dependence of E_{nf} and E_{bkg} and because the tip oscillates at frequency Ω, the contribution of E_{nf} and E_{bkg} carry higher harmonic terms appearing at $n\Omega$ with $n = 1, 2, ...$ As E_{nf} and E_{bkg} are mixed with E_{ref} which is modulated as shown in Eq. 2.3, side bands appear at $n\Omega + mM$ where M is the frequency of the phase modulation and $m = 1, 2, ...$ (see Fig. 2.3). Typically the tip is driven with an oscillation frequency Ω of around 300 kHz close to tip's resonance frequency and M is in the range of 100 Hz - 700 Hz.

The scattered near-field E_{nf} and the background scattering E_{bkg} can be written as a Fourier series [92]:

$$E_{nf} = \sum_{n=0}^{\infty} \sigma_{nf,n} \cos\left(n\Omega t\right) E_{in} \tag{2.7}$$

$$E_{bkg} = \sum_{n=0}^{\infty} \sigma_{bkg,n} \cos\left(n\Omega t\right) E_{in} \tag{2.8}$$

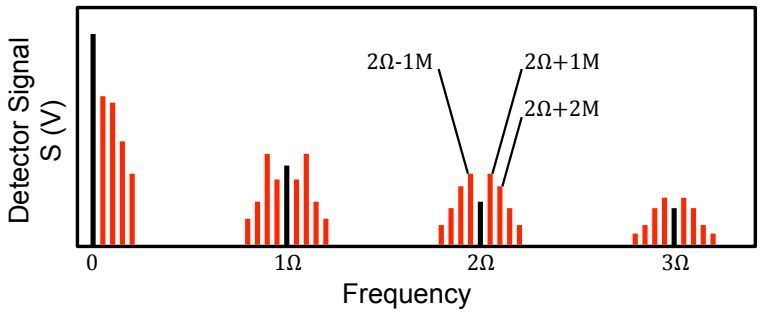

Figure 2.3: **Schematics representation of the frequency spectrum of the detector signal when employing pseudoheterodyne interferometric detection.** Ω is the tip oscillation frequency and M is the frequency of the phase modulation. Adapted from [91].

where $\sigma_{nf,n}$ and $\sigma_{bkg,n}$ are the complex-valued Fourier expansion coefficients of σ_{nf} and σ_{bkg} and Ω is the tip oscillation frequency. In the same way, according to $E_{tip} = E_{nf} + E_{bkg}$ (Eq. 2.2) we can obtain the n-th Fourier coefficient of the tip-scattered light as $\sigma_{tip,n} = \sigma_{nf,n} + \sigma_{bkg,n}$.

The tip-scattered field E_{tip} is dominated by the background scattering E_{bkg} [91]. However, the ratio $\sigma_{nf,n}/\sigma_{bkg,n}$ and thus, the contribution of the scattered near-field to the signal in the n-th term of the expansion increases with increasing number n. This can be understood looking at the dependence of scattered near-field E_{nf} and the background scattering E_{bkg} with tip-sample distance stated previously. Since higher harmonics have higher frequencies, they measure faster changes in the scattering signal. As a consequence, at higher harmonics $n\Omega$ ($n > 1$) the near-field signal is stronger than the background signal. This means that by choosing an sufficiently large n, a pure near-field scattering contrast can be recorded [91]. Demodulation of the detector signal at higher harmonics $n\Omega$ ($n > 1$) allows extracting the near-field signal [90–93] as is explained next. We note that even though higher harmonics have higher near-field contrast, they have lower amplitude, which means that we need to find a compromise between signal intensity and complete background suppression. In practical terms, $n = 3$ is usually enough to obtain a sufficiently intense background-free signal.

Among the different contributions to the detector signal S (see Eq. 2.3), the terms containing only E_{nf} and/or E_{bkg} generate harmonics at $n\Omega$ (black lines in Fig. 2.3) and the terms containing the products $E_{nf}E^*_{ref}$, $E_{bkg}E^*_{ref}$ or their complex conjugates generate the side bands at $n\Omega + mM$ (red lines in Fig. 2.3). This side bands are used to extract the amplitude s_n and phase φ_n of the Fourier coefficient σ_{nf} from the

demodulated detector signal S_n:

$$\sigma_{nf,n} = s_n e^{i\varphi_n} \tag{2.9}$$

$$\sigma_{bkg,n} = s_{bkg,n} e^{i\varphi_{bkg,n}} \tag{2.10}$$

$$\sigma_{tip,n} = \sigma_{nf,n} + \sigma_{bkg,n} = A_n e^{i\phi_n} \tag{2.11}$$

It can be shown that by analyzing the side bands at frequencies $f_{n,1} = n\Omega + M$ and $f_{n,2} = n\Omega + 2M$, $S_{n,1} = S\left(f_{n,1}\right)$ and $S_{n,2} = S\left(f_{n,2}\right)$ respectively (see the side bands marked with arrows in Fig. 2.3), we can obtain the n-th Fourier coefficient of the tip-scattered light $\sigma_{tip,n}$ [91, 92].

$$\sigma_{tip,n} = \sigma_{nf,n} + \sigma_{bkg,n} = 2.16k\left(S_{n,1} + iS_{n,2}\right) \tag{2.12}$$

where we have assumed that the modulation amplitude $\gamma = 2.63$ and k is a complex-valued constant that depends on the adjustment of the interferometer. The contribution of the background scattering $\sigma_{bkg,n}$ becomes negligibly small[1] for a sufficiently high n. Then, we can assume that $\sigma_{tip,n} \approx \sigma_{nf,n}$ and thus,

$$s_n = 2.16k\sqrt{S_{n,1}^2 + S_{n,2}^2} \tag{2.13}$$

$$\varphi_n = \arctan\left(2.16k\frac{S_{n,1}}{S_{n,2}}\right) \tag{2.14}$$

where s_n and φ_n are the signals obtained in s-SNOM with pseudoheterodyne interferometric detection.

All the s-SNOM images shown in this chapter and in the Chapters 3, 5 and 6 display the measured amplitude s_3 and phase φ_3. For better readability, we substitute s_3 and phase φ_3 by $|E_p|$ and φ_p ($|E_s|$ and φ_s) when p-component (s-component) of the tip-scattered field is measured.

[1] When the contribution of the background scattering $\sigma_{bkg,n}$ is not negligible, the obtained results are the amplitude A_n and phase ϕ_n of the tip-scattered light which contain some background information.

2.2.3 Illumination in normal incidence for complex structures

In a typical s-SNOM setup, the sample is illuminated from above under a certain angle of incidence and the backscattered light is collected [77, 78, 80, 86, 96]. However, when mapping extended plasmonic structures it is more convenient to illuminate the sample from below in normal incidence through a transparent substrate that supports the plasmonic structures. The scattered near-field can be collected from above as in a side-illumination s-SNOM setup. This version of s-SNOM was recently introduced, and it is called transmission-mode s-SNOM [97].

Mapping extended plasmonic structures with a side-illumination scheme has one main practical disadvantage, i.e. illuminating the sample from the side causes retardation effects [86]. When the size of the structures to be analyzed are of the order of the wavelength of the incident light, artificial phase gradients are generated as it is represented Fig. 2.4a for an antenna array. By using transmission-mode s-SNOM, we avoid such retardation effects when exciting the structure [98]. While the tip is only polarized weakly because the polarization of the incident beam is always perpendicular to the tip's long axis (see Fig. 2.4b). In the following the transmission mode s-SNOM used during this thesis will be described.

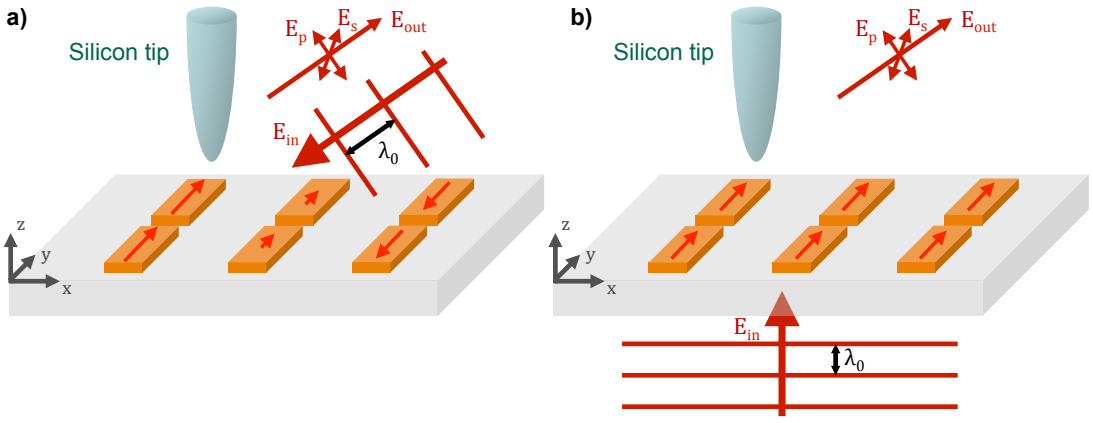

Figure 2.4: **Principle of s-SNOM for different illumination schemes.** **(a)** in side-illumination scheme the structure is illuminated from one side, which makes that a different wavefront reaches each of the gap antennas on the array. **(b)** in transmission-mode the the structure is illuminated from below exciting all the gap antennas on the array with the same wavefront, i.e. with the same phase.

2.3 Transmission-mode s-SNOM

The transmission-mode s-SNOM used during this thesis is based on a modified commercial AFM from the company JPK Instruments AG (www.jpk.com) [35,97]. We use commercial AFM silicon tips from the company NanoWorld AG (www.nanoworld.com) typically of type Arrow-NRC-50. The AFM is operated in tapping mode where the cantilever oscillates with a frequency near its mechanical resonance, around $\Omega = 300$ kHz and a tapping amplitude A (30-100 nm). The schematics of the transmission-mode s-SNOM set up is shown in Fig. 2.5. The sample is illuminated from below using a lens (not shown in Fig. 2.5) with a low numerical aperture of $NA \approx 0.1$ to obtain a weakly focused beam (spot size of ~ 50 μm in diameter on the sample surface) [35]. This provides a homogeneous illumination even for large plasmonic structures. The scattered near-fields are collected at an angle of about 30° relative to the sample surface by a parabolic mirror, whose focal point is at the tip apex (see Fig. 2.5).

As it can be seen in Fig. 2.5, we built a Mach-Zehnder interferometer around the AFM [53]. We use several beam splitters to split the beam (in BS1) into the probing beam and the reference beam, and later to combine (in BS3) them before reaching the detector. The probing beam illuminates the sample from below, usually at a wavelength of $\lambda_0 = 9.3$ μm. The incident field E_{in} is polarized along the antenna attached to the TL to efficiently excite the antenna and launch a mode along the TL, while the tip is weakly polarized. The near fields generated at the tip are thus weak and do not disturb the near fields on the antenna and along the TL [80,86,96]. As in side-illuminaton scheme, the reference beam is modulated with a PZM which oscillates at frequency M and the polarization of the field E_{ref} is rotated by 45° relative to the vertical direction with the polarizer P1 (see Fig. 2.5). Furthermore, there might be some infrared attenuators (not shown in Fig. 2.5) in the reference arm in order to avoid possible saturation of the detector. We select to record the p-polarized (s-polarized) scattered field by aligning the polarizer P2 vertically (horizontally), once the reference beam and the probing beam are recombined in BS3 (see Fig. 2.5). Finally, by demodulating the detector signal at frequencies $M + n\Omega$ and $2M + n\Omega$, $n > 1$, both amplitude and phase of the p- or s-component of the tip-scattered field, ($|\mathrm{E}_p|$, φ_p) or ($|\mathrm{E}_s|$, φ_s), are obtained simultaneously [32,97–99].

The transmission-mode s-SNOM used in this thesis to map extended plasmonic structures was a previously developed set up [35]. In order to illuminate with linearly

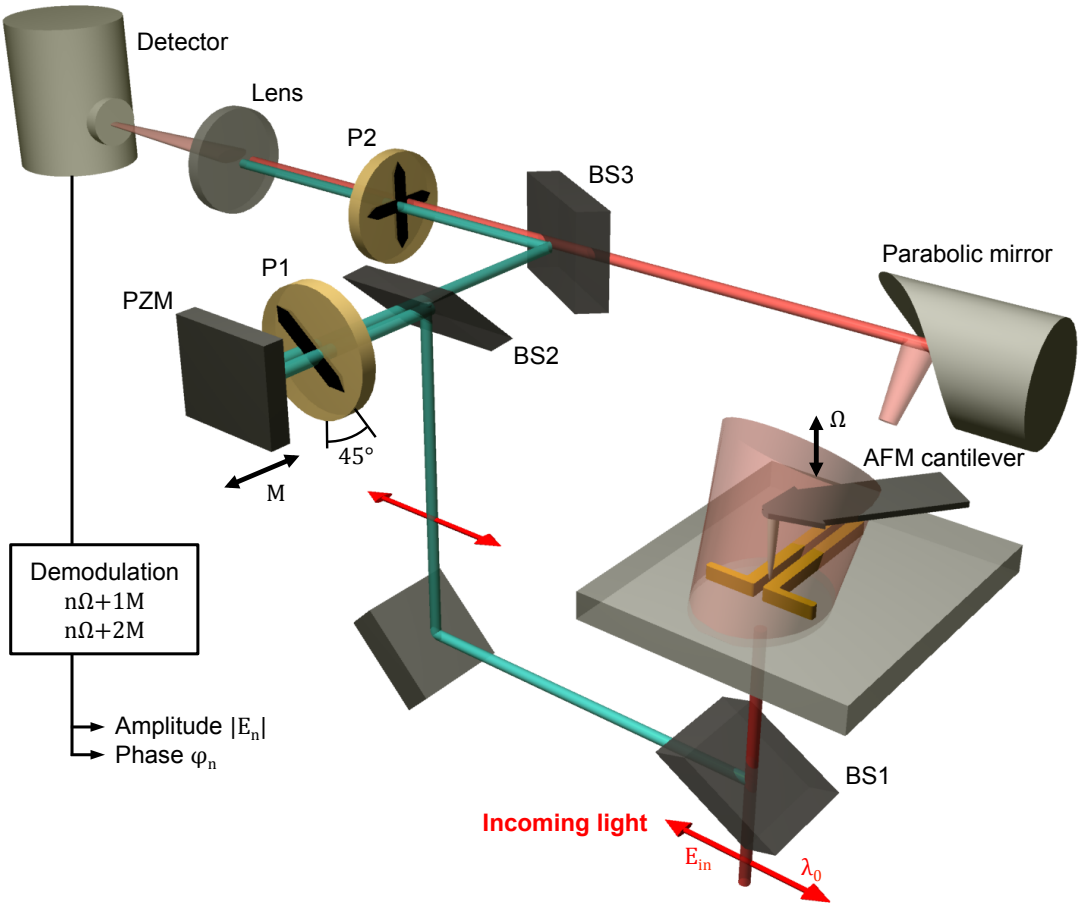

Figure 2.5: **Setup of the transmission-mode s-SNOM with pseudoheterodyne detection.** The components are: beam splitters BS1, BS2, BS3; Polarizers 1 and 2; Piezo-actuated mirror PZM, driven at frequency M; Polarizers P1 and P2; AFM operated in tapping mode with a tapping frequency Ω.

and circularly polarized light we implemented an extra optical path for the probing beam. In this extra optical path for the probing beam we located a periscope (see inset of Fig. 2.6b) which rotates the polarization of incident light by 90°. By setting an extra polarizer (polarizer P3 in Fig. 2.9) in the extra optical path and rotating it from $-45°$ to 45° we can obtain linearly polarized light along any direction on the sample plane (xy plane in Fig. 2.6). In addition, we also included a phase retarding mirror (PRM) into the extra path of the probing beam after the polarizer P3 to generate left- (LCP) and right-handed circular polarized (RCP) light (see Chapter 6). LCP and RCP are obtained when linearly polarized light with equal s- and p-components, i.e. polarized along a direction at $-45°$ and 45° relative to the vertical direction, is reflected in the PRM. The PRM introduced phase shift of 90° between the s- and p-

components obtaining circularly polarized light. Please note that the two optical paths are set so that they coincide when illuminating the sample in normal incidence and can be interchanged with two flip mirrors. This allows to map a plasmonic structure with different light polarization states[2] without any realignment of the setup (no adjustment of the parabolic mirror, reference beam, etc).

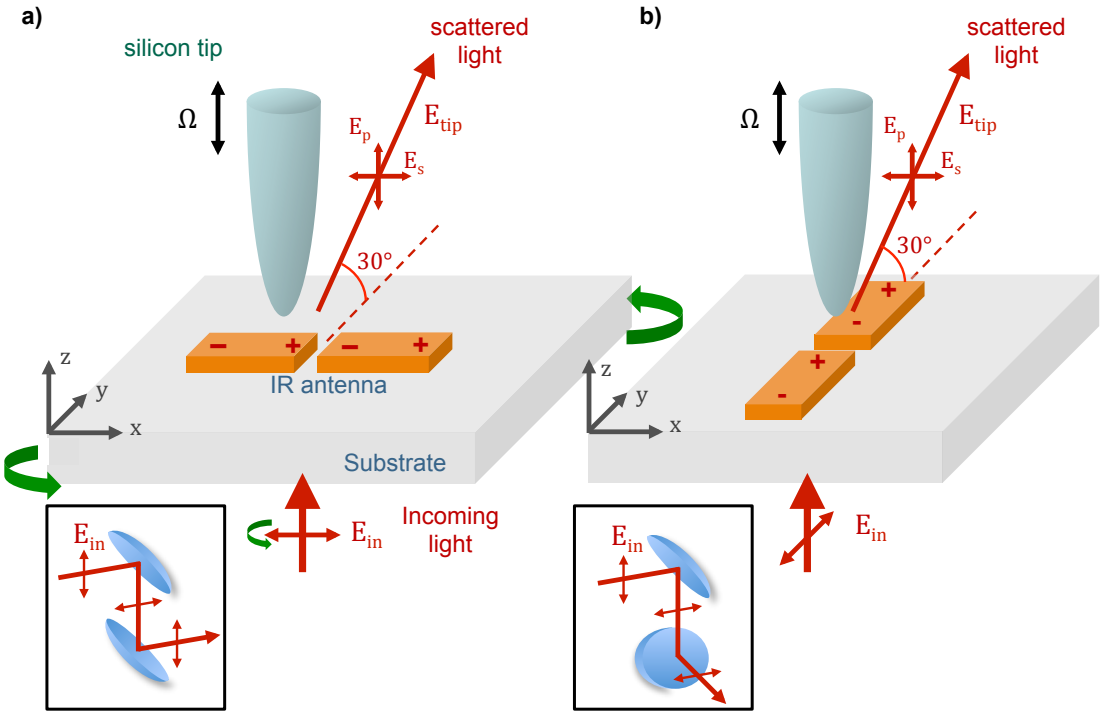

Figure 2.6: **Rotation of polarization of light on the sample plane.** **(a)** The gap antenna is illuminated from below in normal incidence with light polarized along the long antenna axis (x direction). The tip-scattered light is collected in a perpendicular direction with the antenna's long axis.**(b)** Both the sample and the polarization of light are rotated by 90° so that the antenna is illuminated with light polarized along its long axis (y direction). The tip-scattered light is collected in a direction that forms 30° with the antenna's long axis. The insets show the periscopes that provide perpendicular polarization of light.

The direction in which the tip-scattered light is collected is given by the parabolic mirror and is fixed. However, we can rotate the sample and the polarization of the incident light so that the plasmonic structure is still efficiently excited when the sample is rotated. This enables to collect the tip-scattered light along any direction relative to the plasmonic structure as it is illustrated in Fig. 2.6 (see also Fig. 2.9). In Fig. 2.6, both the polarization of the incident light and the sample are rotated by 90° to

[2]Circularly polarized light (LCP or RCP) or linearly polarized light along any direction on the sample plane.

maintain an efficient excitation of the longitudinal antenna mode. However, in Fig. 2.6a the tip-scattered light is collected in perpendicular direction with the antenna's long axis while in Fig. 2.6b it is collected in a direction that forms 30° with the antenna's long axis. Note that it is also possible to rotate the sample and the polarization of light independently when mapping structures that are excited with light polarized along different directions.

2.4 Implementation of transmission-mode s-SNOM

During this thesis, we have used our transmission-mode s-SNOM to study different extended structures. In the following, we present two examples of near-field characterization of extended structures.

2.4.1 Real-Space Mapping of Fano Interference in Heptamer Structure

The first example is a "plasmonic metamolecule" consisting of seven gold discs of the same size arranged in a heptamer configuration on top a CaF_2 substrate (see Fig. 2.7). This heptamer structure is a widely studied configuration exhibiting a so called Fano resonance [100–107], which was previously studied by means of far-field experiments and calculations [106, 108]. However, the spatial field distribution of Fano modes behind these spectral features was experimentally unexplored. From numerically calculated charge density distributions of the heptamer structure, large differences were observed between charge distribution at different spectral positions around the Fano resonance [106]. Accordingly, we expected large changes near field distribution on the heptamer structure across the Fano resonance.

In order to map the near-filed distribution of such a extended structure, a plane wave illumination in normal incidence is crucial to avoid retardation effects (see Fig. 2.4). The p-component of the tip-scattered light was collected. As it can be observed in Fig. 2.8 the obtained near-field images of the p-component of the scattered light are in excellent agreement with numerical calculations of the vertical near-field component E_z.

We performed the experiments at a fixed incident wavelength of $\lambda = 9.3\mu$m

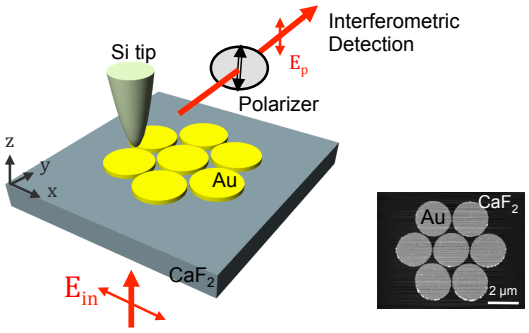

Figure 2.7: **Experimental setup for near-field imaging in transmission-mode.** The heptamer structure is illuminated from below with linearly polarized light. Topography image of a heptamer on top of CaF_2 substrate shown in gray scale on the right. Adapted from [109].

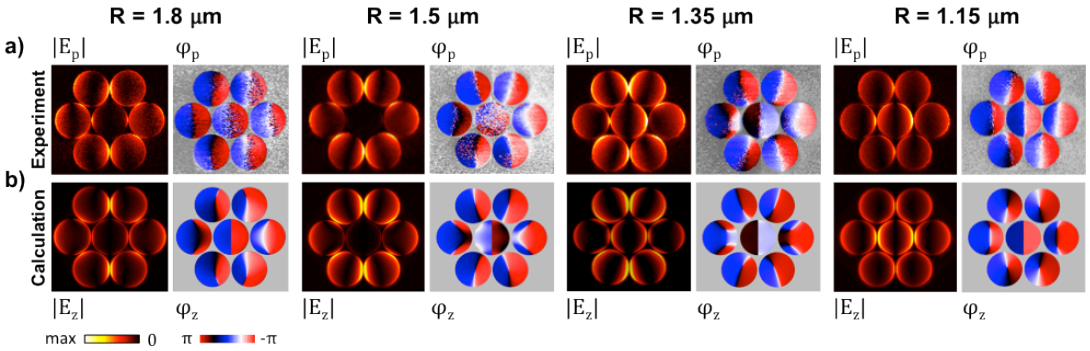

Figure 2.8: **Near-field imaging of differently sized heptamer structures.** Heptamers composed with seven discs of radius R (R being 1.8, 1,5, 1.35, 1.15 μm from left to right) are excited with the same wavelength $\lambda_0 = 9.3$ μm. **(a)** Images of the experimental amplitude $|E_p|$ and phase φ_p of the p-component of the scattered light the differently sized heptamer structures. **(b)** Images of the calculated near-field amplitude $|E_z|$ and phase φ_z of the out-of-plane near-field component for the same heptamers in a). Adapted from [109].

because of the limited wavelength range of the present setup. In order to observe the intensity *toggling* due to Fano interference that occurs upon crossing the "dark" resonance (see ref. [109] for details), we imaged heptamer structures of different sizes. The differently sized heptamer structures were fabricated using e-Beam lithography [109]. In Fig. 2.8b we show the calculated near-field amplitude $|E_z|$ and phase φ_z images of the vertical field component for the differently sized heptamer structures, which are in excellent agreement with the experimental out-of-plane near-field component amplitude $|E_p|$ and phase φ_p (Fig. 2.8c). We can observe how the near-field distribution changes while we cross the Fano dip in the extinction spectra: for both the biggest ($R = 1.8$ μm) and the smallest ($R = 1.15$ μm) heptamer structures, all of the discs show dipolar

resonance pattern [106] with each dipoles oriented in the same direction and oscillating with nearly the same phase. For the heptamers with $R = 1.5$ μm and $R = 1.35$ μm the patterns on the outer discs are similar, however, they are slightly rotated. The most significant change appears on the central disc in both cases. In the case of the heptamer with $R = 1.5$ μm, the central disc appears dark and for the $R = 1.35$ μm disc still exhibits a dipolar pattern, but the fields oscillate about 90° out of phase with the outer discs, as it can be seen in the calculated and experimental phase images. Note that in the case of $R = 1.5$ μm disc, the phase on the central disc does not have any meaning as there is no signal. This experiment showed for the first time a real-space mapping of of Fano interference in plasmonic metamolecules [109].

2.4.2 Near-field verification of retardation among orthogonal dipoles on L shaped antennas

The second example is a "plasmonic metasurface" composed by densely packed gold mirror-imaged L shaped antennas [110] (see Fig. 2.7). This plasmonic metasurface is a quasi-two-dimensional alternative to conventional wave plates used to manipulate the polarization state of light [53]. The polarization state of light is determined by the amplitude and the phase relationship of two orthogonal linear vectors perpendicular to the propagation direction. This structure is designed to modify the phase difference between the those vectors while keeping their amplitudes unchanged. In each single L shaped antenna two orthogonal dipolar modes can be excited and each of the dipoles radiates with linearly polarized light. If the incident light only excites one of the dipoles, this first dipole drives the second one, which will oscillate with some retardation respect to the first one. As a consequence, we obtain two linearly polarized radiation sources, orthogonally polarized and with a phase difference given by the retardation between the oscillating dipoles. In this way, the retardation allows that the plasmonic metasurface can modify the polarization state of the light transmitted through it [110]. The aim of this experiment was to show the retardation among the dipolar modes in the near-field, and thus, prove the microscopic origin of the polarization tuning capability of the metasurface.

In order to prove that this metasurface is able to tune the polarization state of light due to the retardation between the two dipolar modes on each L shaped antenna, me map a cell composed by two mirror-images L shaped antennas within the metasurface with our transmission-mode s-SNOM. In Fig. 2.9b we show the topography image of

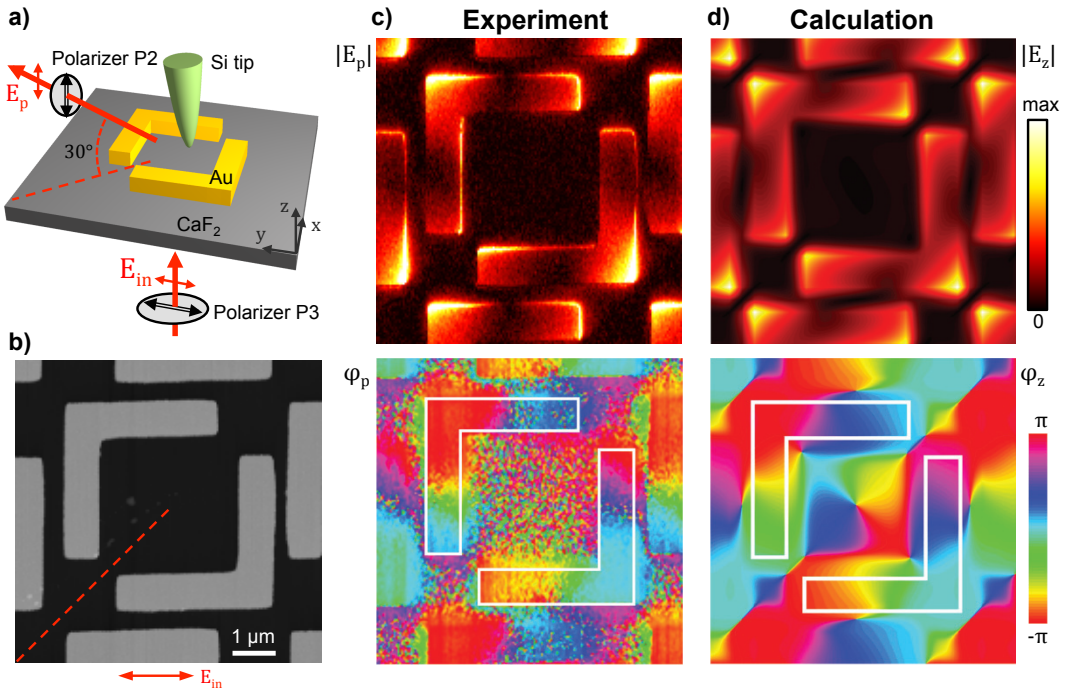

Figure 2.9: **Near-field imaging of plasmonic metasurface composed of L shaped antennas.** **(a)** Experimental setup for near-field imaging in transmission-mode, where the L antennas are illuminated from below with a wavelength of $\lambda_0 = 9.3$ μm. The light is linearly polarized parallel to one of the antenna arms, which can be tuned rotating the Polarizer P3. **(b)** Topography image of a single cell of the metasurface composed by two gold mirror-imaged L shaped antennas on top of CaF_2 substrate. The structure is illuminated with light polarized along the horizontal antenna arms and the red dashed line indicates the projection of the detection direction, also mark in **(a)**. **(c)** Experimental amplitude $|E_p|$ (top) and phase φ_p (bottom) images p-component of the scattered light of a single cell of the metasurface. **(c)** Calculated amplitude $|E_z|$ and phase φ_z of the vertical near-field component of the single cell of the metasurface 10 nm above the structure. Adapted from [110].

the mapped cell, where the projection of the detection direction is indicated with a red dashed line and the incident light is polarized horizontally along the double red arrow. Simultaneously to the topography image, we obtained the amplitude and phase of the p-polarized scattered field E_p images (Fig. 2.9c), which are in excellent agreement with the calculated amplitude and phase of the vertical near-field component E_z (Fig. 2.9d). From the amplitude images (top images in Figs. 2.9c and d) we can observe that both arm ends in each L shaped antenna are bright, meaning that both horizontal and vertical dipole modes are excited. However, the phase distribution in each arm is different. If we look at phase distribution of the bottom right L shape antenna (bottom images in Figs. 2.9c and d), we find that the phase on the left end of the horizontal arm is about $-135°$ (orange in color) and the phase on the top end of the vertical arm is about $135°$ (pink in color). Therefore, the phase of the horizontal dipole is about $90°$ ahead of the

phase of the vertical dipole, confirming the time retardation between the two dipolar modes on the L shape antennas [110].

2.5 Interpretation of near-field images

The interpretation of the images obtained with the polarization-resolved s-SNOM has significantly evolved in recent years. In previous works, the p-polarized scattered field E_p was directly compared to the vertical or the out-of-plane near-field component, E_z [80, 86, 109, 111] while the s-polarized scattered field E_s was directly compared to the horizontal or the in-plane near-field component, E_x (or E_y) [32, 99] on the plasmonic structure. This interpretation has been supported by the good agreement shown between the experimental p-polarized scattered field E_p (s-polarized scattered field E_s) and the numerically calculated out-of-plane near-field component E_z (in-plane near-field component E_x or E_y), as it can be seen e.g. in Fig. 2.7. Later on, more quantitative works [112] showed that the direct comparison between detected fields (E_p and E_s) and the local near-field components (E_z and E_x or E_y) was not always fulfilled.

A recently developed model [113] has been able to rebuilt the experimental images for linear antennas [113] and even spiral antennas (see Chapter 6 and [114]) in an elegant and simple way, which allows to identify the excited plasmonic modes from the experimental images. This model takes into account multiple scattering events between the tip and the sample, as well as the combination of the different near-field components in the s-SNOM signal, depending on the illumination and detection conditions. As it has been shown with the help of this model, in general, the fields detected with polarization-resolved s-SNOM do not correlate with a single component of the local near-field, but with a complex-valued combination of different near-field components at each point [113]. The signal measured in s-SNOM at a given position involves weighted sum of individual local near-field components at that position. Furthermore, depending on the detection scheme selected (s- or p-polarization and scattered light collection direction relative to the structure), scattered fields scale different as a function of the local near-field enhancement [113]. Being the signal detected for the s-polarized field a linear combination of squared local near-field components, while the signal detected for the p-polarized field is given by linear combination of local near-field components [113]. For a linear antenna mapped as in Fig. 2.1, E_s and E_p can be written as

$$E_s \propto \frac{\alpha_x^T E_x^2 + \alpha_y^T E_y^2 + \alpha_z^T E_z^2}{E_{in}} \tag{2.15}$$

$$E_p \propto \left(\alpha_z^T E_z - \alpha_y^T E_y\right) \tag{2.16}$$

where E_i with $i = x, y, z$ are the near-field components of the antenna and α_i^T with $i = x, y, z$ are the diagonal term of the tip polarizability tensor.

Most of the work presented in this thesis is prior to the development of this model. That is the reason why the model is not taking into account until the Chapter 6 and even there it is apply to obtain a qualitative agreement because of the complexity of the structures analyzed.

2.6 Conclusions

We have demonstrated that our transmission-mode s-SNOM is a versatile and powerful technique for near-field mapping of extended plasmonic structures. We apply our transmission-mode s-SNOM to obtain a full characterization of plasmonic structures, which requires resolving their local optical field distributions with a subwavelength resolution. The presented near-field images of p-polarized scattered light for heptamer structures and the L-shaped antennas show an excellent agreement with the calculated out-of-plane near-field component. In addition, we have shown that propagating modes can be also characterized (see Chapter 5) using the transmission-mode s-SNOM. Furthermore, with the help of the model that relates the detected signal with the local near-field components on the plasmonic structure we are able to interpret complicated near-field modes as in spiral antennas (see Chapter 6). This promising results will provide a full and reliable characterization of complex optical plasmonic structures, which can be used as optical circuits, optical metasurfaces or molecular spectroscopy.

Chapter 3

Propagation and Nanofocusing of Infrared Modes on Tapered Transmission Lines: Influence of the Substrate

In this chapter we study the propagation of mid-infrared modes on non-tapered and tapered two-wire transmission lines (TLs) on Si and CaF_2 substrates, the two materials representing for substrates with large and small refractive index, respectively. A comparative numerical study predicts a larger mode wavelength and an increased propagation length (i.e. weaker damping) for the CaF_2 substrate. By near-field microscopy we image the near-field distribution along the TLs and experimentally verify mode propagation. Amplitude- and phase-resolved near-field images of a non-tapered TL on CaF_2 reveal a standing wave pattern caused by back-reflection of the modes at the open-ended TL. Calculated and experimental near-field images of tapered TLs on Si and CaF_2 demonstrate that for both substrates the mid-IR modes are compressed when propagating along the taper. Importantly, the nanofocus at the taper apex yields a stronger local field enhancement for the low-refractive index substrate CaF_2. We assign the more efficient nanofocusing on CaF_2 to the weaker damping of the modes.

3.1 Introduction

Recently, we succeeded to nanofocus mid-IR modes with tapered two-wire TLs [32]. However, the propagation length of mid-IR modes on two-wire (coplanar strip) TLs [115] was observed to be rather short, in the range of 10 μm, which is in the order of the free-space wavelength [31, 32]. Such short propagation lengths challenge the development of mid-IR nanophotonics and limit the maximum field enhancement at the apex of tapered TLs. On the other hand, the reported mid-infrared TLs were fabricated on Si substrates, which have a rather large refractive index, $n_{Si} > 3$ at mid-IR wavelengths [49]. It is well known that substrates with a large refractive index strongly affect the near-field enhancement and damping of surface plasmon polaritons [116]. Here we study the influence of the substrate on the propagation of mid-IR modes on two-wire TLs. Particularly, we compare the performance of tapered TLs on Si and CaF_2 substrates, the latter exhibiting a much lower refractive index of $n_{CaF_2} \approx 1.3$ [49] at 9.3 μm wavelength. To this end, we fabricated two-wire TLs on a CaF_2 substrate, image their IR near-field distribution and compare the results with recently published data [32] obtained for TLs on Si.

3.2 Numerical studies of mid-IR TLs

Fig. 3.1a shows the cross section of a typical two-wire TL on a dielectric substrate, which consists of two infinitely long parallel metallic wires. We define the total width of the TL by $W = 2w + g$, where w is the width of the metal wires and g the distance between them. In Fig. 3.1b we show the calculated mode profiles (intensity) for two-wire TLs on a CaF_2 substrate for different widths W. The calculations were performed with a commercial mode solver (www.lumerical.com). From the set of solutions we have selected the antisymmetric mode, where the fields on the parallel wires oscillate 180° out of phase (illustrated by + and − signs in Fig. 3.1b). As we show later in Fig. 3.4, this mode is the one that is excited and propagates along the TL by attaching a dipole antenna to it [117]. For all calculations we assume a free-space wavelength of $\lambda_0 = 9.3$ μm and use the dielectric values for Au and CaF_2 from Palik [49] ($\epsilon_{Au} = -2591 + 1145i$; $\epsilon_{CaF_2} = 1.74$). We find that the near fields associated to the infrared modes are strongly confined on the scale of the TL width W, even for the narrowest case C with $W = 90$ nm ($\lambda_0/100$). Similar field confinements have been reported for TLs on Si [31,32].

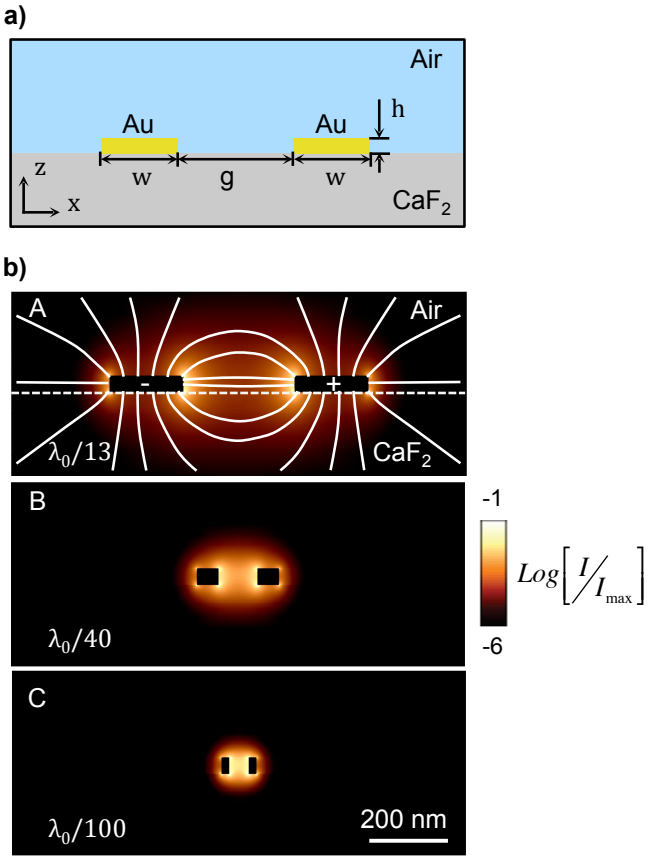

Figure 3.1: **Two-wire TLs on a CaF_2 substrate.** **(a)** Schematics of the cross section. **(b)** Numerically calculated mode profiles which are excited at $\lambda_0 = 9.3$ μm wavelength. Mode profiles are plotted for three situations A, B and C, in which the total width ($W = 2w + g$) is 700 nm, 212 nm and 90 nm, respectively. The mode profiles are normalized to their maximum value.

In order to compare the performance of TLs on the two different substrates, CaF_2 and Si, we display in Fig. 3.2a the mode wavelength λ_m and in Fig. 3.2b the propagation length L as a function of the total width $W = 2w + g$, where the gap width g increases linearly from 50 nm to 300 nm and the wire width from $w = 20$ nm to 200 nm. Following our previous work on near-field mapping of TLs [32], we define the propagation length L as the distance where the field amplitude decays by a factor of $1/e$. For both the CaF_2 (blue curves) and Si (red curves) substrate the mode wavelength λ_m decreases when the width W of the TL is reduced, as the overlap between the mode profile and the metal increases [118]. We also see that λ_m is larger by about a factor of two on the TLs on CaF_2. This can be explained essentially by the lower refractive index of the CaF_2 substrate. When considering the TL being embedded in a homogeneous medium with an effective refractive index n_{eff} given by [119]:

$$n_{eff} = \sqrt{\epsilon_{eff}} = \sqrt{\frac{\epsilon_{air} + \epsilon_{subs}}{2}} \tag{3.1}$$

We obtain $n_{eff,Si} = 2.28$ for the TL on Si and $n_{eff,CaF_2} = 1.17$ for the TL on CaF_2. In comparison, the effective refractive index for CaF_2 in the half as large as the one for Si, which explains why the mode wavelength on Si is a factor of two smaller.

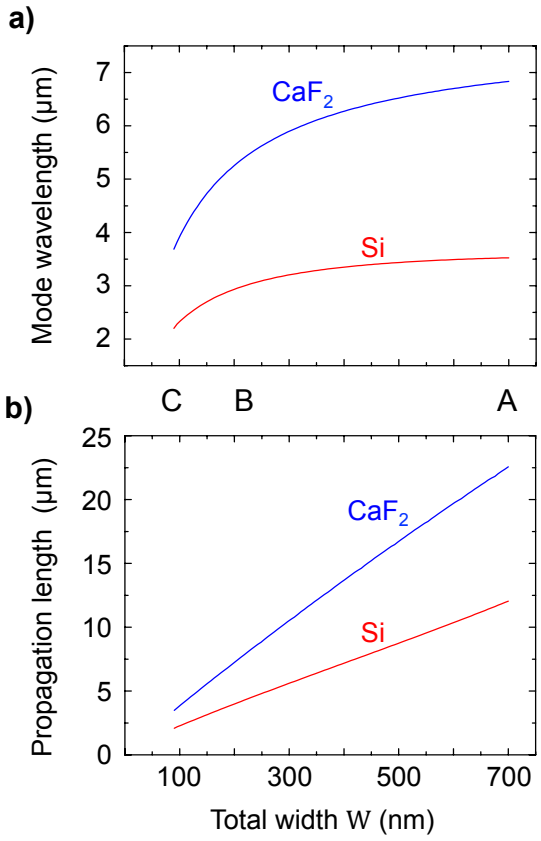

Figure 3.2: **Propagation properties of infrared modes on two-wire TLs of total width W.** **(a)** Mode wavelength. **(b)** Propagation length as a function of the total TL width ($W = 2w + g$) on CaF_2 (blue curves) and on Si (red curves) substrates, while the wire width w and the gap size g are decreased simultaneously from $w = 200$ nm to 20 nm and $g = 300$ nm to 50 nm. The letters A, B and C indicate the TLs shown in Fig. 3.1b.

We also find that on both substrates the propagation length L decreases for smaller W. This can be attributed to the increasing amount of energy propagating inside the gold (skin depth effect) [30,32], yielding damping of the mode because of the losses inside the metal. We also find that the propagation length L is about a factor of two smaller on the TLs on Si. The higher refractive index of Si makes the optical field to be more confined, increasing the field magnitude at the Au-Si interface (and inside

the gold) and resulting in a greater absorption loss [116,120]. Our numerical study thus suggests to employ low refractive index materials for the development of mid-IR TLs, particularly for nanofocusing mid-IR light in tapered TLs as we show later in Fig. 3.5.

3.3 Near-field microscopy of mid-IR TLs

We experimentally study two-wire TLs on a CaF_2 substrate by imaging their near-field distribution with a scattering-type Scanning Near-Field Optical Microscope (s-SNOM)[79]. In order to launch a mode (Fig. 3.1b) along the TL, a dipole antenna is attached to the left end of the TL [31,32]. Fig. 3.3 illustrates the imaging principle. A conventional, cantilevered silicon (Si) tip is used as a near-field probe, scanning the TL. The tip apex scatters the local near field of the IR mode [31, 32, 121, 122] (illustrated schematically by red curved lines over the TL), which is subsequently detected by a distant detector in the far field. The TL is illuminated from below through the transparent substrate (transmission-mode s-SNOM [32, 97]), with a polarization parallel to the dipole antenna. This way the antenna is efficiently excited and launches a mode along the TL. The tip, in contrast, is only weakly polarized, which prevents disturbance of the near-field distribution of the TL [80,86,96,97]. Transmission-mode s-SNOM has been already used successfully to image the mid-IR near-field distributions of infrared antennas and TLs on Si substrates [32, 97, 99, 123].

Further details of the setup used in this work are described in Chapter 2. A CO_2 laser tuned at a wavelength $\lambda_0 = 9.3$ μm is weakly focused to the sample through a low-numerical aperture objective, yielding a mid-IR spot of about 50 μm in diameter for the purpose of homogeneous sample illumination. The background contributions are fully suppressed by vertical tip oscillation at a frequency Ω (about 300 kHz) and subsequent higher harmonic demodulation of the detector signal at 3Ω (see Chapter 2 for details). The tip-scattered light is detected with a pseudo-heterodyne Mach-Zehnder interferometer [92], where a piezo-actuated mirror (PZM) is oscillating at frequency M ($\sim$600 Hz), in order to modulate the vertically polarized the reference beam (with polarizer P1 set vertically, see Fig. 2.5). Thus, by demodulating the detector signal at frequencies M + 3Ω and 2M + 3Ω, both amplitude $|E_p|$ and phase φ_p images of the p-component of the tip scattered light can be recorded simultaneously to the topography [32, 97, 99, 123].

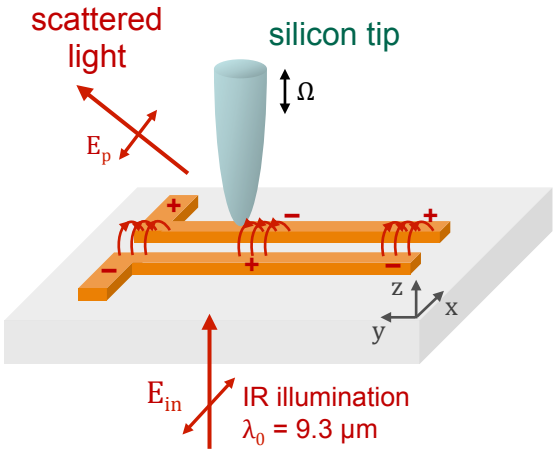

Figure 3.3: **Principle of transmission-mode s-SNOM**. A silicon tip is scattering the near-fields from the TL that is illuminated from below through the substrate with polarization parallel to the dipolar antenna. The scattered light is collected above the surface in y-direction at an angle of about 60° normal to the surface. The near field scattered by the silicon tip is detected with a pseudo-heterodyne interferometer, yielding amplitude and phase images of the p-polarized scattered light.

3.4 Fabrication of mid-IR TLs on a CaF_2 substrate

The two-wire TLs were fabricated by high-resolution e-beam lithography and metal lift-off. A bilayer of polymethyl methacrylate (with molecular weight of 495 kDa at the bottom and 950 kDa at the top) was used as electron-sensitive polymer. Because CaF_2 is an insulator, the surface of the substrate is charged when exposed to the electron beam, which can deviate the beam. In order to avoid charging of the sample, a 1.5 nm thick gold layer was sputtered on top of the electron-sensitive polymer. After the electron beam exposure the sputtered gold layer was etched with solution of KI_3 ($KI+I_2$). The sample was then developed in methyl isobutyl ketone (MIBK) and isopropanol alcohol (IPA) mixture of ratio 1:3. Then a 40 nm gold film was thermally evaporated in high vacuum on top of 3 nm thick titanium layer, which before was electron beam evaporated onto CaF_2 substrate for adhesion purposes. Finally, a lift-off was done by immersion of the sample in acetone for about 4 hours, followed by about 15 s of ultrasound treatment and IPA rinse.

3.5 Experimental verification of mid-IR TLs on a CaF_2 substrate

We first verify the propagation of the infrared mode on a 6 μm long two-wire TL on CaF_2, which has a total width of $W = 700$ nm (cross section A in Fig. 3.1b). Fig. 3.4a shows the topography image of the TL and the dipole antenna attached at its left end. The amplitude $|E_p|$ and phase φ_p images of the p-polarized scattered light are shown in Fig. 3.4c. We observe strong near-field amplitude signals on the parallel metal wires, which prove that the antenna couples an IR mode into the subwavelength-scale TL. The 180° phase jump between the two wires proves that the mode is antisymmetric, i.e. the near fields on the two parallel wires oscillate in antiphase as indicated by the plus and minus signs in the phase image. We also observe amplitude maxima and minima along the parallel wires. They reveal a standing wave pattern, which is confirmed by the phase jump of 180° along the wires. The standing wave pattern on the TL is generated because of the back-reflection at the right open end of the TL, where the wave finds an impedance mismatch [31]. From the standing wave pattern we measure that the distance between minima is about 3.5 μm, which is the half of the IR mode wavelength, $\lambda_m/2$. This is in excellent agreement with the theoretically expected wavelength $\lambda_m = 7$ μm (see position A in Fig. 3.2a). For comparison we performed numerical calculations with a commercial software package (www.lumerical.com). We consider a homogenous plane wave illumination from below. In Fig. 3.4d we show the amplitude and the phase of the vertical near-field component ($|E_z|$ and φ_z) at 30 nm above the TL. We see that our experimental results are well reproduced by numerical calculations.

3.6 Comparative study of mid-IR nanofocusing with tapered TLs on Si and CaF_2 substrates

In Fig. 3.5 we compare experimentally and numerically the nanofocusing capabilities of tapered TLs on CaF_2 and Si substrates. To that end we imaged and calculated the near-field distribution of a 6 μm long tapered TL on CaF_2 substrate (Fig. 3.5a) and compare it with the results obtained for a TL of the same geometry on Si (Fig. 3.5b, numerical and experimental data taken from ref. [32]). As seen in the topography images (Figs. 3.5a and 3.5b, top), we tapered the right open end of the TLs over a length of 1 μm by reducing the total width W of the TL linearly from 700 nm (case A in Fig. 3.1b) to 90

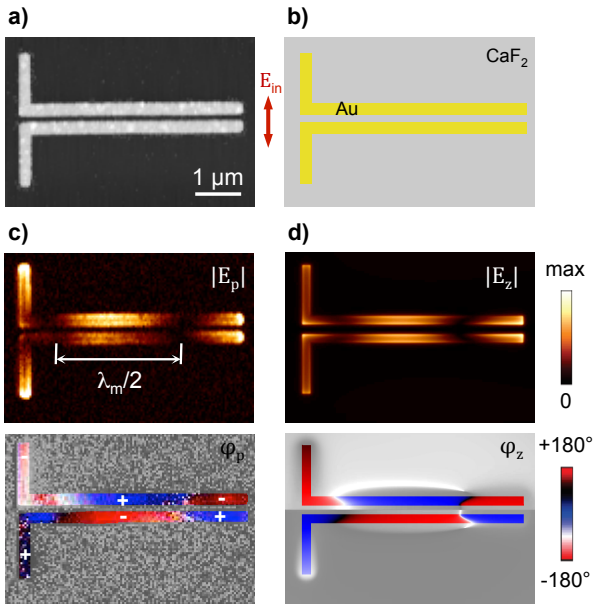

Figure 3.4: **Near-field images of a two-wire TL. (a)** AFM topography. **(b)** Geometry used for numerical calculations. **(c)** Experimental near-field images showing amplitude $|E_p|$ (top) and phase φ_p (bottom) of the p-component of the scattered light. **(d)** Numerically calculated near-field images showing amplitude $|E_z|$ (top) and phase φ_z (bottom) of the vertical near-field component. Numerical calculations show the near-field distribution 30 nm above the TLs. The phase images are displayed is a cyclic colour scale where white colour represents -90°, blue 0°, black 90° and red ±180°.

nm (case C in Fig. 3.1b). Both TLs were imaged with our transmission-mode s-SNOM [97] at a wavelength of $\lambda_0 = 9.3$ μm. The experimental (Figs. 3.5a and 3.5b, middle) and calculated (Figs. 3.5a and 3.5b, bottom) near-field images show the intensity of p-component of the scattered light I_p and vertical near field component I_z respectively. As for the untapered transmission in Fig. 3.4, we see one interference maximum in the middle of the TL on CaF_2 (Fig. 3.5a), which is caused by a back-reflection of the mode at the open-ended taper. On the TL on Si (Fig. 3.5b) we observe two fringes along the untapered part of the TL, as the mode wavelength is reduced by a factor of two (see Fig. 3.2). More importantly, on both TLs we see a significant increase of the near-field intensity towards the taper apex, which is caused by the compression of the mode when it propagates along the taper [32]. We note that a similar intensity increase occurs for the in-plane (x) near-field component, exhibiting its maximum inside gap at the taper apex as can be shown mapping the s-component of the scattered light [32]. However, the signal for the s-polarized component was much weaker and below the noise level on the untapered part of the TLs. In the following, we thus use the p-component for evaluating and comparing the intensity enhancement at the taper apices.

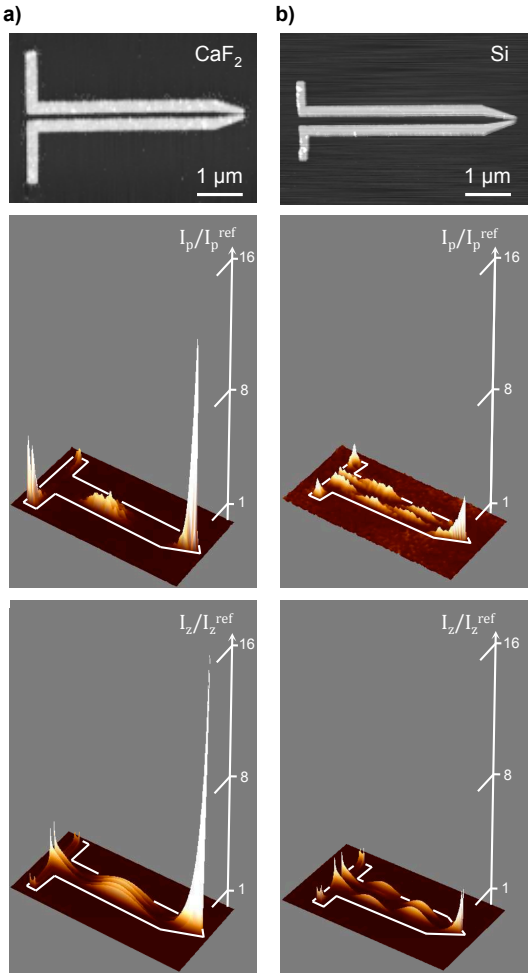

Figure 3.5: **(a)** Topography image of a tapered TL on CaF_2 (top). Near-field images showing the experimental intensity of the p-component of the scattered light $|E_p|^2$ (middle) and numerically calculated intensity of the vertical field component $|E_z|^2$ (bottom). **(b)** Topography image of a tapered TL on Si (top). Near-field images showing the experimental intensity of the p-component of the scattered light $|E_p|^2$ (middle) and numerically calculated intensity of the vertical field component $|E_z|^2$ (bottom). (data taken from ref. [32]).

In order to compare the intensities I_{max} at the taper apices, we normalized the intensity of the measured near-field component I to the value I^{ref} measured at the first interference maximum before the taper, in both experimental and calculated images, and for both substrates. On CaF_2 we find an intensity enhancement $I_p^{max}/I_p^{ref} \approx 14$ in the experiment and $I_z^{max}/I_z^{ref} \approx 17$ in the calculation. In the case of the Si substrate, we obtain $I^{max}/I^{ref} \approx 4$ in both the experiment and the calculation. The intensity enhancement is thus clearly stronger on the CaF_2 substrate, by about a factor of 4. The quantitative discrepancies between experiment and theory we attribute to

fabrication uncertainties particularly at the taper apex. We explain the stronger field enhancement at the taper apex on the CaF_2 substrate to the larger propagation length, i.e. reduced losses of the mode.

3.7 Conclusions

In conclusion, we showed that the propagation length of mid-infrared modes on two-wire TLs is about twice as long on CaF_2 substrates compared to Si substrates. The stronger damping of the infrared modes on the Si substrate is explained by the enhanced interaction between the electromagnetic fields and the lossy metal. We also found that the reduced losses on CaF_2 substrates yield a stronger field enhancement at the apex of tapered TLs. The use of CaF_2 substrates or other low refractive index materials will thus allow for more efficient nanofocusing of mid-IR light, which will be beneficial for the development of integrated mid-IR sensors and near-field probes.

Chapter 4

Focused Ion Beam Fabrication of Plasmonic Structures on Insulating Substrates

In this thesis, the infrared antennas and TL structures studied by near-field microscopy were fabricated by both electron beam (e-beam) lithography and Focused Ion Beam (FIB) milling. The fabrication by e-beam lithography was done in collaboration with the nanodevices group in CIC nanoGUNE, see Chapter 3 for details. However, by e-beam lithography we could not fabricate TLs on CaF_2 with narrow and long gaps (see Chapter 5). Obtaining TLs with high aspect ratio (narrow and long) gaps, however, is a key component for the investigation of the propagation of extremely confined infrared light. Thus, we developed a new fabrication strategy for FIB milling, which enabled us to fabricate functional TLs with gaps of width $g < 50$ nm and length $L > 10$ μm (L:g>10^3:1) on insulating substrates. We applied this strategy to fabricate TLs with 26 μm long homogeneous gaps of 25 nm width and spiral antennas on CaF_2 substrates.

4.1 Overview of e-beam lithography and FIB milling

Nanofabrication by charged particle beams, including electron and ion beams, is extensively used in nanoscience and nanotechnology. Charged particle beams are used for fabrication because they can be focused to spot sizes as small as few nanometers using sophisticated charged particle optics [124].

The e-beam lithography is performed in an electron microscope with patterning software and a focused electron beam. In e-beam lithography, the structure is fabricated in a multi-step process as is shown in Fig. 4.1: Covering the substrate with an electron-sensitive resist (positive or negative) by spin-coating, exposing the resist to an electron beam, developing the exposed patterns, deposition (or etching for negative resist) of the material of interest and lifting-off the resist (see Fig. 4.1).

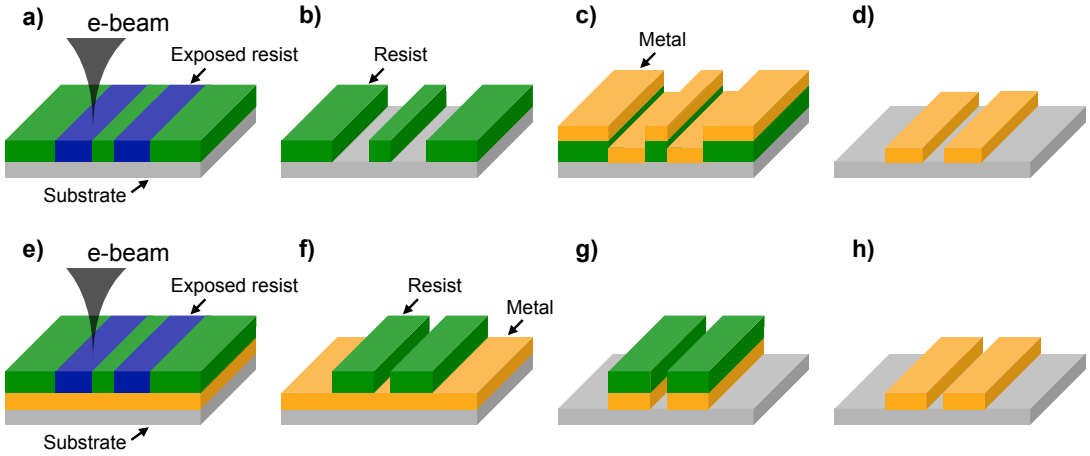

Figure 4.1: **The main steps for an e-beam fabrication process using positive (a-d) or negative resist (e-h).** The polygons in grey color represent the substrate, the yellow ones the metal, the green ones the resist and the blue ones the resist exposed to the e-beam. **(a)** Exposure of the pattern on a positive resist by e-beam. **(b)** Developing process for a positive resist, the exposed part is removed. **(c)** Deposition of the metal of interest. **(d)** Lift-off of the resist. **(e)** Exposure of the pattern on a negative resist by e-beam. The metal of interest has been previously deposited. **(f)** Developing process for a negative resist, only the exposed part remains on top of the sample. **(g)** Etching the metal that is not protected by the resist. **(h)** Removal of the resist. Adapted from [125].

We have used e-beam lithography to fabricate various IR TLs on an insulating substrate (calcium fluoride CaF_2) using a positive resist (polymethyl methacrylate, PMMA [126]), and a slightly modified fabrication process in order to avoid the deflection of the electron beam (see Section 3.4 on Chapter 3 for details). However, fabrication by e-beam lithography has some disadvantages for fabricating TLs with long (above 10 μm) and extremely narrow (below 50 nm) gaps [127,128]. E-beam lithography is not an ideal technique for the fabrication of challenging structures: When exploring its limits one needs to go through the whole process for observing whether the fabrication has been successful or not. This drawback can be circunvented by fabricating a large number of structures at the same time, but with slightly different fabrication parameters and then selecting the best structures. More importantly, the principal drawback of e-beam lithography for fabricating TLs with high aspect ratio gaps is the need for solvents

to remove the resist and obtain the final structure. When fabricating high aspect ratio gaps the solvent is often not able to completely dissolve the resist inside the gap. Consequently the gap may partially remain closed after the lift-off process. The need for solvents and a lift-off process is an inherent problem of e-beam lithography.

In order to obtain functional TLs with high aspect ratio gaps, a promising alternative to e-beam lithography is FIB milling. Ions have a heavy mass compared to electrons, which make them particularly suitable for nanofabrication by direct structuring of a material [124]. FIB milling does not require exposing a pattern to the ion beam prior to material deposition. FIB milling is a two step process: deposition of the material and milling the material by exposing it to a focused ion beam (see Fig. 4.2).

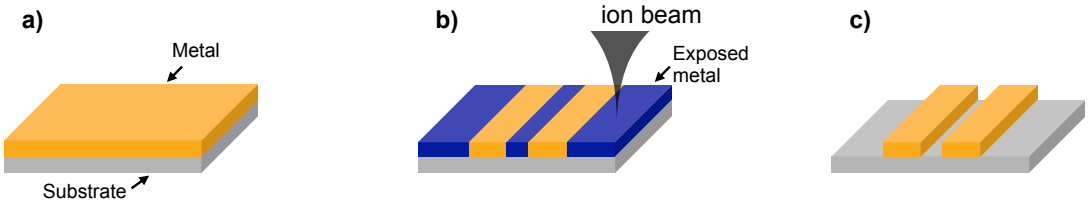

Figure 4.2: **The two steps for a FIB milling fabrication process.** The polygons in grey color represent the substrate, the yellow ones the metal and the blue ones the metal exposed to the ion beam. **(a)** Deposition of the material. **(b)** Milling the material by exposing it to FIB. **(c)** Structure fabricated after milling in **(b)**.

Because of the direct milling of the exposed area, imaging the sample with the ion beam should be avoided. This is the reason why ion columns are usually incorporated into dual-beam microscopes, which are combine an ion column with an electron column[1] (see Fig. 4.2). The dual-beam microscopes offer the possibility to verify in-situ whether or not the fabrication has been successful with no subsequent damage to the structure from the use of the incorporated Scanning Electron Microscope (SEM). By successive FIB milling and SEM imaging we are able to optimize the milling parameters for a complicated structure in a single fabrication session as described in Section 4.3.

The dual-beam microscopes available at CIC nanoGUNE (FEI Helios DualBeam NanoLab 600 and NanoLab 450S) have a field emission electron gun and liquid metal ion source (LMIS). The electron beam is focused and collimated with electromagnetic lenses. It is scanned across the sample surface with a electrostatic scanning system.

[1]Nowadays there are some dual-beam FIB microscopes that do not have an e-beam but a helium ion beam instead, which is used for both imaging and extremely fine milling. Imaging with He ion beam also mills the structure but it is negligible compared to one caused by heavier ions like Ga used commonly.

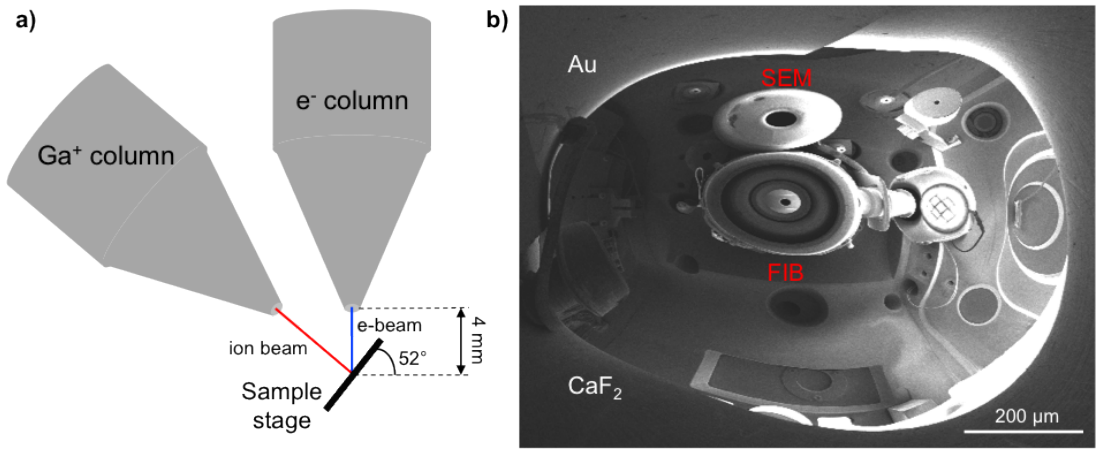

Figure 4.3: **Dual-beam microscope (a)** Schematic of a dual-beam microscope showing the electron column, ion column and the sample stage tilted by 52° to be perpendicular to the ion beam. **(b)** SEM image of the dual-beam microscope from point of view of the sample showing the position of the electron column and the ion column inside the fabrication chamber. The area of the substrate of CaF_2 with no gold on top, gets charged and becomes a mirror for electrons.

The ion beam is focused and collimated with electrostatic lenses and it is scanned with its own electrostatic scanning system. The ion column by construction is inclined by 52 degrees to the vertical direction. In order to achieve perpendicular milling relative to the sample surface, the stage must be tilted by 52° from the horizontal position (see Fig. 4.3).

Within this thesis, 1 mm thick CaF_2 crystals were used as substrate for the antennas and TLs. CaF_2 was chosen because of its many properties that facilitate the near-field characterization of the samples with the s-SNOM: (i) It is transparent at mid-IR wavelengths (around 10 μm), (ii) it has a low refractive index, which improves the antenna properties compared to Si substrate (see Section 3.2 on Chapter 3 for details), (iii) it is commercially available with double-sided polishing, which is important for transmission-mode experiments, (iv) it is stable to humidity and (v) it is not poisonous. However, it has a drawback from the point of view of nanofabrication by charged particle beams; CaF_2 is an insulating substrate which leads to deflection of the beam and thus errors in the structuring process.

For e-beam lithography the problem of charging is overcome by sputtering few nanometers of gold on top of the electron-sensitive resist (see Section 3.4 on Chapter 3 for details). In the case of FIB milling we have to fabricate the structure in such a way that it is grounded while the area around it is being milled away. This avoids charging

of the sample and subsequent beam deflection. For that reason we designed a milling process that guaranties that every structure is grounded during the milling process. In the following we explain the milling process we have developed for the fabrication of plasmonic structures on insulating substrates, from the design of the milling process to the optimization of the milling parameters. All the examples shown in this Chapter were fabricated at CIC nanoGUNE employing a Gallium ion beam.

4.2 Design of the milling process

First of all, the pattern to be exposed to the ion beam has to be designed. As the material on the exposed surface is removed by FIB (see Fig. 4.2), the pattern needs to be the inverse of the final structure. This is illustrated in Fig. 4.4. First, the final structure (white circles in Fig. 4.4a) with a polygon around it (white rectangle around the circles in Fig. 4.4a) is drawn for example in AutoCad. Then, in a second program (LayoutEditor^{TM} ©2007 Jürgen Thies), the structure is inverted using Boolean operators to obtain the pattern to be exposed (blue polygon in Fig. 4.4b, resulting from subtracting the eight circles from the rectangle) and saved as a `.gds` file[2]. When the area to be milled (marked in blue in Fig. 4.4b) is scanned by the ion beam, the material within this area is removed, opening a window with the final structure inside (the eight discs inside the rectangular window in Fig. 4.4b). Thus, the polygon drawn around the structure (white rectangle in Fig. 4.4a) defines the window that is opened.

Fig. 4.4b represents the simplest pattern of a milling process where there is only one polygon (the blue one). Because the pattern consist of one single polygon, only one set of milling parameters (beam current, dwell time, pitch, ...) is used to mill the pattern. However, more often, as it is sketched in Fig. 4.5, different sets milling parameters are needed to fabricate a structure. The milling process should be fast and at the same time provide high resolution. However, a fast milling process requires high beam current (high dose) and a milling process with high resolution requires low current (small beam diameter, see *Milling parameters* in section Fabrication for more details). In addition, if the substrate is an insulator, the structure being fabricated needs to be grounded during the milling process. This is a key aspect of the design of the milling process for insulating substrates: Every piece of metal to be milled needs to be connected to the

[2]The AutoCad file must be saved as `.dxf` in order to open it in Layout. Then we can manipulate the pattern and save it as a `.gds`.

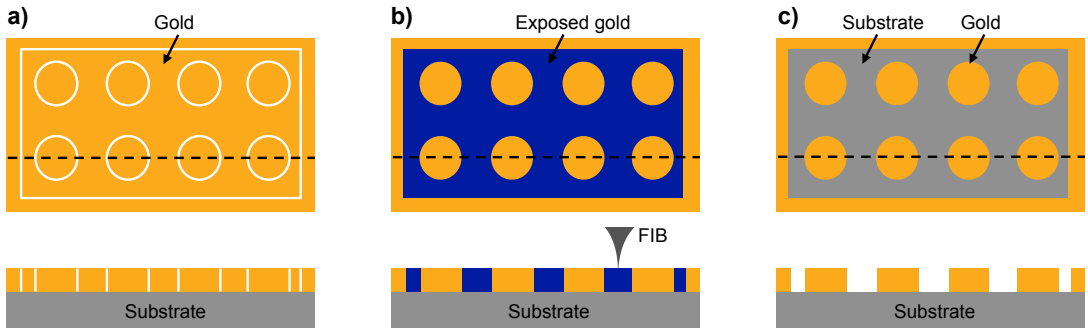

Figure 4.4: **Design of the pattern to expose with FIB. (a)** Drawing of eight circles surrounded by a rectangle (white lines) superposed on a gold film (yellow) over a substrate (grey), top view (top) and cross section of the sample along the black dashed lines (bottom). **(b)** Pattern to expose with FIB (blue polygon), resulted from subtracting the eight circles to the rectangle, superposed on a gold film (yellow) over a substrate (grey), top view (top) and cross section of the sample along the black dashed lines (bottom). **(c)** The sample after milling the blue polygon in (b) with FIB, showing the window opened on the gold film with eight gold discs inside, top view (top) and cross section along the black dashed lines (bottom).

grounded metal film (see Fig. 4.5 below). In this way, the area being milled does not get charged, and the milling is performed with the required precision. In order to solve these problems, the pattern is separated into different polygons, and these polygons are located in different layers. Different milling parameters used for different purposes (e.g. low current for high resolution milling) are defined in each layer. A layered pattern also allows for milling the different polygons in the desired order (layer by layer).

In Fig. 4.5 we show a typical milling process to fabricate a linear metallic antenna (thin rod) on an insulating substrate. Fig. 4.5a shows the pattern that is used to fabricate the antenna (Fig. 4.5b-f). Each polygon (blue, green and red) is located in a different layer and is milled with different milling parameters. The blue polygon is the first one to be milled (Fig. 4.5c). Its function is to open a window (of e.g. 30 μm $\times$ 30 μm) around the final structure (Fig. 4.5f). For the blue polygon the resolution is not critical and we can use a high current[3] (e.g. 500 pA) in order to minimize the milling time[4]. Next, the green polygon is milled (Fig. 4.5d). In this step, the metal around the antenna is milled, which requires higher resolution to precisely define the metal structure. As it is a small area to mill (the width of the green area is about 400 nm all around the antenna), a lower beam current (e.g. 30 pA) is used. To finish the

[3]Here we only mention the beam current because is the main delimiter among the milling parameters, see *Milling parameters* in section Fabrication.

[4]There is also a technical reason to use a high current: Milling a big area with low current requires a lot of memory because beam radius is smaller and you need a smaller pitch to get the same coverage. In this cases the software we use may crash.

fabrication, the red polygon is milled (Fig. 4.5e) to obtain the final structure (which then becomes electrically isolated). In this case we use the same parameters as for the the green polygon, so that all the surrounding area of the antenna is milled as homogeneously as possible.

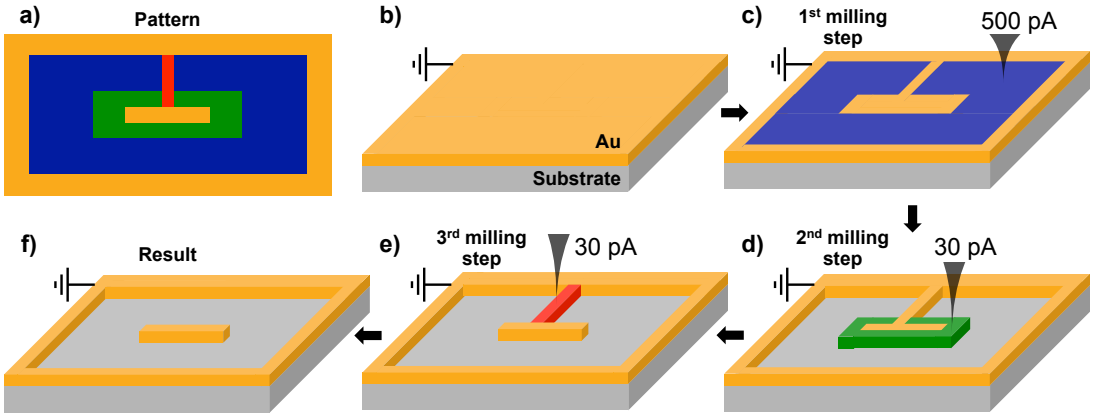

Figure 4.5: **Three milling step process for a metallic antenna on an insulating substrates.** **(a)** Pattern (blue, green and red polygons) to expose with FIB, superposed on a gold film (yellow). **(b)** Grounded gold film over an insulating substrate (grey) where the pattern in **(a)** is transferred. **(c)** The blue polygon (on the first layer) of the pattern is milled away with an ion beam current of 500 pA, opening a window on the gold film. **(d)** The green polygon (on the second layer) is milled away with an ion beam current of 30 pA, precisely defining the antenna. **(e)** The red polygon (on the third layer) is milled away with an ion beam current of 30 pA, electrically isolating the antenna and finishing its fabrication. **(f)** Final structure, gold antenna on a insulating substrate

In some cases, the samples can be left connected to the grounded metal film through the contacts, e.g. the TLs analysed on Chapter 5. As shown in Fig. 4.6, the TLs are still connected after the fabrication, as the connection does not influence the function of the TL.

The area exposed to the ion beam is always bigger than the area defined by the pattern because of the finite beam diameter. Thus, the obtained structures are smaller (bigger when fabricating holes) than the nominal dimensions. A way to anticipate this size discrepancy is to modify the sizes on the patterns from the beginning. Typically the patterns should be modified by adding about 30 to 50 nm (for typical beam currents of 10 to 100 pA) to every feature of the structure. Usually, these modifications avoid many trial and error iterations that are usually needed when starting from the nominal dimensions.

It is important to note that different beam currents might be focused to slightly displaced spots relative to each other on the sample surface. In order to correct the

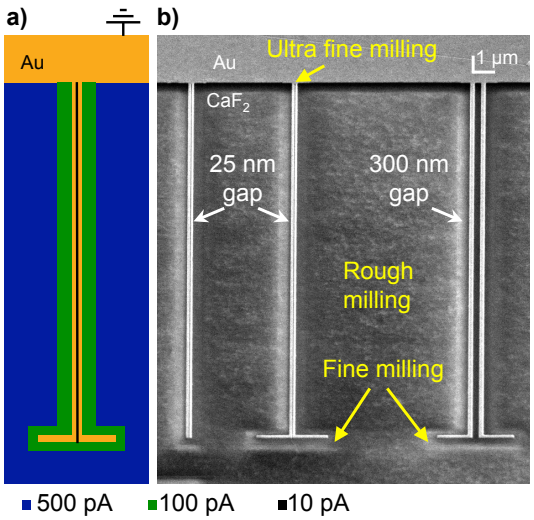

Figure 4.6: **FIB fabrication of gold TLs with different gap sizes on CaF_2 substrate. (a)** Pattern (blue and green polygons and black line) to expose with FIB over a gold film (yellow) using three beam currents in the following order: 500 pA (blue, rough milling), 100 pA (green, fine milling), 10 pA (black line, ultra-fine milling). **(b)** SEM image (taken at 52° stage tilt) of gold TLs with different gap sizes on CaF_2 substrate.

spatial shift between beams with different currents used during milling, the pattern to be exposed needs to include a correlation feature (typically a cross, see Fig. 4.9 or 4.10b). The correlation feature is imaged using the ion beam, during the milling process. Then, to prevent milling the final structure it is important to locate the correlation feature as far as possible from our final structure within the pattern (see Fig. 4.10b). How the correlation feature is employed to correct the shift between the current is explained in section 4.3.5.

4.3 Fabrication

4.3.1 Evaporation of gold on CaF_2

A film of 30 to 60 nm of gold is evaporated using thermal evaporation (Oerlikon evaporator, UNIVEX 350F, Thermal & e-Beam Evaporator) with low deposition rates of about 0.4 Å/s. The thickness of the gold film is chosen to obtain a compromise between the fabrication quality and the damping of plasmons exited on gold nanostructures. The thinner the gold, the easier it is to get a precise milling, i.e. it is easier to get a uniform

narrow gap. The reason is that the milling is faster[5] and the surrounding area that is being milled is exposed to the beam tails for less time. However, a thin gold film also implies a higher damping for plasmons excited or propagating on the nanostructure. The significant penetration of electric fields into the gold film (skin depth of about 20 nm for wavelengths around 10 μm [44]) defines a lower limit of about 30 nm for the thickness of gold nanostructures in order to avoid damping of the plasmons [44].

The gold is evaporated directly on top of CaF_2 substrates without titanium adhesion layer. This is, in contrast to e-beam lithography where a 3 nm thick titanium layer that was used in order to improve the adhesion between the CaF_2 substrate and the evaporated gold film (see Chapter 3). For FIB milling we do not use a titanium adhesion layer because it is an additional step, it would increases the thickness of the layer to be milled, and moreover, yields additional plasmon damping [129–131]. The absence of the titanium adhesion layer has not affected the reproducibility of the fabrication process.

4.3.2 Location of the Eucentric point

In order to scan the same area with both electron and ions, the electron and ion beam focii have to coincide at the same position on the sample surface. The stage height where this condition is fulfilled is called *eucentric height* or *eucentric point*. In our DualBeam the *eucentric point* is close to 4.1 mm height but needs to be located for each specific sample. This point is achieved through the following process: (i) Focus the electron beam on an unimportant area of the sample (typically an area near the corners or the edges of the sample), (ii) set the stage height to 4.1 mm, (iii) tilt the sample stage by 52° so that the sample surface is perpendicular to the ion beam, (iv) focus the ion beam[6], and (v) focus and superposed to the electron beam properly[7]. After this process both beams are well focused on the same area of the sample surface. It is important to make sure that the ion beam is properly focused every couple of hours and every time the sample stage is moved by more than 100-200 μm.

[5] We need a lower value of the parameter *dwell time* to mill trough a thinner layer.

[6] The best is to use a relatively low current (e.g. 50 pA) and high magnification to focus the ion beam for the first time, in this way we avoid exposing a large area to a high dose of ions, because until we focus we do not know what we are exposing.

[7] A way to do this is by milling a square using high magnification, which shows where the ion beam is and then locate the electron beam on this square by moving the stage up and down and using the beam shift of the electron beam

4.3.3 Milling parameters

The fabrication is done using the software "NanoBuilder ©2013 FEI Company" where the pattern to be exposed[8] (see Fig. 4.4b or 4.5a) is loaded. The milling parameters are optimized as explained in section 4.3.4. As the milling parameters are set for each layer, not for each polygon, the optimizing needs to be done layer by layer. In the case that different layers use the same beam current, it is likely that we can use the same milling parameters for all of them. For example, in Fig. 4.5 the green and red polygons belong to different layers but are milled with the same beam current. If we use the same set of milling parameters, the surroundings of the antenna will be milled as homogeneously as possible. In the following, each of the milling parameters will be discussed in detail, and the typical values that were used during this thesis will be provided:

- **Acelleration voltage.** This parameter defines the voltage used to accelerate the Ga ions, and thus the energy that the ions have when they reach the sample (in NanoBuilder called "energy"). We always set the acceleration voltage to the maximum, which is 30 kV.

- **Beam current.** The parameter beam current defines the ion beam current (measured in amperes) used to mill the polygons of a layer. A higher beam current corresponds to a higher dose (see below) and a larger diameter of the beam focus (see Fig. 4.7). Therefore, a higher beam current provides less milling precision, requires less time (lower dwell time) to mill certain amount of material and less scanning points (bigger pitch) are needed to cover a certain area[9]. For a process where we need to mill some very small features and, at the same time, mill a wide area, we typically use the following beam currents to mill 30-60 nm thick gold film: 500 pA or higher for the layer which outlines the final structure and opens the window around it, 30-100 pA for the layer which circumscribes the final structure except its smallest features, and 10 pA for the layer which mills the smallest features (below 50-80 nm) of the final structure.

- **Dwell time.** The parameter dwell time defines the amount of time that the ion beam sits on each scanning point (pixel). The higher the value of the dwell time,

[8] The pattern has to be loaded in `.gds` format and after boolean operations.

[9] The software NanoBuilder discretizes each polygon in points according to the pitch we require. The amount of points that the software can raster at a time is limited, which as a consequence sets a minimum pitch, and thus a minimum current for a given area. The bigger the area of a polygon the bigger the minimum pitch.

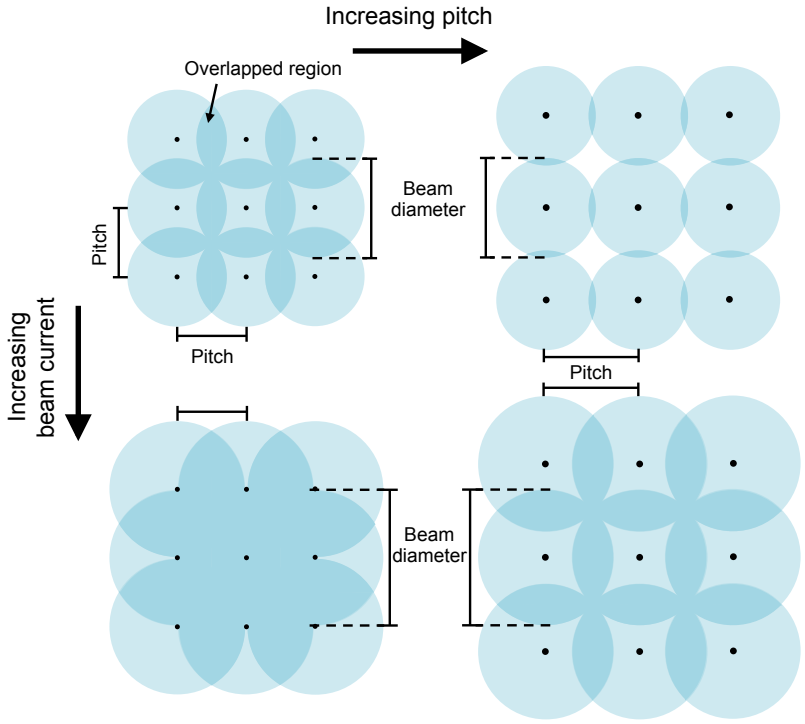

Figure 4.7: **Illustration of the relation between the pitch and the beam diameter with the parameter overlap.** Schematics showing nine neighbouring scanning points (black dots) separated by square pitch, where the ion beam sits while milling. From left to right the pitch is increased while maintaining a constant beam diameter (constant beam current) in each row resulting on a smaller overlap. From top to bottom the beam diameter (beam current) is increased while maintaining a constant pitch in each column resulting on a bigger overlap. Illustrated values for the pitch, beam diameter and overlap (in percentage) respectively are: 5 nm, 7.1 nm, $\sim$ 70% (top left), 6.5 nm, 7.1 nm, $\sim$ 10% (top right), 5 nm, 9.7 nm, 100% (bottom left) and 6.5 nm, 9.7 nm, $\sim$ 70% (bottom right),

the more material is milled (higher dose). The dwell time should be chosen such that just the gold is milled through (without milling the substrate) in the number of passes we set (usually two) as is explained in section 4.3.4 (see Fig. 4.8).

- **Pitch.** The pitch defines the distance between neighbouring scanning points (pixels, see Fig. 4.7). It is set to be smaller than the beam diameter so that at each pixel the beam spot overlaps with the beam spot on the neighbouring pixels (illustrated in Fig. 4.7). The smaller the pitch is the bigger the overlap and thus, more material is milled (higher dose). The pitch needs to be chosen so that when milling with a given dwell time and with a given amount of passes, there are no gold grains left. It can be easily optimized with the same procedure as the dwell time shown in Fig. 4.8. The typical pitch depends on the current we use but it is always such that the beam overlap is 50-60% (sometimes we have increased it up

to 70-80%).

- **Overlap.** This parameter defines the percentage of the beam spot (sitting on a pixel) that is overlapped by the beam spot sitting on the neighbouring pixels as is illustrated in Fig. 4.7. The overlap is a result of having a distance between pixels (the pitch) that is smaller than the beam diameter (see Fig. 4.7). It depends on the beam current (the bigger the current the bigger the beam diameter) and on the pitch, so it is already determined by these two parameters. The overlap is a good reference to set the pitch when we change the current, as it gives a relation between the beam diameter and the pitch.

- **Number of passes.** This parameter defines how many times the milling of the polygons on a layer is repeated. In a usual FIB milling process, a multi-pass strategy is used: it consists in setting a low dwell time and many passes for a given beam current and pitch values. However, multi-pass strategy is not appropriate for fabricating structures on thermally evaporated gold, i.e. polycrystalline gold. The ions penetrations depth into the gold varies due to different lattice orientations on the evaporated gold, the so called channeling[10] effect [132–135]. This means that the milling-rate depends on the grain orientation. If a grain is not milled away in the first pass it probably holds also on the the following passes. Huang *et al.*, solved this problem by using chemically grown single crystalline gold flakes and obtain excellent results compared to vapor-deposited polycrystalline gold [128].

  An alternative way to solve this problem is to optimize the milling process for polycrystalline gold, which is less expensive and easier to prepare than single crystalline gold. We found that for polycrystalline gold it is better to apply the dose in larger portions to neglect the channeling effect, i.e. to mill more in each pass (increase the dwell time and decrease the pitch) while keeping the amount of passes to the minimum. We set the number of passes to 2 (3 at most).

- **Dose.** The parameter dose[11] defines the total amount of ions (amount of charge) reaching the sample per unit area. It also defines the amount sputtered material through the sputtering coefficient. The dose depends on other milling parameters described above: it increases with increasing number of passes, beam current, dwell time and decreasing pitch as can be described by

[10] This effect is often used to identify differently oriented grains by detecting backscattered electrons: channeling contrast [132] or grain contrast [133].

[11] In NanoBuilder the dose is called "fluence". We use the term dose as it more common term in nanofabrication techniques using charged particle beams.

$$\text{Dose} = \frac{\text{Number of passes} \times \text{Beam current} \times \text{Dwell time}}{\text{Pitch}^2} \tag{4.1}$$

If the dose is kept constant while varying the parameters number of passes, beam current, dwell time and pitch, the amount sputtered material is also kept constant. However, the way the material is sputtered is different, and thus the process can be optimized for polycrystalline gold by modifying those parameters.

- **Pattern sequencing.** This parameter sets whether all the polygons on a layer are milled at the same time (parallel) or one after the other (serial). In principle, the preferable option is to mill in *parallel* (all the polygons of a layer are milled as a single unit). However, because of memory limitations, we usually mill in a *serial* fashion. If we choose to mill in *parallel* the software needs to raster all the polygons on that layer first and then it executes the complete layer. However, if we choose to do it in *serial* the software rasters and mills each polygon before starting with the next polygon, which reduces the amount of points the software needs to raster and keep in the memory at the same time. Thus, if we have more than one polygon on a layer, it is preferable to use the option *serial*. In addition, if we have one big polygon which gives us problems because the amount of points it needs for given parameters (pitch and beam current) but we want to keep those parameters unmodified, as an alternative, we can cut the polygon in smaller pieces and mill the pieces in *serial*. Choosing the *serial* option may also have drawbacks when we have a structure that requires a long milling time because the sample may drift causing that some polygons shift relative to each other.

4.3.4 Optimization of milling parameters

Apart from the beam current, only the dwell time and the pitch are independent parameters[12]. These parameters are independent in the sense that we can control them independently, however, the dose depends on both of them. This allows us to tune the dwell time and the pitch such that we obtain well-defined structure even in polycrystalline gold, thus avoiding the inhomogeneities caused by the channel effect [132–135] mentioned above, while keeping the number of passes to minimum.

In order to optimize the dwell time and the pitch, we start with the highest beam current of the milling process because it needs less optimization as its quality is not

[12]The number of passes is set to 2.

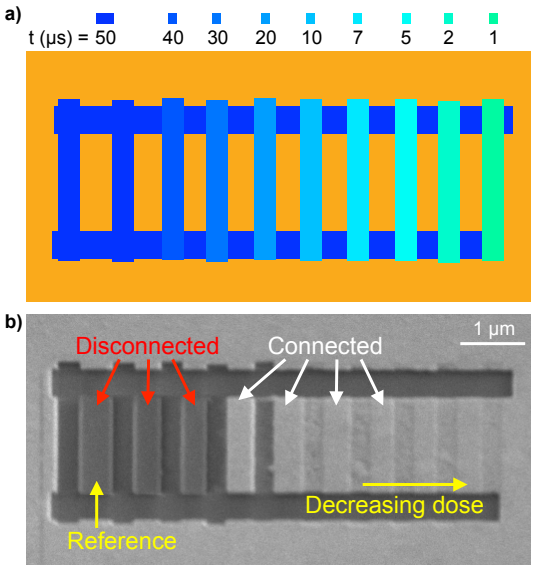

Figure 4.8: **Parameter optimization.** **(a)** Pattern for dwell time optimization, two horizontal stripes with vertical stripes on top. The two horizontal stripes and the first two vertical stripes on the left are milled with the same parameters, for the rest, only the dwell time (and thus, the dose) is changed, which decreases rightwards. **(b)** SEM image of the milled pattern on gold over a CaF_2 substrate showing a clear contrast between the connected and disconnected rectangles.

critical. Then the parameters for the lower beam currents are optimized in decreasing order, which usually require more optimization. One of the ways to optimize the dwell time (or the pitch) is to mill multiple copies of a polygon with a different dwell time (or pitch) while keeping the rest of the milling parameters constant. We usually start with the dwell time and we use a pitch value that gives an overlap value of 50-60% for a given current. Then, we draw a simple pattern in the software of the microscope itself without using NanoBuilder. As it is shown in Fig. 4.8 this pattern consist on two long stripes and multiple vertical stripes where we vary the parameter to be optimized: First of all we pattern the long horizontal stripes and the first two vertical stripes on the left (see Fig. 4.8a), using the same parameters for all four of the stripes. We have to make sure that the rectangle that is left when milling these four stripes is completely disconnected from the rest of the grounded gold film because we use it as a reference. As it can be seen in Fig. 4.8b, when we image a disconnected gold rectangles we have a strong contrast compared with the connected ones, which makes it easy to verify that our reference rectangle is disconnected. Then we add more vertical stripes and we vary one of the parameters to be optimized from one stripe to the other and decreasing the dose rightwards. It is important to decrease the dose rightwards when the reference is on

the left to avoid that one stripe hides the effect (disconnect or not) of the previous one, as once we mill completely trough the gold film with a vertical stripe, all the rectangles on its left get disconnected.

In Fig. 4.8 we vary the dwell time and we can observe some rectangles are disconnected because they show the same contrast as the reference one, while others are clearly connected. From this example, we can conclude that the best dwell time for the current parameters (beam, current, passes, etc) is between 30 and 20 μs. In order to find the best dwell time with more precision, we only need to modify the dwell times on the vertical stripes starting on the third one on the left (so that we keep the reference rectangle unmodified) in smaller steps between 30 and 20 μs and always in decreasing dose rightwards e.g. 30, 28, 26, 24, 22, 20, 18 and 16 μs. We note that in the case of a conducting substrate we could not conclude so easily whether we are milling trough or not.

Usually the pitch also needs to be modified, especially when we observe that there are some unmilled grains of gold in between the rectangles although they are disconnected. We can use the same pattern in Fig. 4.8 but varying the pitch with a given dwell time. If the best result is obtained with a different pitch value to the one used before in the optimization of the dwell time, we repeat the previous optimization with the new pitch value.

This approach allows for the optimization of each parameter in two or three steps and we do not need to fabricate the actual structure with all the parameter variations to see which one is the best combination. Once we get the optimal values for each current we use we can include them in the NanoBuilder job (on the design of the milling process) so that they are saved there. If for some reason the parameters need to be slightly modified we can do it directly with NanoBuilder.

4.3.5 Correlation alignment

Once these optimal milling parameters for every milling current are included in the design of the milling process, the first prototypes can be fabricated. However, first we need to correct the spatial shift among the beams with different currents. This shift is corrected by correlating the different currents among each other, which in NanoBuilder is done with a function called *correlation alignment* and it works as follows: First, only the first layer of the pattern is executed, which in Fig. 4.9a leads to mill the area

corresponding to the blue polygon with a current of 500 pA. The first layer mills away more material, uses the highest current to open a big window around the structure and it also contains the correlation feature. Then, on the next layer which employs a different current (layer 2 in Fig. 4.9a) the correlation alignment option is selected. In this correlation alignment, an image is acquired using ions with the same current used in layer 1 (500 pA) but with much lower dose[13]. This image shows what was fabricated when layer 1 was executed and is acquired only when setting the correlation alignment, never during the fabrication process. The image is stored in the NanoBuilder job in the layer to be correlated, so a new image needs to be acquired for each layer with correlation alignment (layers 2, 3 and 4 in Fig. 4.9a). A search window (where the acquired image becomes visible) needs to be set in each correlation alignment, so that it only includes the correlation feature and its close proximity[14], as it is shown in Fig. 4.10b. In this way, during the fabrication, an image is acquired only on the search window with the current of that particular layer (100 pA for Layer 2 in Fig. 4.9a) and is then correlated with the previously stored image. We note that The cross used as the correlation feature in Fig. 4.9 is less appropriate[15] than its inverse structure, a milled cross (see Fig. 4.10b).

In Fig. 4.10a we show a screenshot of the NanoBuilder program where the pattern of two TLs with their respective control structures (TLs without antennas) is loaded. The first layer is colored dark blue and the correlation feature is the cross on the bottom left corner. Fig. 4.10b shows the search window selected in this design where the stored image becomes visible and is superposed to the pattern.

4.3.6 Fabrication of prototypes

When the first complete prototype is fabricated we verify it by imaging it with the electron beam. Usually the prototypes are not perfect on the first try and we need to slightly modify some milling parameters in order to improve the quality of the prototype. This means that we do multiple fabrication - verification cycles, which are extremely

[13] Otherwise the correlation feature is also milled while imaging

[14] Setting the search window so that it only includes the correlation feature and its close proximity (see Fig. 4.10b), we avoid exposing the region close to the structure.

[15] The cross is only useful for simple designs because it could be problematic and it is usually preferable to have its inverse structure (a milled cross, see Fig. 4.10b): Charging of the substrate around the feature in Fig. 4.9b could generate problems to the software recognizing it and in addition, if the feature is imaged multiple times, the feature or the contact between the feature and the grounded gold film might be milled away, preventing the recognition of the feature for correlation alignment.

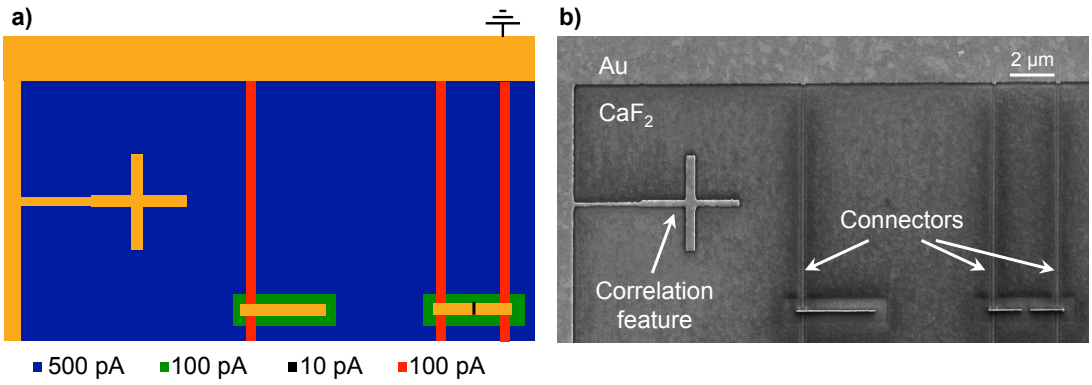

Figure 4.9: **FIB fabrication of single and gap-antennas of gold on CaF_2 substrate.** **(a)** Pattern (blue and green polygons and black line) to expose with FIB over a gold film (yellow) using three beam currents in the following order: 500 pA (blue polygon contained in layer 1), 100 pA (green polygons contained in layer 2), 10 pA (black line polygon contained in layer 3) and 100 pA (red polygons contained in layer 4). The cross on the left hand side is the cross-correlation feature. **(b)** SEM image of single and gap gold antennas on CaF_2 substrate. The footprint of the connectors is clearly visible.

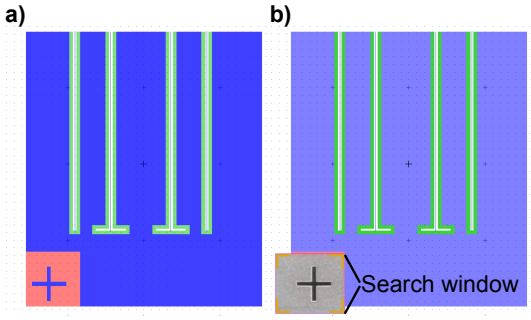

Figure 4.10: **Full design of two TLs and their control structures in NanoBuilder.** **(a)** The design showing all the polygons when the first layer (dark blue) is selected. The red polygon is used to mill away the correlation feature to prevent possible resonances (and thus, radiation) on (from) the feature, this is always the last fabrication step. **(b)** The search window including the correlation feature and its close proximity when a layer that is cross correlated is selected.

time consuming if the complete prototype is fabricated every time. In order to save time while fabricating our prototypes, we can select fabricating only specific parts of our prototypes[16] which allows to fabricate faster and check the quality of the specific parts of the prototype, e.g. we can fabricate only the structure without opening a window around it like in Fig. 4.11 (see also Fig. 4.12a,b) where we verify the quality of the structure and whether the gap is completely open. We also must take into account that the disconnected structures in the final version appear with poor or no contrast

[16]This can be done by executing only specific layers of the NanoBuilder job or by disabling the polygons that we do not want to mill individually.

so we use a connected version on the prototypes (see Fig.4.12a-c) if we want to see the details of these structures (size, shape, edge sharpness, etc). In case that the structures do not show the desired features we can modify the parameters slightly directly on the NanoBuilder job. However, if the structure is nicely defined, showing the features we want but its size slightly different from the desired size, the best way is to proceed is to modify the size of the structure on the pattern in Layout (on `.gds` format) and then load it again to NanoBuilder (which maintains the parameters we had when the NanoBuilder job was last saved) instead of changing the otherwise nicely optimized parameters. Note that the vertical sizes measured with the electron beam are not the actual ones if the stage is tilted (52° for FIB milling).

Fabricating on insulating substrates is challenging but also has some advantages that can be exploited. One of them is to use sample's charging to optimize our milling parameters as it is shown in Fig. 4.8, where the contrast between connected and disconnected gold rectangles is used to find the optimal dwell time. In the same way, it is particularly useful to verify if the gaps we fabricate are completely open, i.e., without short circuits. As it is mentioned in the introduction to this Chapter, the main reason why we started using FIB milling was to produce TLs with high aspect ratio gaps, which need to be opened in order to receive and transport light. A way to verify this is to ground one of the TL arms but not the other one, so that if the gap is completely open one arm of the TL should be dark. In Fig. 4.11 we show an example of open and short circuited gaps on double tapered TLs, where it can be clearly distinguished whether the gaps separating the two arms of the TLs are disconnected or not.

This possibility to verify our structures during the fabrication is really useful as otherwise we would need to measure the structures in our Transmission-mode s-SNOM to check their functionality. This would lead to more fabrication sessions in case of having negative results.

4.3.7 Fabrication of final structures

Finally, when the prototypes that we have been fabricating on a corner of our samples are good enough, we move to a clean place where we fabricate the final structures. Before fabricating, we must focus again all the currents we need as we did in the beginning, to verify we have a well focused beam. Then, we fabricate our final structures.

In case we want to fabricate multiple structures corresponding to different patterns

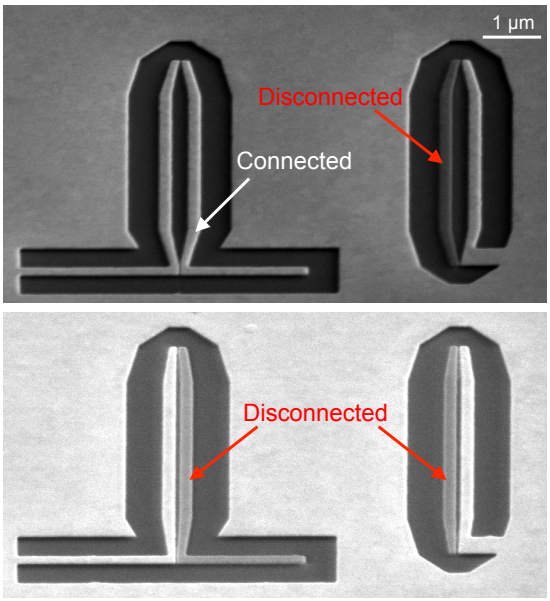

Figure 4.11: **Fabrication verification on double tapered TLs.** SEM images showing two examples of double tapered TLs (left) and their respective control structures (right) fabricated on gold over a CaF_2 substrate, where only the layer circumscribing the structure has been executed and one of the arm of each structure is grounded but not the other.

in the same fabrication session, the best approach is to optimize all the designs first, save the NanoBuilder jobs with the optimal parameters and finally fabricate all of them. In order to optimize the parameters for a new design, the best starting point is to use a previously optimized process with similar characteristics. As it has been stated before, the NanoBuilder jobs keep the last saved parameters for each layer even when a new pattern is loaded. In this way, we open a NanoBuilder job, we load our new pattern with the layers ordered in the same way, then we save it with a new name not to destroy the previous information and only some fine tuning is needed to obtain a good result.

4.4 Examples

Using the fabrication strategy described in previous sections, we have fabricated multiple samples such as alignment samples consisting of simple antenna arrays or more complicated spiral antennas. In Fig. 4.12 we show SEM images of some of the fabricated structures. The images where the structures appear connected (Figs. 4.12a-c) were taken during fabrication in order to verify the dimension of the structures and the fabrication quality. Once the structures are disconnected they appear dark and

with darker stripes on their sides because of charging (see the shadow-like stripes that appear close to the structures in Figs. 4.12d,e,g and 4.12j). This effect increases with the acquisition time (dwell time) we use as can be seen clearly by comparing Fig. 4.12d with Figs. 4.12e,g, where we have used high and low dwell time respectively.

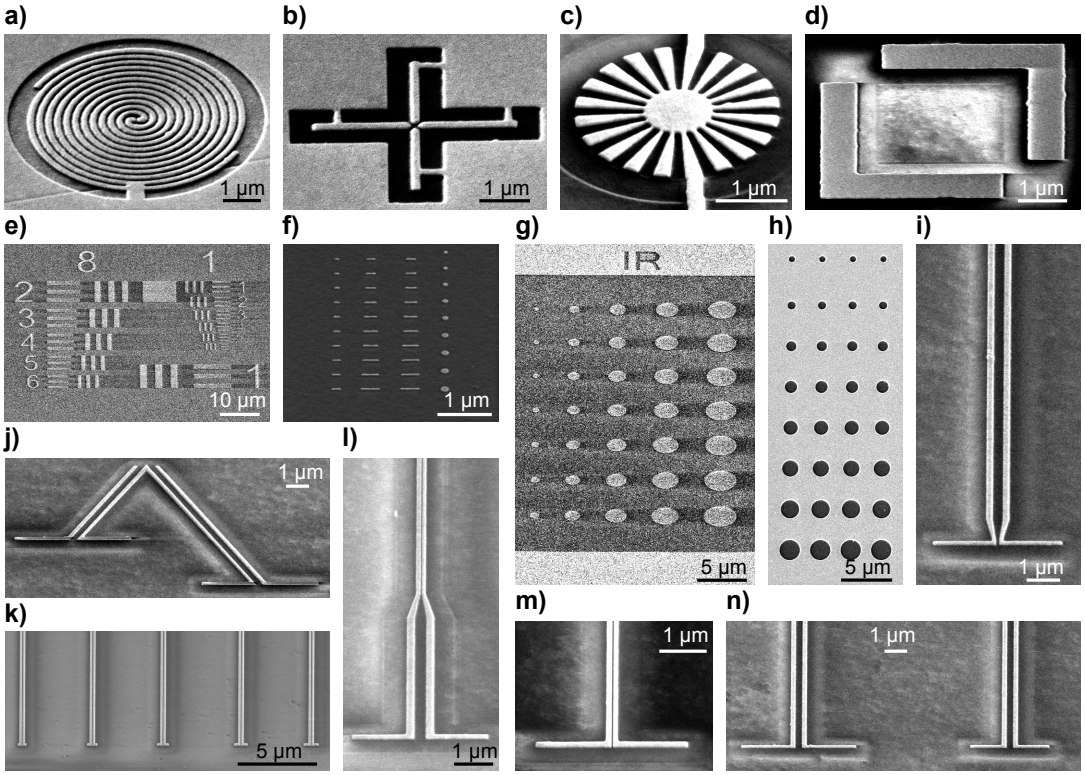

Figure 4.12: **SEM images of multiple examples of structures fabricated by FIB.** The structures are fabricated on CaF_2 substrates except **(f)** and **(h)** and all the images but **(h)** are taken with the stage tilted by 52°. **(a)** Spiral antenna [114], **(b)** cross with a gap in the center and **(c)** antenna for spoof plasmons [136] during the fabrication process still connected to the grounded gold film. **(d)** Isolated unit cell of gold mirror-image L patterns [110]. **(e)** Micrometric 1951 USAF resolution test chart used as resolution test pattern. **(f)** Silver antennas fabricated on epitaxially grown silver film over Si(111) substrate [137]. **(g)** Variously sized gold discs for s-SNOM alignment at infrared frequencies. **(h)** Variously sized circular holes on a gold mask beneath the "Quantum Metamaterial" superlens [138]. Two wire TLs **(i)** with a tapered feed, **(j)** assembled in a phase-matching arrangement, **(k)** with different antenna sizes designed for telecom wavelength, **(l)** tapered for compression of the propagating mode, **(m)** with a gap width of 25 nm and **(n)** coupled to two antenna sized for infrared wavelength.

The structures in Figs. 4.12e-h were fabricated with a single milling step process for different reasons: In Fig. 4.12e the sharpness of the edges is not very relevant, in Figs. 4.12f,g the structures and the window around is small enough to permit a sufficiently low current for good resolution-time compromise and in Figs. 4.12h we fabricate holes. However, for the TLs in Figs. 4.12i-n we need to use a two- or three-milling step process

strategy described previously due to the combination of milling a big window around the structure and maintaining the sharp structural features of the TL.

With some samples a single milling step process is enough (Figs. 4.12e-h), because the sharpness of the features is not very relevant (Fig.4.12e), because the structure and the window around is small enough to permit a sufficiently low current for good resolution-time compromise (Figs. 4.12f,g), or simply because we are fabricating holes (Figs. 4.12h). However, most of the time we need to use a multi-step milling process strategy as described above, especially for structures like TLs with high aspect ratio gaps (Figs. 4.12i-n), due to the combination of milling a big window around the structure and maintaining the sharp structural features of the TL.

4.5 Conclusions

We have shown that the fast prototyping offered by FIB milling can lead to TLs with high aspect ratio gaps, which we could not obtain by e-beam lithography. We have also shown that using insulating substrate can also be a benefit to the researcher if we use the charging of the sample to optimize our milling parameters. In the following chapters we show that the structures fabricated by FIB are functional and thus FIB milling is a very useful technique for fabricating plasmonic structures. In particular for our Transmission-mode s-SNOM measurements it is really convenient to fabricate by FIB milling. The window we mill around the sample works as a small collimator, which prevents a large part of the illuminating beam to pass to the upper part of the sample. This is also particularly useful for far-field techniques like Fourier transforms infrared spectroscopy (FTIR) where the acquisition area is nicely defined by the milled window.

Chapter 5

Near-field Characterization of Nanoscale Infrared Modes in Transmission Lines

In this chapter we demonstrate that functional infrared transmission lines (TLs) with gap widths of 25 and 5 nm can be fabricated by Gallium and Helium ion beam milling of gold films thermally evaporated on insulating substrates. Interferometric and polarization-resolved scattering-type scanning near-field microscopy (s-SNOM) at λ_0= 9.3 μm is applied to image in real space the propagation and confinement of the TL modes. Mapping the p-polarized scattered field, we obtain the distribution of the out-of-plane near-field component of the mode. When s-polarized scattered field is detected, we map the strongly confined in-plane fields propagating inside the gap. With decreasing gap width, we experimentally confirm the predicted reduction of mode diameter D_m, wavelength λ_m and propagation length L_m. For TLs with 25 nm gap width we experimentally verify λ_m= 5 μm mode wavelength and D_m = 42 nm mode diameter ($\lambda_0/220$). The propagation length is about L_m = 8.3 μm, which is more than two orders of magnitude larger than the mode diameter, L_m/D_m = 200. For the TLs with 5 nm gap we find a mode wavelength of λ_m= 3.6 μm, propagation length of L_m = 3.9 μm and mode diameter of D_m = 30 nm. Infrared TLs are thus interesting candidates for the development of ultra-compact infrared circuits or bio-chemical waveguide sensors or circuits.

5.1 TL fabrication by Ga and He ion beam milling

The TLs studied in this chapter (Fig. 5.1) consist of two parallel gold wires separated by an air gap of different widths g, ranging from 500 nm to 5 nm. At the end of each TL an antenna was attached for coupling far-field illumination into an antisymmetric TL mode [31, 32]. CaF_2 was chosen as the supporting substrate because of its low refractive index, which increases the propagation length L_m of the TL mode compared to Si subtrates [111] (see Chapter 3). The TLs were fabricated by ion beam milling of a 40 nm thick thermally evaporated gold layer.

Employing a Gallium ion beam (FEI Helios DualBeam NanoLab 600, FIB model Sidewinder) and a three-step milling process using different ion beam currents (Fig. 5.1a), we fabricated TLs with gaps down to 25 nm (see Chapter 4 for details). We first fabricated the TL contour by clearing a large area of gold with an ion beam current of 500 pA (blue area), followed by more precise milling of the contour edges at a lower current of 100 pA (green area). We then performed a single-pass line-scan along the center of the TL contour at a current of 10 pA (red area) to open the gap and to produce the final TL structure (Fig. 5.1b). Note that during the milling process the TL contour and the final TL were electrically connected to the grounded Au film, in order to avoid charging of the sample and subsequent beam deflection during the milling process, a common challenge with insulating substrates such as CaF_2. Characterizing the fabricated TLs with SEM reveals a homogeneous gap along a total length of 26 μm (Figs. 5.1b-d), which in case of the 25 nm gap (Figs. 5.1c,d) corresponds to an aspect ratio of $>10^3$:1. Large aspect ratio gaps in combination with fast prototyping [139] are primary examples where FIB milling offers a significant advantage over e-beam fabrication processes [127, 128].

To fabricate samples with narrower gaps, Helium ion milling (HIM) was utilized, which has been already successfully employed for structuring silicon nitride[140], graphene [141, 142] and magnetic spin valves [143]. Recently, its capability to fabricate sub-10 nm features in plasmonic structures has been demonstrated [144, 145]. In this chapter, HIM was applied to mill TL gaps with gap width below 10 nm. The helium ion milling was done with a Orion Nanofab in the Carl Zeiss Orion laboratories in Peabody (USA). First, the TL contour was fabricated with a Gallium ion beam as described before. Subsequently, the gap was opened by a single-pass line scan with the Helium ion beam (red area in Fig. 5.1a). We then returned the TLs to the Helios NanoLab 600

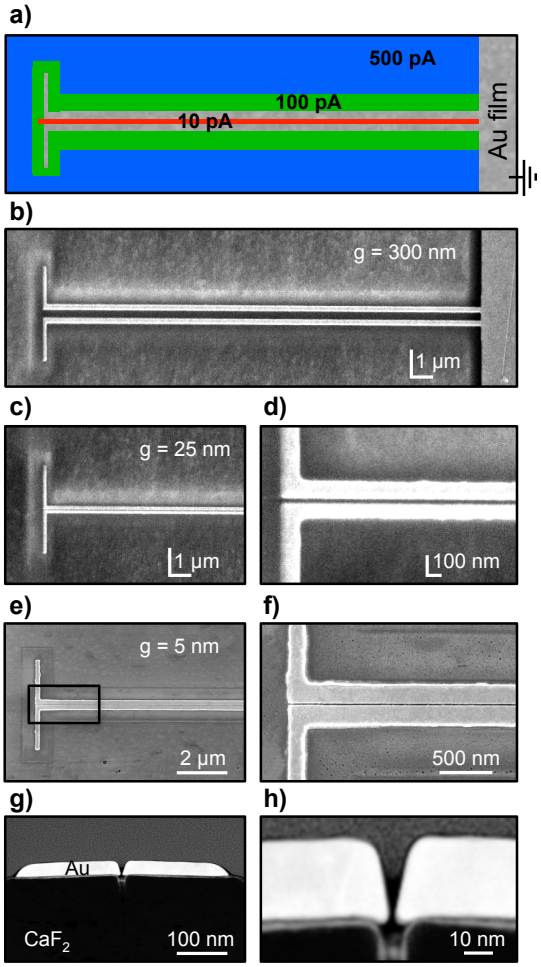

Figure 5.1: **Sample Fabrication by Ga and He ion beam milling.** **(a)** Illustration of the three step milling process. **(b)** SEM image (52° tilt) of a two-wire TL with a 300 nm wide gap with a linear antenna attached to the left end and the grounded gold layer to the right. **(c)** SEM image (52° tilt) of a TL with a 25 nm wide gap. **(d)** Zoom-in image of the TL shown in **(c)**. **(e)** SEM image of a TL with a 5 nm wide gap. **(f)** Zoom-in image of the TL shown in **(e)**. **(g)** STEM image of z cross-section of TL shown in **(e)**, which was fabricated posterior to near-field studies. **(h)** Zoom-in image of the cross section shown in **(g)**.

DualBeam for non-destructive high-resolution imaging of the gap with SEM. In Figs. 5.1e,f the gap is seen as a thin black line in the center of the TL. To measure precisely the gap width, we prepared a cross section (lamella) of the TL by FIB posterior to the near-field microscopy studies and performed scanning transmission electron microscopy (STEM). The STEM image of the cross section (Figs. 5.1g,h) shows a wedge-shaped gap, measuring about 5 nm at the bottom of the Au film. The wedge-like shape we attribute to the ion-beam milling process. We expect more rectangular shaped gaps for thinner gold films.

5.2 Near-field characterization by polarization-resolved interferometric s-SNOM

In order to verify the IR mode propagation and field confinement in the TLs, we applied polarization-resolved transmission-mode scattering-type Scanning Near-Field Optical Microscopy (s-SNOM) [97, 99, 123] (see Chapter 2). The home-built s-SNOM used in this work is based on an Atomic Force Microscope (AFM), where commercial silicon tips (NanoWorld, Arrow-NRC-50) are employed to scatter the near fields of the TLs. The sample is illuminated from below with a weakly focused CO_2 laser beam at a wavelength of $\lambda_0 = 9.3$ μm (Figure 5.2). The polarization was chosen parallel to the dipole antenna to achieve excitation of the anti-symmetric TL mode. The scattered light is collected with a parabolic mirror, analyzed with the linear polarizer P2 to select either the p- or s-component, and detected interferometrically. Background contributions are fully suppressed by vertical tip oscillation with a tapping amplitude about 100 nm at a frequency $\Omega = 300$ kHz (tapping-mode AFM) and subsequent higher harmonic demodulation of the detector signal at 3Ω. The tip-sample distance varies in this case between 0 and 200 nm. Applying a pseudoheterodyne detection scheme [92] yields amplitude and phase of the p- or s-component of the tip-scattered light, ($|E_p|$, φ_p) and ($|E_s|$, φ_s), respectively, depending on the orientation of the polarizer P2. We note that for imaging the sample is scanned (see Chapter 2 for details).

For interpretation of the experimental near-field images, we compare them with numerical calculations of the near-field distribution of the TLs using a commercial FDTD software package (FDTD solutions, www.lumerical.com). In all figures we show either the in-plane (y) or out-of-plane (z) component of the calculated near-field distribution in a height of 15 nm above the TL surface. The height of 15 nm was chosen because the best agreement between experimental and calculated images was obtained (which can be well seen in Figs. 5.5d and 5.6f). We attribute this finding to the finite apex radius of the Si tip (nominally around 10 nm) and the oscillating tip-sample distance.

We first mapped the TL with 25 nm gap width (SEM images in Figs. 5.1c,d) by recording the p-polarized scattered light. Previous publications have shown that such a detection scheme yields images of the vertical (z) near-field component of antennas and TLs [78, 86, 99, 146]. Fig. 5.3a shows maps of the real part of the p-polarized scattered field, $\mathrm{Re}(E_p) = |E_p| \cos \varphi_p$. At the antenna ends we observe enhanced fields

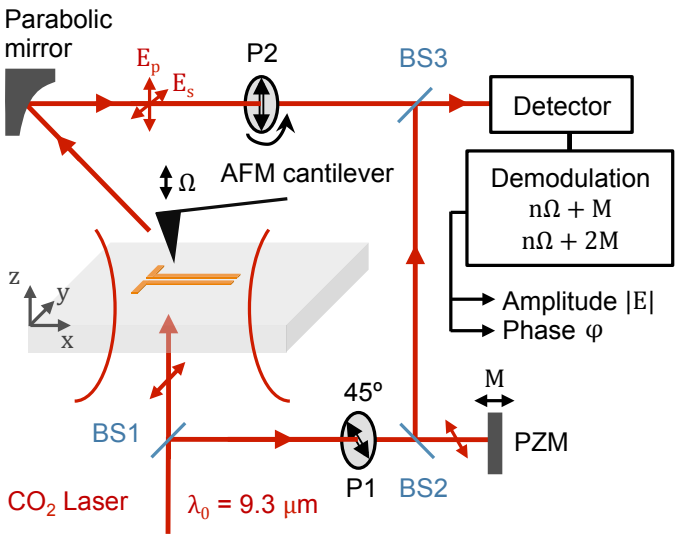

Figure 5.2: **Transmission-mode s-SNOM set-up.** The sample is illuminated from below under normal incidence with a weakly focused infrared laser beam. The polarization is parallel to the antenna that is attached to the TL. The near fields at the sample surface (i.e. TL) are scattered by an AFM silicon tip and detected with a pseudoheretodyne interferometer, yielding infrared near-field amplitude and phase images by scanning the sample. The components are: beam splitters BS1, BS2, BS3; Polarizers 1 and 2; Piezo-actuated mirror PZM, driven at frequency M; Polarizers P1 and P2; AFM operated in tapping mode with a tapping frequency Ω.

[32], oscillating out of phase for about 180 degree. The fields extend along the TL wires, periodically changing their polarity and with opposite sign between the wires, providing clear evidence of a propagating, anti-symmetric mode. With increasing distance x from the antenna, the propagating field decays because of dissipation in the metallic wires comprising the TLs [31, 32, 111]. From the oscillation period of the near-field patterns we can directly determine the effective wavelength of the TL mode, λ_m (marked by the arrow in Fig. 5.3a). The near-field image is in excellent agreement with a numerical calculation of the real part of the vertical near-field component, Re(E_z) (Fig. 5.3b), corroborating that the mapping of the p-polarized scattered light yields directly the near-field distribution of the propagating TL mode. In both experiment and calculation we find a mode wavelength of $\lambda_m = 5.1$ μm.

The near-field image contrast and underlying scattering mechanism for the p-polarized scattered field are illustrated in Fig. 5.3c. The plane wave illumination with field E_0 excites the antenna, which subsequently launches a mode on the TL. The vertical near-field component of the TL mode induces a vertical dipole oscillation in the probing tip, resulting in scattering of a p-polarized field. Because the sample is

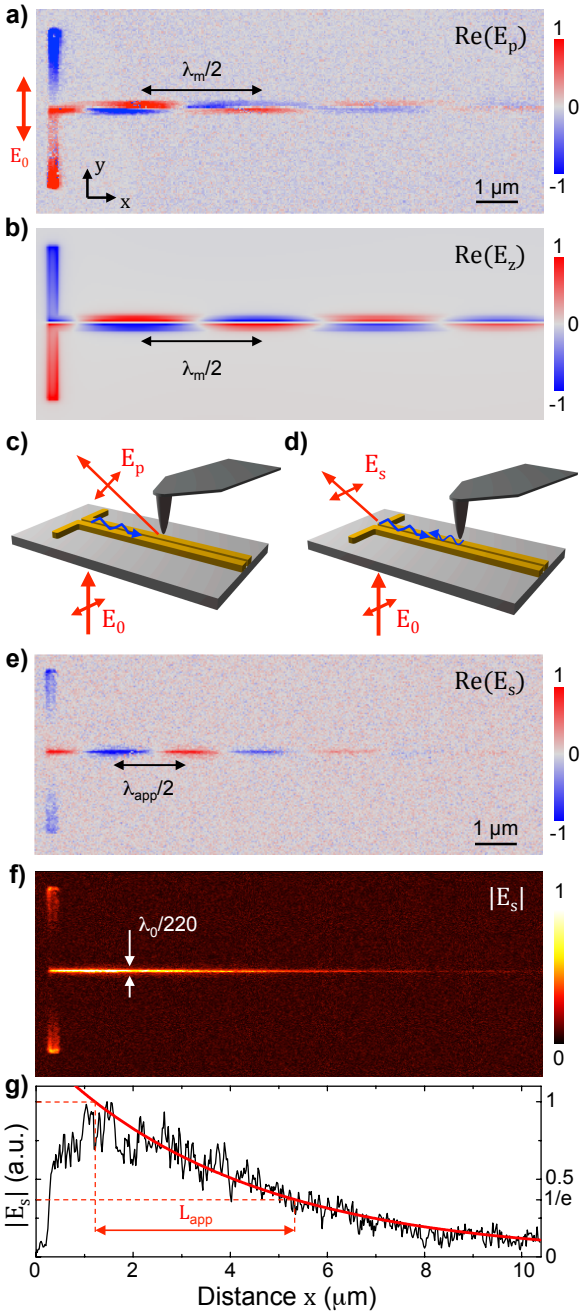

Figure 5.3: **Near-field characterization of a TL with a 25 nm wide gap.** **(a)** Experimental near-field image showing the real part of the p-polarized scattered field, Re(E_p). **(b)** Numerically calculated real part of the vertical near-field component, Re(E_z), 15 nm above the TL. **(c,d)** Schematics of the dominating scattering processes when p- and s-polarized scattered fields are detected. **(e)** Experimental near-field images showing the real part of the s-polarized scattered field, Re(E_s). **(f)** Experimental amplitude of the s-polarized scattered field $|E_s|$. **(g)** Near-field amplitude $|E_s|$ along the center of the TL gap, extracted from the image shown in **(f)**. The red line shows an exponential fit, from which the apparent propagation length, L_{app}, is obtained.

illuminated under normal incidence and the probing tip is stationary, the phase shift of the p-polarized scattered field corresponds to the propagation phase of the TL mode. Thus, the half of the TL mode wavelength is simply given by the distance between two adjacent field maxima (indicated by $\lambda_m/2$ in Figs. 5.3a).

We next imaged the TL with the 25 nm gap by recording the s-polarized scattered field while the TL was illuminated from below. We have previously employed this detection scheme to map the intense and strongly confined near fields ("hot spots") in antenna gaps [99] and at the apex of a tapered TL [32]. It has been shown that the near-field signal inside the gap reveals the in-plane near-field component. Here we apply this detection scheme for mapping the propagating infrared mode on two-wire TLs. In Fig. 5.3e we show the real part of the s-polarized scattered field, ($\mathrm{Re}(E_s) = |E_s| \cos \varphi_s$). We observe strong near-field signals of the same polarity at both antenna extremities, similar to former results obtained on individual infrared antennas [**?**]. We also see a strongly confined near-field signal along the gap between the two TL wires. The polarity of this signal oscillates along the gap, indicating that we probe the concentrated near field propagating inside the gap. Surprisingly, the apparent spatial oscillation period (marked λ_{app} in Fig. 5.3e) is significantly shorter than λ_m in Fig. 5.3a. This observation lets us conclude that the contrast of s-polarized near-field images is based on a different scattering mechanism. Before discussing this finding in more detail, we note that the fields decay with propagation distance, which can be better appreciated in Fig. 5.3f, where we display the absolute value of the electric field, $|E_s|$. The field decay along the gap can be fitted by an exponential function (Fig. 5.3g), yielding an apparent propagation length of about $L_{app} = 4.15$ μm.

We explain the image contrast in Fig. 5.3e as follows. When the s-component of the scattered light is recorded, we mainly detect the s-polarized electric field scattered by the antenna attached to the TL. Because of the antenna resonance, we can assume that the s-polarized field scattered by the antenna is much stronger than the s-polarized field scattered by the dielectric tip (illustrated by the schematics in Fig. 5.3d). We also assume that the tip causes a partial backreflection of the TL mode, when the apex is close or inside the gap, where most of the infrared energy is expected to propagate [32]. Because of the tip vibration at frequency Ω and the non-linear decay of the electric fields vertical to the TL, the mode reflection is modulated at harmonics of the tip vibration frequency, $n\Omega$. The reflected mode propagates back to the antenna where it is reradiated. Recording the s-polarized scattered field by higher-order signal demodula-

tion and pseudoheterodyne interferometric detection subsequently yields amplitude and phase maps providing information about the reflected and antenna-scattered TL mode. The amplitude signal is a measure for the strength of the mode reflection at the tip, while the phase yields the propagation phase of the TL mode. The near-field maps thus exhibit significant differences compared to near-field maps displaying the p-polarized scattered field. First, the infrared TL mode propagates twice the distance between tip and antenna before it is detected. Second, the antenna, and thus scattering center, moves relative to the detector, which introduces a phase shift to the scattered field that depends on the sample position. For both reasons, the distance between signal maxima of the same polarity yields an apparent wavelength, λ_{app}, rather than the wavelength λ_m of the TL mode.

We note that the backreflected TL mode does not influence the near-field images obtained for p-polarized light. First, the near-field images (particularly the mode wavelengths) match well the calculated distribution of the vertical near-field component. Second, the tip reflects the TL mode as a whole (and not a particular field component), which excites the antenna. The associated antenna radiation is s-polarized, owing to the horizontal orientation of the antenna perpendicular to the detection direction. Thus, the antenna radiation is not detected when the p-polarized scattered field is detected.

To corroborate our explanation and to reconstruct the near-field distribution of the TL from s-polarized near-field images, we developed a model describing the scattered field E_s, which is illustrated in Fig. 5.4. We assume that the antenna launches an exponentially decaying electromagnetic mode on the TL with a mode wavelength λ_m and a propagation length L_m. The mode propagates along the TL with most of the energy confined in the gap (indicated in Fig. 5.4 by the blue arrow on the TL pointing towards the tip). When the tip is located in the gap of the TL, the mode is partially reflected back to the antenna (indicated in Fig. 5.4 by the blue arrow on the TL pointing towards the antenna) where it is radiated. Assuming that the mode has an initial field E_0 (i.e. $E_t(x=0) = E_0$), the field at the tip (located on the TL gap at distance x from the antenna) is then given by

$$E_t(x,y) \propto E_0 e^{i\frac{2\pi}{\lambda_m}x} e^{-\frac{x}{L_m}} \tag{5.1}$$

and the back-reflected field at the antenna by $E_t(2x,y)$. To finally obtain the scattered field, we have to account for the sample (antenna) movement relative to the detector,

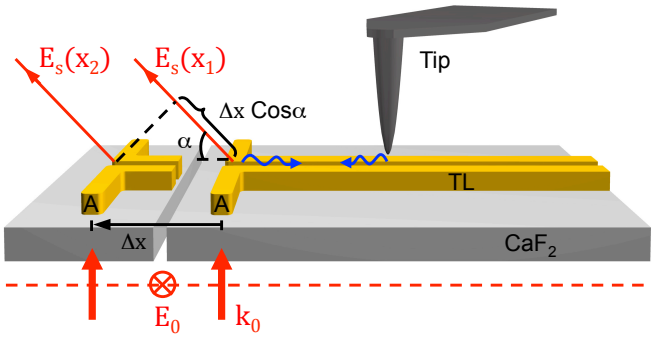

Figure 5.4: **Model of contrast mechanism in case the s-polarized scattered field is recorded.** Δx displays the sample displacement, α is the detection angle.

given by the last exponent in Eq. 5.2:

$$E_s(x,y) = E_t(x,y)e^{i\frac{2\pi}{\lambda_m}x}e^{-\frac{x}{L_m}}e^{-i\frac{2\pi}{\lambda_0}x\cos\alpha} \tag{5.2}$$

λ_0 is the wavelength of the free-space radiation and $\alpha = 30°$ the angle of detection relative to the sample surface. In the near-field map, the scattered field subsequently yields an apparent near-field distribution given by

$$E_{app}(x,y) \propto E_0 e^{i\frac{2\pi}{\lambda_{app}}x}e^{-\frac{x}{L_{app}}} \tag{5.3}$$

Comparing Eqs. 5.2 and 5.3, we obtain the mode wavelength and propagation length:

$$\lambda_m = \frac{2\lambda_0\lambda_{app}}{\lambda_0 + \lambda_{app}\cos\alpha} \tag{5.4}$$

$$L_m = 2L_{app} \tag{5.5}$$

With an apparent wavelength of $\lambda_{app} = 3.1$ μm (Fig. 5.3e), we obtain $\lambda_m = 4.9$ μm, which is in good agreement with the mode wavelength obtained directly from Fig. 5.3a ($\lambda_m = 5.1$ μm) and with numerically calculated results (see Fig. 5.7a and discussion below). For the propagation length we obtain $L_m = 8.3$ μm, which is slightly shorter than the numerically calculated propagation length (see Fig. 5.7b and discussion below).

Having measured both amplitude and phase of the scattered field $E_s(x,y)$, we can reconstruct the near-field distribution of the TL. Using Eq. 5.2, $\lambda_{app} = 3.1$ μm from Fig. 5.3e, and $L_{app} = 4.15$ μm from Fig. 5.3f, we obtain $E_t(x,y)$. The real part of $E_t(x,y)$ is shown in Fig. 5.5b. It matches well with the numerically calculated near-field distribution (real part of $E_y(x,y)$) of the TL shown in Fig. 5.5a. The good agreement can be further appreciated in Fig. 5.5c, which shows the reconstructed (dots) and numerically calculated (red line) field along the TL gap.

In Fig. 5.5d we display the near-field amplitude along the dashed black line in Fig. 5.5b in order to measure the mode diameter D_m. As mode diameter we define the FWHM of the measured near-field profile perpendicular to the TL gap. We find a mode diameter D_m of about 42 nm, which is significantly smaller than the incident wavelength λ_0, $\lambda_0/D_m = 220$, providing direct experimental evidence of nanoscale field confinement that can be achieved with TLs at IR frequencies. For comparison, we show the calculated near-field profile in 15 nm height above the TL, which has been extracted from Fig. 5.5e. As can be seen in Fig. 5.5d, the calculated field profile (black solid line) matches well with the measured near-field profile (symbols).

Comparing propagation length and mode wavelength, we find $L_m/\lambda_m \approx 1.7$, which seems rather short. However, by comparing the propagation length with the mode diameter $D_m = 42$ nm (Fig. 5.5d), we obtain the quite large value $L_m/D_m = 8.3$ μm/42 nm = 200. Remarkably, a mid-IR mode with a diameter below 50 nm can propagate several micrometers. The large difference between the two relative propagation lengths, L_m/λ_m and L_m/D_m, is due to the rather long wavelength of the mode, being two orders of magnitude larger than the mode confinement. We stress that nanoscale field confinement does not require ultra-short mode wavelengths, as we discuss in more detail below.

We also imaged the TL with 5 nm gap width by recording the p- and s-polarized scattered field. The images showing the real part of E_p and E_s are displayed in Figs. 5.6a and b, respectively. As before in Fig. 5.3 with the 25 nm gap TL, we observe an oscillating near-field distribution on the TL. For the s-polarization, the detected (apparent) wavelength is significantly shorter than with the p-polarization due to the different scattering mechanisms, as explained above. The images clearly demonstrate that the He-milled TL with only 5 nm gap width is functional and supports a highly confined infrared mode. In Fig. 5.6a we directly measure $\lambda_m = 3.68$ μm, while in Fig. 5.6b we find $\lambda_{app} = 2.2$ μm, yielding $\lambda_m = 3.6$ μm according to Eq. 5.4. λ_m is thus

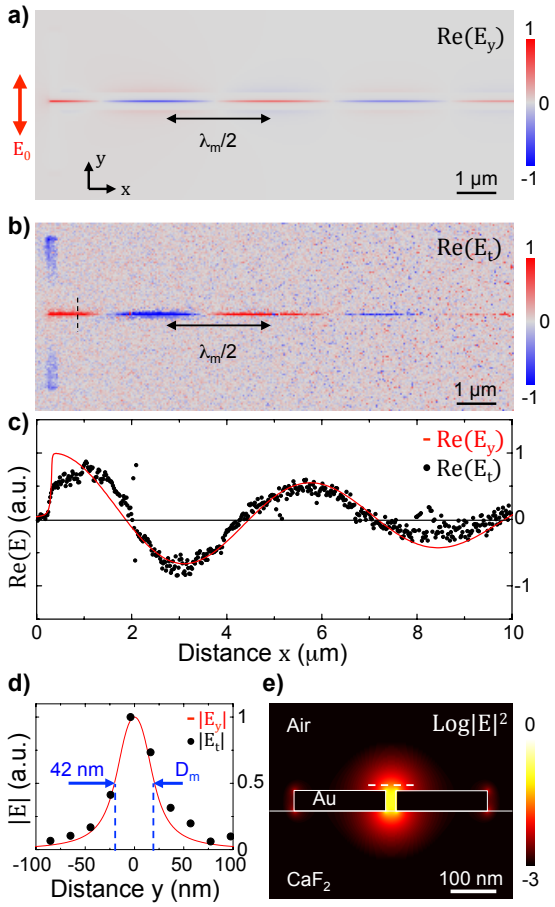

Figure 5.5: **Reconstruction of near-field distribution from the s-polarized scattered field.** **(a)** Numerically calculated near-field distribution showing the real part of the in-plane field component $\mathrm{Re}(E_y)$, 15 nm above the TL. **(b)** Near-field distribution, $\mathrm{Re}(E_t)$, reconstructed from the experimental image in Fig. 3e. **(c)** Real part of the reconstructed near-field distribution, $\mathrm{Re}(E_t)$, along the center of the TL gap, extracted from the image shown in **(b)**. The red line shows the real part of the in plane component, $\mathrm{Re}(E_y)$, calculated 15 nm above the TL gap. **(d)** Calculated amplitude of the in-plane near-field component, $|E_y|$, 15 nm above the TL (red line), and along the dashed line in **(e)**. The black circles represent the experimental near-field amplitude data, $|E_t|$, extracted from **(b)** along the dashed line. **(e)** Numerically calculated mode profile, showing the normalized electric field intensity in logarithmic scale. The dashed line indicated where the line profile shown in **(d)** was extracted.

about 30% shorter than the one measured in Fig. 5.3a for the TL with 25 nm. We discuss this gap-dependent wavelength reduction below in Fig. 5.7a.

We note that the near field in both Figs. 5.6a and 5.6b abruptly vanishes at about 5 μm distance from the antenna. It can be explained by a short circuit in the TL (eventually by incomplete milling of the gap or formation of metal bridge due to re-sputtering of the gold), which becomes evident by displaying the amplitude of the s-polarized scattered field in Fig. 5.6c. We observe modulations of the field amplitude

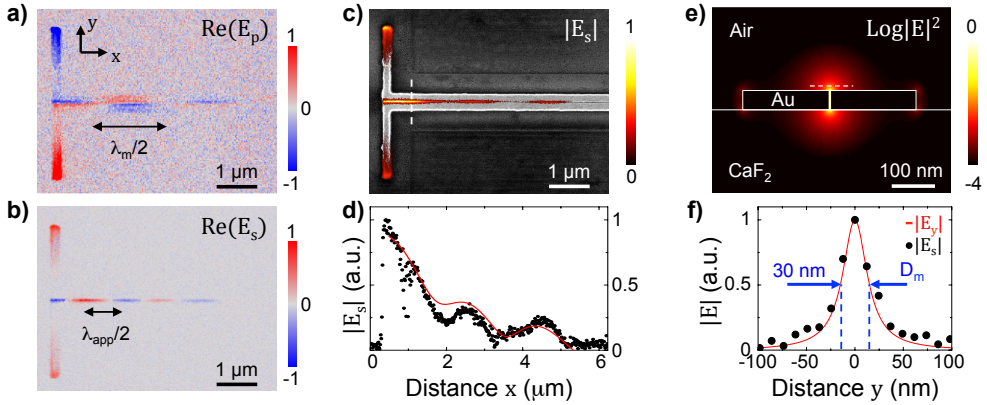

Figure 5.6: **Near-field characterization of a TL with a 5 nm wide gap.** **(a)** Experimental near-field image showing the real part of the p-polarized scattered field, Re(E_p). **(b)** Experimental near-field image showing the real part of the s-polarized scattered field, Re(E_s). **(c)** Experimental near-field amplitude image (in color) of the s-polarized scattered field $|E_s|$, superposed to the SEM image (in grey) of the TL. **(d)** Experimental near-field amplitude (black dots) along the center of the TL gap, extracted from the near-field image shown in **(c)**. The red line represents a fit to the data, assuming an exponentially decaying wave being backreflected at position $x = 5$ μm. **(e)** Numerically calculated mode profile, showing the normalized electric field intensity in logarithmic scale. **(f)** Calculated amplitude of the in-plane near-field component, $|E_y|$, 15 nm above the TL (red line), and along the dashed line in **(e)**. The black circles represent the experimental near-field amplitude data, $|E_s|$, extracted from **(c)** along the dashed white line.

along the gap, rather than a monotonous exponentially decaying field. We explain them as interference between the forward propagating mode and the mode that is back-reflected at the short circuit. In order to obtain the propagation length L_m, we averaged the line scans around the gap in Fig. 5.6c and fitted the result to a damped standing wave (red solid line in Fig. 5.6d). We obtain a propagation length of $L_m = 3.9$ μm, which is slightly smaller than the numerically calculated propagation length $L_{m,calc} = 6.2$ μm (see Fig. 5.7b).

In Fig. 5.6f we display the near-field profile along the dashed white line in Fig. 5.6c. We find a FWHM of about 30 nm, which indicates a mode diameter being about 310 times smaller than the incident wavelength λ_0, respectively 120 times smaller than the mode wavelength, $\lambda_m/D_m = 120$. For comparison, we show the calculated near-field profile in 15 nm height above the TL, which has been extracted from Fig. 5.6e. As can be seen in Fig 5.6f, the calculated field profile (black solid line) matches well with the measured near-field profile (symbols). Comparing the propagation length with the mode diameter $D_m = 30$ nm (Fig. 5.6f), we obtain $L_m/D_m = 3.9$ μm/30 nm = 130, which is slightly smaller than the one obtained for the TL with gap width $g = 25$ nm.

5.3 Study of mode properties as a function of gap width

In Fig. 5.7a we summarize the experimentally found mode wavelength λ_m (symbols) as a function of the gap width g and compare them with results obtained by numerical calculations (red solid line) performed with a mode solver (FDTD solutions, www.lumerical.com). The experimental values for $g = 300$ nm and 500 nm were taken from near-field images not shown, and the ones for $g = 5$ nm and 25 nm were taken from Figs. 5.3a and 5.6a (red triangles) and reconstructed from Figs. 5.3e and 5.6b (red circles). In the calculations we considered infinitely long TLs consisting of two rectangular Au wires (width 200 nm, height 40 nm) separated by a rectangular-shaped gap of width g and supported by a CaF_2 substrate. To describe gold at mid-IR frequencies we used the Drude model, yielding the permittivity

$$\epsilon_{\mathrm{Au}}(\omega) = \epsilon_{inf} - \frac{\omega_p^2}{\omega^2 + i\Gamma\omega} \tag{5.6}$$

with $\omega_p = 8.95$ eV being the plasma frequency, $\Gamma = 65.8$ eV the damping parameter and $\epsilon_{\mathrm{inf}} = 11$ [36]. Employing the dielectric values for $\lambda_0 = 9.3$ μm, we obtain good quantitative agreement between calculated (red solid line) and experimental (symbols) mode wavelengths λ_m. Particularly, the plot corroborates that λ_m decreases with decreasing gap width g, reaching values of about $\lambda_0/5$ for gaps as small as 1 nm.

In order to understand the wavelength reduction of two-wire TL modes at mid-infrared frequencies (that is, far away from the strong plasmonic behaviour of gold), we performed mode simulations where we assumed artificial material properties for the gold. First, we assume that gold is a lossless Drude metal, i.e. we set the damping parameter in the Drude model (Eq. 5.6) to zero, $\Gamma = 0$. The calculated mode wavelengths in this case (blue curve in Fig. 5.7a) are nearly identical the mode wavelengths obtained by using a realistic Drude model for gold (red curve in Fig. 5.7a). This finding indicates that the absorption in the gold is not the cause for the mode wavelength reduction. By substituting Au by a Perfect Electric Conductor (PEC) in the calculations, the mode wavelength λ_m does not decrease but slightly increases with decreasing gap width, approaching λ_0 for $g < 100$ nm (green curve in Fig. 5.7a). This is because for a PEC material no field is propagating inside the wires. The fields propagate in the air and the substrate below the TL. When the gap width is reduced, the field concentrates inside the air gap and thus a smaller part of the mode propagates in the substrate.

For that reason, the mode wavelength λ_m increases for smaller gaps, approaching the mode wavelength λ_0 of a PEC without substrate (black curve in Fig. 5.7a). Note that for a PEC TL without substrate all field energy propagates in air, and thus the mode wavelength λ_m equals λ_0 for all gap widths. From the sum of all these numerical results we conclude that in a realistic gold TL the mode wavelength λ_m decreases because of an increasing amount of field energy propagating inside the gold when the gap width decreases, owing to the finite real part of the dielectric function. This effect has been already described analytically for nanoscale plasmon cavities [147].

It is worth to be noted that the mode wavelength λ_m for sub-10 nm gaps is still in the micrometer range, showing that nanoscale field confinement in infrared TLs (as observed in Figs. 5.5e and 5.6d) does not require wavelength compression to the nanometer scale. The mechanism of field confinement in the TLs is rather of geometrical nature. The two metal wires (Au or PEC) are the mode carriers, and the field confinement is achieved by capacitive coupling between the TL wires [19].

We also calculated the mode propagation length L_m as a function of gap width g. The results are shown in Fig. 5.7b together with the experimental values for g = 25 nm and g = 5 nm obtained from the fittings shown in Figs. 5.3g and 5.6d. The experimental values are in good agreement with the calculated ones, although the experimental propagation lengths are slightly smaller. These discrepancies might be explained by imperfections in the fabrication process, such as ion implantation and ion beam damage of gold and substrate, or due to non-uniformity of the gap width. We note that the numerical calculation predict significant propagation distances even for TLs with sub-5 nm gaps, for example L_m = 3 μm for g = 1 nm.

5.4 Conclusions

We demonstrated that focused ion beam (FIB) milling can be applied for fabricating functional mid-infrared two-wire TLs on insulating substrates. By applying Ga and He ion beam milling we could fabricate metal TL wires separated by air gaps as small as 5 nm. Employing polarization-resolved interferometric s-SNOM, we could experimentally map the near-field distribution, wavelength and confinement of the mid-infrared modes supported by the TLs. Numerical simulations confirm the experimental results, corroborating that nanoscale mid-infrared mode confinement and micrometer long propagation distances can be achieved with such TLs. The ratio between propagation distance

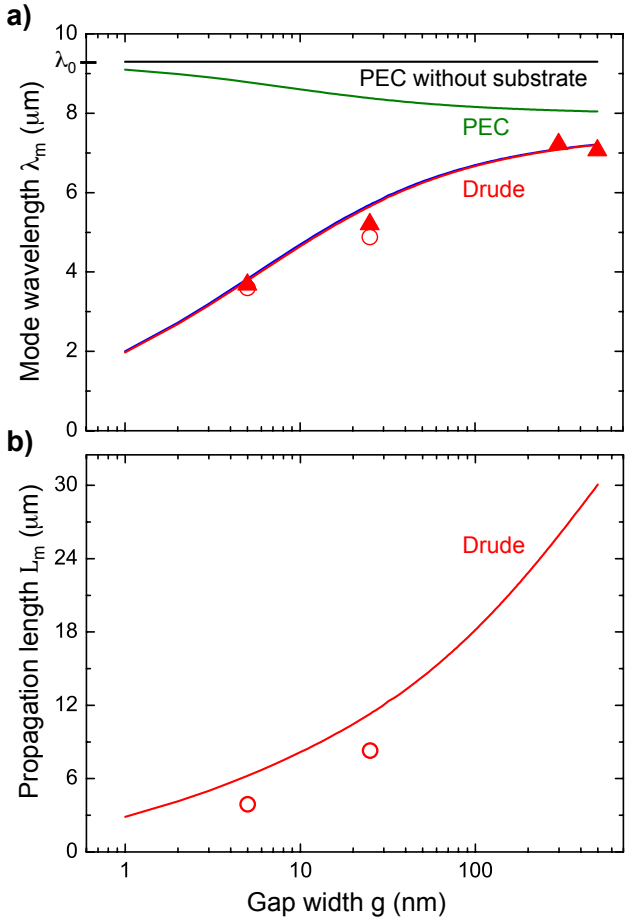

Figure 5.7: **Propagation properties of TL modes. (a)** Calculated effective wavelength of the TL mode as a function of the gap width g. Red line: TL made of Au described by the Drude model. Green line: TL made of PEC. Black line: TL made of PEC and without substrate. The red triangles display the experimental data extracted from Figs. 5.3a and 5.6a and from images (not shown) of vertical near-field distribution of TLs with 300 nm and 500 nm gap width. The red circles display the mode wavelength reconstructed from the data shown in Figs. 5.3e and 5.6b. **(b)** Calculated propagation length of the TL mode as a function of the gap width g, for a TL made of Au described by the Drude model. The red circles display the experimental propagation lengths obtained from the fittings shown in Figs. 5.3g and 5.6d.

and mode confinement is larger than 100, which makes metal two-wire TLs promising structures for guiding and manipulating mid-infrared energy in nanoscale circuits and devices. TLs comprising nanoscale wire separation thus could become highly valuable building blocks in ultra-sensitive and ultra-compact mid-infrared sensing, spectroscopy and nanoimaging applications.

Chapter 6

Real-space Mapping of Near-field Distributions in Spiral Antennas and Planar Metasurfaces

Chiral antennas and metasurfaces can be designed to react differently to left- (LCP) and right-handed circularly polarized (RCP) light, which enables novel optical properties such as giant optical activity and negative refraction. In this chapter, we demonstrate that the underlying chiral near-field distributions can be directly mapped with scattering-type scanning near-field optical microscopy (s-SNOM) employing circularly polarized illumination. We apply our technique to visualize, for the first time, the circular-polarization selective nanofocusing of infrared light in Archimedean spiral antennas, and explain this chiral optical effect by directional launching of travelling waves in analogy to antenna theory. Moreover, we near-field image single-layer rosette and asymmetric dipole-monopole metasurfaces and find negligible and strong chiral optical near-field contrast, respectively, which provides an insight into the microscopic origin of the negligible and strong circular dichroism (CD) in these structures. Our technique paves the way for near-field characterization of optical chirality in metal nanostructures, which will be essential for the future development of chiral antennas and metasurfaces and their applications.

6.1 Introduction

Optical antennas [148] and metamaterials [149, 150] allow for fascinating new ways of manipulating light far beyond the capabilities of classical optical components, which has paved the way to novel photonic applications ranging from ultrasensitive spectroscopy [12, 15] and ultrafast photodetectors [151] to negative refraction [152, 153] and perfect absorption [154]. Recently, a significant research interest was found with chiral metal nanostructures, where the individual elements or their arrangement have the property of handedness [149, 155–170]. They exhibit a different optical response to left (LCP) and right circularly polarized (RCP) light, which can be engineered to be much stronger than that of natural materials such as chiral (bio)molecules. This chiral optical effect can be exploited to produce an extraordinarily large optical activity and CD in chiral metamaterials, which may be used for broadband circular polarizers [161, 166], or to achieve negative refraction based on a chiral resonance [160, 164, 168]. Furthermore, optical chirality can be strongly enhanced in the vicinity of chiral antennas, enabling novel CD spectroscopy applications with greatly improved sensitivity for the molecules' handedness [155, 165, 170, 171].

Interestingly, chirality is also found in radiofrequency antenna design such as with helical and spiral antennas [33, 41, 42], where the chiral antenna geometry provides radiation with circular polarization, thus offering improved radio transmission in situations where the relative orientation of transmitting and receiving antennas is unknown or multipath interferences occur. First studies have demonstrated functional optical and infrared spiral antennas, and have investigated their radiation properties in the far field as well as reception of thermal radiation [172–175]. However, transmission and reception with circular polarization, and particularly the chiral near-field response, are widely unexplored.

So far, experimental characterization of optical chirality is mainly based on far-field spectroscopy [156–167], which however provides only limited information on the underlying microscopic mechanisms. For example, while optical activity and circular dichroism of metal nanostructures can be directly measured in transmission experiments, its root cause, the surface charge and current distributions, cannot be experimentally confirmed. Nanoimaging techniques are thus needed to verify theoretically predicted surface charge distributions and to test real-world structures in the near field. The latter is particularly important for control and optimization of the fabrication

process because the chiral optical response critically depends on absorption losses in the metal structures [176–180], the actual element shape and the quality of interelement alignment [158]. In first studies, the near-field distributions in chiral antennas and metasurfaces were mapped with near-field microscopy employing linearly polarized illumination [181], and also maps of the differential near-field signal for periodically changing LCP and RCP excitation were obtained [182, 183]. However, the near-field distributions in antennas and metasurfaces excited by circularly polarized light, the relevant polarization in dichroism measurements and chiral negative refraction, have not been imaged yet.

In this chapter we demonstrate that the chiral near-field distributions in extended two-dimensional nanostructures can be mapped directly and in real space with transmission-mode s-SNOM [97–99, 123] employing circularly polarized illumination. We apply our technique to provide experimental evidence of the circular-polarization-sensitive nanofocusing capabilities of infrared Archimedean spiral nanoantennas in the near field, as a canonical example of chiral antenna structures. We also investigate how the circular polarization contrast depends on the antenna arm length and explain the findings in terms of standing wave and travelling wave concepts from antenna theory. We furthermore apply our technique to image the chiral near-field distributions of a single-layer rosette metasurface and an asymmetric dipole-monopole metasurfaces [178], and connect the results with the chiral optical response (circular dichroism) in the far field.

6.2 Sample fabrication

The metal nanostructures that we study in the following were fabricated by focused ion beam (FIB) milling of a 60 nm thick thermally evaporated Au layer on a CaF_2 substrate using a three milling step process [98]. As described in Chapter 4, we removed in a first step the metal around the nanostructures with a high current (double pass, 500 pA) and only left a thin metal bridge connecting electrically the structures with the grounded gold film. This avoids charging of the sample and subsequent beam deflection during the following milling steps (see Chapter 4). In a second step, we milled the fine structure, including the gaps, at a lower current of 30 to 100 pA (double pass). In a third step, we removed the metal bridges and to obtain the final structure. We note that the gold wires of the spiral antennas are 200 nm wide and are separated by 200 nm, while in

the topography images in Fig. 6.2 the wires appear wider than the gap. This can be explained as a convolution effect because of the relatively large s-SNOM tip (~ 20 nm in diameter).

6.3 Near-field microscope setup

In order to map the near-field distributions in chiral metal nanostructures, we modified our near-field microscope setup (see Chapter 2). In Fig. 6.1, we introduce and illustrate s-SNOM [97–99, 123] antenna mapping employing circularly polarized light. The sample and tip are illuminated from below at normal incidence with a weakly focused CO_2 laser beam at a wavelength of 9.3 μm with left- (LCP) or right-handed circular polarization (RCP). The light scattered from the tip and the sample is collected with a parabolic mirror in $+x$-direction at an angle of 60° from the surface normal, and superimposed it with a p-polarized phase-modulated reference beam at the infrared detector. Background contributions can be fully suppressed by vertical tip oscillation at a frequency $\Omega = 250$ kHz (tapping-mode AFM) and by subsequent higher harmonic demodulation of the detector signal at 3Ω. Using a pseudoheterodyne detection scheme [92], the amplitude $|E_p|$ and phase φ_p of the p-component of the scattered light are obtained.

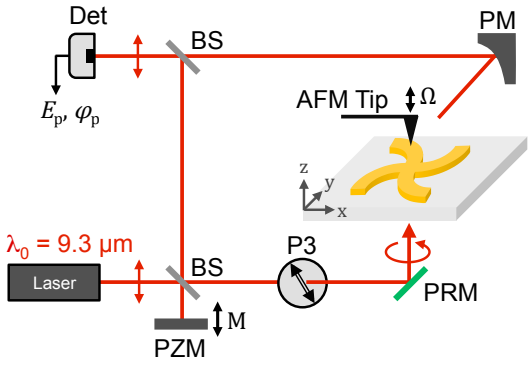

Figure 6.1: **Transmission-mode s-SNOM for near-field mapping with circularly polarized illumination.** Laser: CO_2 laser emitting at 9.3 μm wavelength, BS: beam splitter, PZM: piezo-actuated mirror driven at frequency M, P3: linear polarizer, PRM: Infrared phase retarding mirror, AFM: Atomic force microscope, PM: Parabolic Mirror, Det: Pseudoheterodyne detection.

To generate left (LCP) and right-handed circular polarized (RCP) light we located a polarizer (marked as P3 in Fig. 6.1) and a phase retarding mirror PRM (designed

for 9.3 μm wavelength, Rocky Mountain Instruments) in the probing beam path (see Chapter 2). Switching between LCP and RCP is achieved by rotating the polarizer 45° and −45° respect to the vertical axis z (see Fig. 6.1) respectively. We characterized the PRM by registering the light transmitted through a linear analyzer upon one rotation with an infrared detector. We found that at 9.3 μm wavelength the light reflected on the PRM was slightly elliptically polarized with an axial ratio[1] of 1.17:1 for both RCP and LCP light. We explain this slight ellipticity by the fabrication tolerances of the PMR element, specified by the manufacturer to be $90° \pm 6°$ for the introduced phase shift between the orthogonal components of the circular polarization. Note that here we define LCP and RCP as a wave propagating in $+z$ direction with a counterclockwise and clockwise rotation of the electric field vector in the (x, y) plane (from the point of view of the receiver), respectively.

6.4 Model for reconstructing s-SNOM images

In order to compare the obtained experimental near-field distributions of spiral antennas and metasurfaces (see Figs. 6.2 and 6.2) with numerically calculated near-field distributions, we rely on a recently developed model to reconstruct s-SNOM images [113]. Typically, the experimental near-field images ($|E_p|$, φ_p) have been compared to the z-component of the calculated near-field distribution ($|E_z|$, φ_z). However, a recent study has revealed that the signal obtained in s-SNOM is given by a complex combination of the different local near-field components with both linear and quadratic dependencies [113]. For a dipole antenna, it was shown that the experimental near-field distribution can deviate substantially from the numerical calculated distribution of a single near-field component, an effect which can be expected to be even more pronounced in the case of more complex structures such as the presented chiral antennas and metasurfaces. We thus apply a recently developed model for the scattering process in s-SNOM [113] to calculate the theoretical s-SNOM amplitude and phase images ($|E_p|$, φ_p) of the antenna near-field distribution. The model takes into account multiple scattering events between the probing tip and the antenna, which it describes in a first order approximation by (i) direct scattering of the antenna near fields by the tip into the far field (detector) and (ii) indirect scattering of the antenna near fields by the tip via the antenna itself [113]. The model takes also into account the combination of the different near-field components in

[1] The ratio between the major an minor axis of the ellipse, i.e. the ratio between the maximum and minimum intensities registered upon one rotation of the analyzer.

the s-SNOM signal, depending on the illumination and detection conditions [113]

In order to simulate the experimental s-SNOM images according to the model, we first numerically calculate the electric near-field distributions of the presented metal nanostructures using a commercial finite-difference time-domain (FDTD) software package (FDTD Solutions, Lumerical). We assume a dielectric value for gold of $\epsilon_{Au} = -2598 + 1157i$ according to Palik and for the CaF_2 substrate of $\epsilon_{CaF_2} = 1.74$ for illuminating light with a incident light free-space wavelength of $\lambda_0 = 9.3$ μm. We calculate the electric field at a height of 50 nm above the metal nanostructures, yielding the near-field distribution $E_{inc}(x, y)$, for sample illumination from below at normal incidence with either LCP or RCP. In Figs. 6.2 and 6.2, we plot the z component $E_z(x, y)$ to visualize the near-field distribution in the vicinity of the nanostructures. In order to take into account the detection conditions, i.e. detection of p-polarized scattered light from above at an angle of 60° to the surface normal, we then perform an additional numerical simulation. We assume a p-polarized plane-wave illumination incident on the sample from the same direction as the collection of the scattered light was taking place, i.e. $+x$ direction at an angle of 60° to the surface normal and we calculate the electric field distribution $E_{virt}(x, y)$ at the same height above the metal nanostructures. For each illumination polarization (LCP, RCP), we then calculate the scattered field $E_p(x, y)$ according to

$$E_p(x, y) \propto E_{virt}(x, y) \cdot \alpha^T \cdot E_{inc}(x, y) \tag{6.1}$$

We assumed a diagonal scattering tensor of the tip, α^T, where we choose $\alpha_x^T = \alpha_y^T = \alpha_z^T = 1$ to obtain best agreement with the experimental s-SNOM maps (Figs. 6.2), and $\alpha_x^T = \alpha_y^T = 1$ and $\alpha_z^T = 3$ in Figs. 6.5.

6.5 Near-field mapping of spiral antenna structures

We first apply the transmission-mode s-SNOM to image infrared Archimedean spiral antennas, which are a well-established design concept from RF antenna theory offering large bandwidth, compact dimensions and radiation with circular polarization [33,41,42] (see Chapter 1). Figs. 6.2a,b show the topography images of a 1-turn and a 5-turn infrared Archimedean spiral antenna made of 200 nm wide and 60 nm high gold wires, separated by a 200 nm wide gap and supported on a CaF_2 substrate. The near-field

maps of the 1-turn antenna show similar amplitude and phase response for LCP and RCP, yielding strong fields near the antenna gap and at the arm ends (Fig. 6.2c). Intriguingly, a dramatic difference is observed with the 5-turn antenna (Fig. 6.2d): LCP produces a strong field concentration near the antenna gap and no significant fields are seen on the outer part of the antenna. For RCP illumination, in contrast, the fields completely extinguish at the gap and a ring-shaped field concentration is observed in a distance of 3 to 5 μm from the gap. These observations indicate that the length of the spiral arms decisively determines the near-field optical response to the handedness of circularly polarized light.

Remarkably, the chiral optical response of our spiral antennas operating at infrared frequencies can be explained by a directional launching of travelling waves in analogy to antenna theory [33, 41, 42] (see Chapter 1). We first consider the 5-turn antenna (Fig. 6.2h) that exhibits an arm length of about 75 μm, which is large in terms of the wavelength ($\lambda_0 = 9.3$ μm). This antenna can be described as an infrared two-wire transmission line (TL) [31,32,98] that is wound into a spiral configuration [33, 41, 42]. In transmitting mode, a source would be connected to the TL terminals (the antenna gap), launching a travelling wave that propagates outwards along the wires. Near the gap region, the currents on neighboring wires oscillate 180° out-of-phase and radiation is effectively cancelled, as it is known from two-wire TLs [31–33]. The path difference between two neighboring wires, due to the extra half turn of the outer wire, generates an additional phase delay between the wires that increases with increasing distances from the gap. Radiation is maximum when the currents of neighboring wires become in-phase, which occurs in an annular ring of one wavelength λ circumference (see Chapter 1), the so-called the active region (indicated by the green dashed circle in Fig. 6.2d). The radiated beam is circularly polarized (see Fig. 6.3d), with LCP in $-z$ and RCP in $+z$ direction. Conversely in reception mode, LCP (RCP) illumination from below in $+z$ direction launches a travelling wave at the active zone that travels inwards (outwards), leading to strong fields (no fields) at the antenna gap in case of the 5-turn antenna (schematic Fig. 6.2b, right). Indeed, our near-field images confirm the directional wave launching in our infrared 5-turn spiral antenna. For RCP, we observe high amplitude signals mostly outside the green-dashed ring (Fig. 6.2d, right), and the near-field phase image clearly shows an increasing phase along the wires as can be appreciated by the transition from blue to white to red to black color, indicating outward wave propagation (Fig. 6.2j, right). In contrast, for LCP we observe significant amplitude signals mainly inside the green-dashed ring (Fig. 6.2d, left), and a constant near-field phase along the

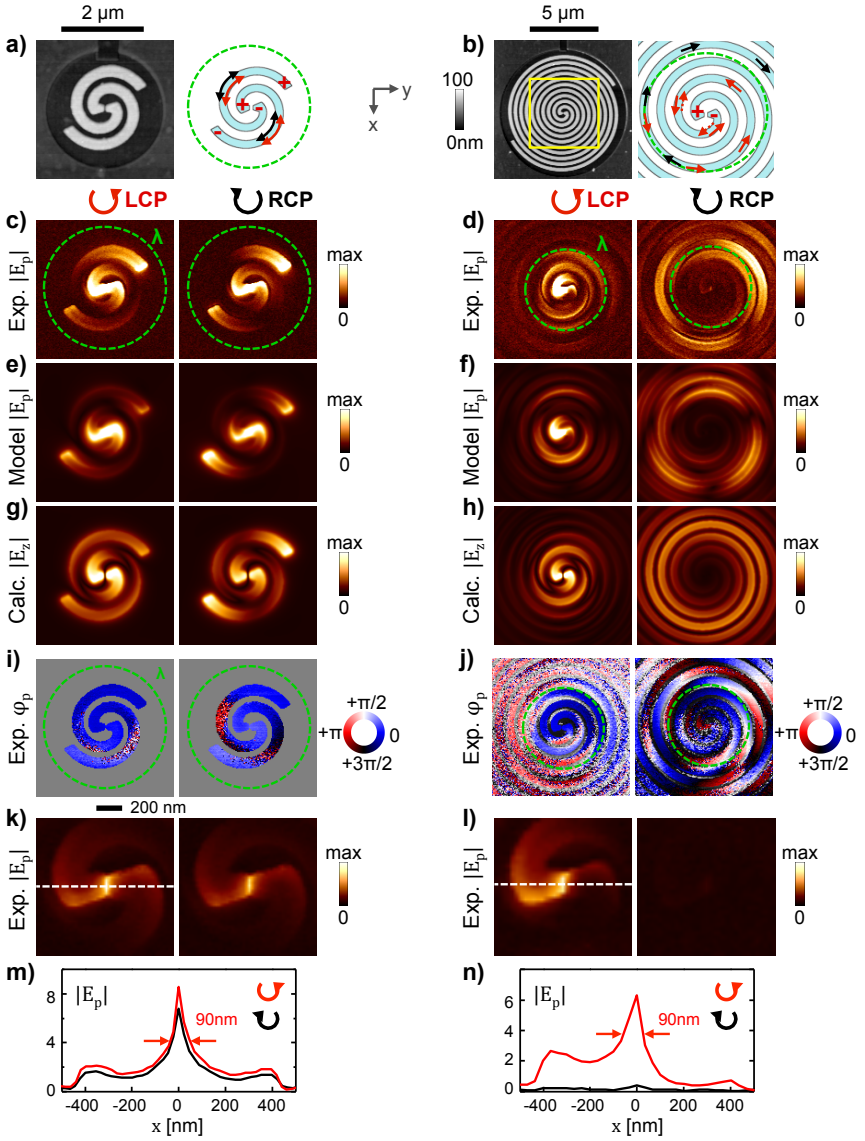

Figure 6.2: **Nanofocusing of infrared light with circular polarization contrast in infrared Archimedean spiral antennas.** **(a)** Left panel: Topography image of a 1-turn spiral antenna. Right panel: Illustration of a standing wave pattern on the antenna when illuminated with LCP or RCP **(b)**. Left panel: Topography image of 5-turn spiral antenna. Right panel: Illustration of directional wave launching at the active zone of the antenna (green dashed ring): Outward flowing currents (black arrows) excited by RCP, inward flowing currents (red arrows) excited by LCP illumination and subsequent reflection at the gap (red dashed arrows). **(c,d)** Experimental s-SNOM images of the antennas in **(a,b)**. Shown is the near-field amplitude $|E_p|$ for left-handed (LCP) and right-handed circular polarized (RCP) illumination. The color scale is saturated to show the antenna mode more clearly. **(e,f)** Modeled s-SNOM images. **(g,h)** Numerically calculated vertical electric field component, $|E_z|$ and φ_z. **(i,j)** Experimental near-field phase image, φ_p. **(k,l)** Digital zooms of the gap region of the near-field amplitude images shown in **(c,d)**. **(m,n)** Line profiles through the nanofocus at the antenna gap, extracted at the position indicated by the dashed line in **(k,l)**. Values of $|E_p|$ are in Volts as obtained from the pseudoheterodyne module.

wires, which we explain by an interference between the inward travelling wave and the subsequent reflected wave at the open-circuited gap (Fig. 6.2j, left).

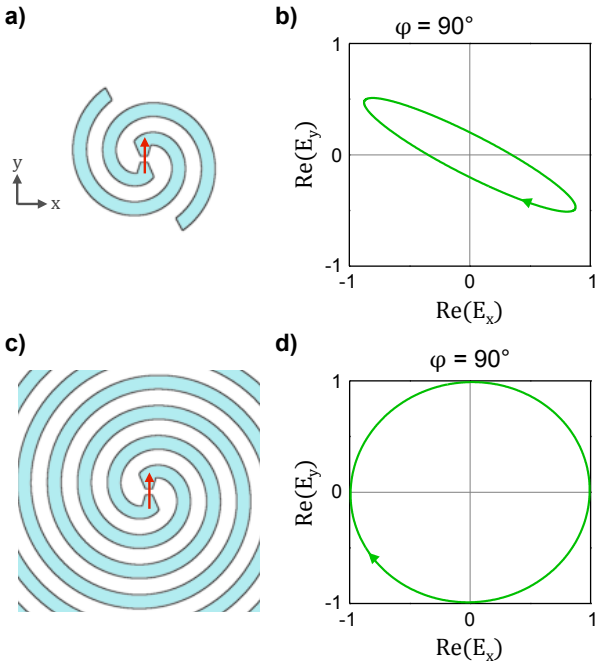

Figure 6.3: **Calculated radiation characteristics of our infrared 1-turn and 5-turn Archimedean spiral antennas shown in Fig. 2** The data are obtained by FDTD simulations assuming a wavelength of $\lambda_0 = 9.3$ μm. **(a)** Sketch of the 1-turn spiral antenna excited by an electric dipole placed inside the antenna gap. **(b)** Polarization state of the radiated light in +z- direction, showing an elliptical polarization state of axial ratio 5.5:1. **(c)** Sketch of the 5-turn spiral antenna excited by an electric dipole placed inside the antenna gap. **(d)** Polarization state of the radiated light in +z-direction, showing a circular polarization state (axial ratio is 1.02:1).

The negligible chiral optical response of the 1-turn spiral antenna (Fig. 6.2a) can be attributed to the arm length (3.7 μm) being short in terms of the wavelength ($\lambda_0 = 9.3$ μm). In transmitting mode, a wave launched at the gap first radiates with LCP, reflects at the outer wire ends and travels inwards, radiating with a circular polarization of opposite handedness, i.e. RCP. Numerical calculations (Fig. 6.3b) reveal that the 1-turn antenna radiates with strongly elliptical polarization (axial ratio 5.5:1). In reception mode, the antenna thus provides only poor discrimination between LCP and RCP illumination, which explains the negligible chiral optical near-field response observed in the experiment (Fig. 6.2c). Indeed, the phase images (Fig. 6.2i) show constant phase on the spiral antenna (blue color) indicative of a standing wave pattern as typically observed with linear antennas [112,113]. Our images thus demonstrate that in spiral antennas, travelling waves (5-turn antenna) are the cause for a strong chiral

optical response, while standing waves (1-turn antenna) are the cause for a negligible chiral optical response in the near-field.

As an interesting side aspect, we also observe the same, strong near-field contrast when we leave the illumination field fixed to LCP and compare the original right-wound 5-turn spiral antenna with its left-wound mirror image (Fig. 6.4). This result confirms that reversing the handedness of either the incident field or the structure itself produces the same change in the near-field response in our chiral antennas.

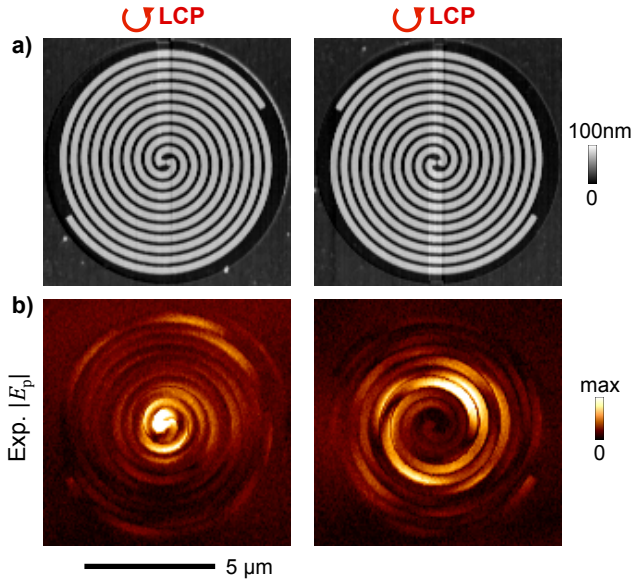

Figure 6.4: **Chiral optical near-field contrast between a right-wound Archimedean antenna and its left-wound mirror image for the same LCP illumination.** **(a)** Topography images. **(b)** Experimental near-field amplitude images of the antennas in **(a)** for LCP illumination.

Closer inspection of the near-field amplitude images reveals a highly localized, intense nanofocus (hot spot) inside the antenna gap (Figs. 6.2k,l). Interestingly, we see that the 5-turn antenna produces a hot spot only for LCP illumination, while the gap remains nearly dark for RCP (Fig. 6.2l). The 1-turn antenna, in contrast, generates a nanofocus for both LCP and RCP (Fig. 6.2k). We describe the polarization-selective generation of the nanofocus as the circular polarization contrast (CPC) of the antenna. To quantify it, we extracted line profiles from the near-field images in Figs. 6.2k,l (as indicated by the dashed line), determine the near-field amplitude, $|E_p|$, at the antenna gap (x=0) for both the LCP and RCP images and calculate the ratio CPC $= |E_p^{LCP}|/|E_p^{RCP}|$. Note that a direct and quantitative comparison between the two images is possible because only the polarization state of the illuminating beam was

changed between the two image acquisitions (by rotation of the linear polarizer P3) whereas the detection remained unchanged. For the 5-turn antenna, we obtain an impressive CPC of 16:1, which can also be appreciated by the strong peak at x=0 for LCP (red) and the very weak peak for RCP (black line) in Fig. 6.2n. The experimental result is confirmed by numerical calculations, predicting a CPC of 67:1 (with respect to E_{tot} at a height of 50 nm above the structures). This polarization-selective nanofocusing is a direct consequence of the inward (outward) wave launching on the antenna wires for LCP (RCP) observed in Fig. 6.2d. We note that the experimental value can be better matched by taking into account the slight ellipticity of the illuminating beam (see Section 6.3), then yielding a reduced CPC of 19:1 in the numerical calculations. In contrast, for the 1-turn antenna we obtain a near-unity (1.3:1) CPC (Fig. 6.2m). We attribute this effect to the negligible chiral optical near-field response of the antenna, as discussed above. Our results demonstrate the capability of spiral antennas to detect and enhance one specific handedness of the circular light, provided that the wire length (number of turns) is sufficiently long in terms of wavelength λ_0. We envision that this capability makes Archimedean spiral antennas a promising candidate for combining antenna-enhanced sensing with circular-polarization sensitivity in form of an integrated thin-film solution for novel spectroscopy, photodetector and polarimetric imaging applications. For example, the spiral antenna's sensitivity to the light's handedness could be used to develop ultra-compact full Stokes parameter polarimeters that do not require quarter wave plates or polarizers. Conversely, the spiral antenna's indifference to the orientation of linearly polarized illumination could simplify antenna-based sensing application by removing the constraint of sample alignment to the (polarized) light source, such as a laser.

Note that the nanofocus in the antenna gap (the one discussed above) is revealed in our near-field images when recording the p-component of the scattered light, E_p (Figs. 6.2k,l). This might be surprising and is in contrast to s-SNOM experiments with linear antennas, where detection of the p-component of the tip-scattered light typically yields a dark gap [112, 113, 123]. We explain the bright gap in our near-field images by a strong scattering of the antenna near fields by the tip via the antenna itself into the far field, which predominates over the direct scattering of the near fields by the tip [113]. Furthermore, the spiral antennas radiate with both s- and p-component as a result of the circular polarization of the 5-turn spiral antenna, and the tilted elliptical polarization of the 1-turn spiral antenna (Fig. 6.3). Thus the in-plane component of the field inside the gap is transferred to the p-component of the scattered field. In

contrast, linear antennas radiate entirely in s-polarization normal to the antenna axis, thus the in-plane component of the field inside the gap is only contained in the s-component (assuming light detection normal to the antenna axis) and consequently a dark gap is observed when the p-component is measured [112]. The employed s-SNOM model, which that properly accounts for the complex-valued combination of near-field components, not only confirms the bright gap, but also some specific features in the experimental near-field distributions (Figs. 6.2e,f). In more detail, the model correctly predicts the stronger field enhancement on the wire edges than on the wire center (Fig. 6.2e), the breaks (dark spots) in the ring-shape structure (Fig. 6.2f, RCP) and the general asymmetric nature of the amplitude distribution observed in the experiment. This detailed reproduction of the experimental images supports the validity of the s-SNOM scattering model with the spiral antennas.

We furthermore note that the Archimedean spiral geometry is also found in plasmonic lenses [184, 185], whose near fields have been imaged employing circularly polarized illumination [186, 187]. These spiral lenses are based on the launching of surface plasmons on thin metal films at spiral grooves with a defined geometric phase, where a nanofocus is generated on the metal film by a radial and inwards propagation of the plasmons. This mechanism is different to infrared and radiofrequency spiral antennas, where the illuminating beam excites currents in the metal wires, which travels tangentially and along the wires to produce a field concentration at the antenna gap.

6.6 Near-field mapping of planar metasurfaces

To further demonstrate the wide application potential of our technique and to obtain new insights in the chiral optical near-field response of metal nanostructures, we image the chiral near-field distributions that govern CD in planar chiral metasurfaces [156–160,162–166,169,170]. To this end, we fabricated two examples: The first design consists of a single-layer array of infrared-resonant metal rosettes (Fig. 6.5a) which exhibits very little CD [156–160, 162, 165, 169, 170]. The second design consists of an asymmetric arrangement of dipole and monopole antennas, as well as a horizontal wire acting as the ground plane for the monopole antenna (Fig. 6.5f) [177, 178]. This metasurface produces strong CD due to a Fano resonance induced by capacitive coupling between the dipole and monopole antenna. The weak and strong CD of both structures can be appreciated with the calculated transmission spectra in Fig. 6.5e and 6.5j, respectively.

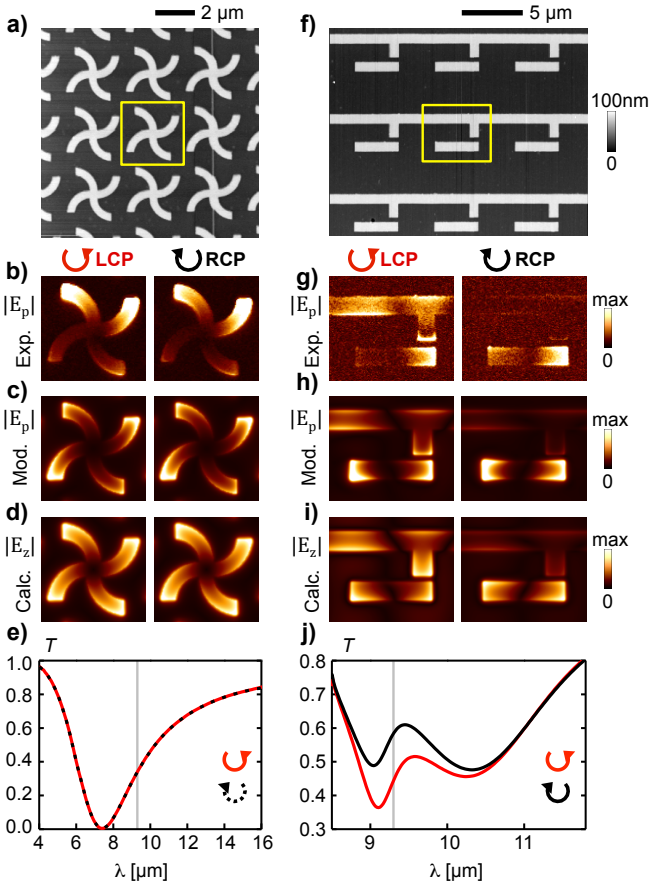

Figure 6.5: **Chiral near-field distributions in planar chiral metasurfaces that govern the circular dichroism response in the far field.** **(a)** Topography image of a periodic array of infrared-resonant rosettes (four arms of a 1/4-turn). **(b)** Experimental s-SNOM images, showing the near-field amplitude images $|E_p|$ for left-handed (LCP) and right-handed circular polarized (RCP) illumination. **(c)** Modeled s-SNOM images. **(d)** Numerically calculated vertical electric field component, $|E_z|$ and φ_z. **(e)** Calculated transmission spectra, T, of the rosette metasurface in **(a)** for LCP (red) and RCP (black dashed). **(f)** Topography image of an asymmetric dipole-monopole metasurface, consisting of a dipole antenna (3.58 μm x 0.79 μm) that capacitively couples to a monopole antenna (0.79 μm x 1.125 μm) connected to horizontal wire (ground plane). **(g)** Experimental s-SNOM images. **(h)** Modeled s-SNOM images. **(i)** Numerically calculated vertical electric field component. **(j)** Calculated transmission spectra, T, of the asymmetric dipole-monopole metasurface in **(f)**. The vertical gray line marks the imaging wavelength $\lambda_0 = 9.3$ μm.

With the rosette metasurface (Fig. 6.5b), noticeably, we find that the near-field images are nearly identical for LCP and RCP despite of the chiral geometry of the rosettes. In detail, our images show the same mode structure for LCP and RCP, exhibiting strong amplitude signals at the four arm ends and a node at the spiral center, and the difference in near-field amplitude is negligible. We thus observe no significant differences in the chiral optical response in the near-field of the single-layer rosette

metasurface. This finding is consistent with the small to negligible CD observed in far-field studies of similar single-layer structures [156, 158–162, 164, 166, 170] which was attributed to the missing of a significant magnetic mode [158–160]. Here we propose an alternative explanation along the lines of antenna theory, which is motivated by the similarities of the rosettes with the 1-turn spiral antenna (Fig. 6.2a): Both show small near-field contrast between LCP and RCP despite their obvious planar chiral geometry. Describing the rosettes as four-arm spiral antennas [33], we notice that the rosettes' arm length (1.5 μm) is much shorter than the wavelength λ_0. Consequently, a standing wave pattern rather than a travelling wave is formed on the antenna arms, leading to a nearly linear polarization of the antenna radiation, hence the rosettes' poor discrimination between LCP and RCP illumination.

In contrast, the asymmetric dipole-monopole metasurface shows drastically different near-field responses between LCP and RCP illumination (Fig. 6.5g). While the dipole antenna is always excited, we find strong fields at the monopole antenna and the horizontal wire only for LCP illumination, while the fields almost vanish for RCP. This on-off switching of the fields is caused by a Fano resonance induced by capacitive coupling between the dipole and monopole [177, 178]. Because of Ohmic losses in real metals, the fields observed at the monopole antenna cause additional absorption in the structure for LCP illumination, while this extra absorption is not present for RCP. The underlying physics of this finding is described in detail in ref. [177]. Importantly, our imaging technique reveals the different chiral near-field distributions as the cause for the CD in the asymmetric dipole-monopole metasurface. This capability we consider to be crucial for the further development of planar chiral structures with strong CD (in absorption) effects. Note that the modeled s-SNOM images (Figs. 6.5c,h) and the numerical calculation (Figs. 6.5d,i) qualitatively confirm the experimental images for both structures (Figs. 6.5b,g). The quantitative differences (asymmetries in the experimental images) can be attributed to the imperfect experimental conditions and the simplified description of the s-SNOM tip as a point dipole in the s-SNOM scattering model.

6.7 Conclusions

In conclusion, we have demonstrated, for the first time, the real-space mapping of chiral near-field distributions in planar chiral antennas and metasurfaces with s-SNOM. To

this end, we have developed a new imaging modality which employs circularly polarized illumination in combination with interferometric detection. Applied to infrared Archimedean spiral antennas, our technique revealed that left- and right-handed circularly polarized light can produce strongly different near-field distributions, provided that the antenna arms are long enough in terms of the wavelength. We have shown that this effect can be exploited to selectively nanofocus incident light of only one specific handedness, which could lead to new ultracompact polarimeter applications. Imaging planar chiral metasurfaces, we have found nearly identical near-field distributions in case of single-layer rosettes while drastically different near-field distributions were observed with an asymmetric dipole-monopole metasurface, which correlates with the weak and strong circular dichroism of these structures, respectively. Our imaging technique thus paves the way for a fundamental and detailed verification of the chiral optical effects in the near field, which will play an important role for the development and optimization of planar chiral metasurfaces and their applications. Furthermore, our results indicate an interesting connection between chiral infrared antennas and radiofrequency antenna theory: The infrared spiral antenna shows a chiral optical response similar to its larger, radiofrequency counterparts and this response can be described in terms of travelling and standing waves. This finding suggests that many RF antenna concepts are potentially suitable for building novel infrared chiral antenna and metasurfaces, which is certainly worth to be explored further in the future.

List of publications

This thesis is based on the following publications:

1. Paulo Sarriugarte, Martin Schnell, Pablo Alonso-Gonzalez, Libe Arzubiaga, Federico Golmar, Fèlix Casanova, Luis E. Hueso and Rainer Hillenbrand, "Propagation and Nanofocusing of Infrared Surface Plasmons on Tapered Transmission Lines: Influence of the Substrate"
   Optics Communications **285**, 3378 (2012).
   (Chapter 3)

2. Paulo Sarriugarte, Martin Schnell, Andrey Chuvilin and Rainer Hillenbrand, "Polarization-resolved Near-field Characterization of Nanoscale Infrared Modes in Transmission Lines Fabricated by Gallium and Helium Ion Beam Milling"
   ACS Photonics **1**, 604 (2014).
   (Chapter 5)

3. Martin Schnell*, Paulo Sarriugarte*, Tomas Neuman, Alexander B. Khanikaev, Gennady Shvets, Javier Aizpurua and Rainer Hillenbrand, "Real-Space Mapping of the Chiral Near-Field Distributions in Spiral Antennas and Planar Metasurfaces"
   Nano Letters **16**, 663-670 (2016).
   * Equally contributed
   (Chapter 6)

Other publications:

1. Alexander B. Khanikaev, Nihal Arju, Zhiyuan Fan, David Purtseladze, Feng Lu, Jongwon Lee, Paulo Sarriugarte, Martin Schnell, Rainer Hillenbrand, Mikhail A. Belkin and Gennady Shvets, "Experimental demonstration of the microscopic origin of circular dichroism in two-dimensional metamaterials"
Nature Communications **7**, 12045 (2016).

2. Alexey O. Bak, Edward O. Yoxall, Paulo Sarriugarte, Vincenzo Giannini, Stefan A. Maier, Rainer Hillenbrand, John B. Pendry and Chris C. Phillips, "Harnessing a Quantum Design Approach for making Low-loss Superlenses"
Nano Letters **16**, 1609-1613 (2016).

3. Andrea Blanco-Redondo, Paulo Sarriugarte, Angel Garcia-Adeva, Joseba Zubia, and Rainer Hillenbrand, "Local Field Enhancement of Mid-Infrared Light in an Integrated Photonic-Plasmonic Structure"
Journal Of Lightwave Technology **33**, 368 (2015).

4. Andrea Blanco-Redondo, Paulo Sarriugarte, Angel Garcia-Adeva, Joseba Zubia, and Rainer Hillenbrand, "Coupling mid-infrared light from a photonic crystal waveguide to metallic transmission lines"
Applied Physics Letters **104**, 011105 (2014).

5. Shang-Chi Jiang, Xiang Xiong, Paulo Sarriugarte, Sheng-Wei Jiang, Xiao-Bo Yin, Yuan Wang, Ru-Wen Peng, Di Wu, Rainer Hillenbrand, Xiang Zhang, and Mu Wang, "Tuning the polarization state of light via time retardation with a microstructured surface"
Physical Review B **88**, 161104(R) (2013).

6. Pablo Alonso-Gonzalez, Martin Schnell, Paulo Sarriugarte, Heidar Sobhani, Chihhui Wu, Nihal Arju, Alexander Khanikaev, Federico Golmar, Pablo Albella, Libe Arzubiaga, Fèlix Casanova, Luis E. Hueso, Peter Nordlander, Gennady Shvets and Rainer Hillenbrand, "Real-Space Mapping of Fano Interference in Plasmonic Metamolecules"
Nano Letters **11**, 3922 (2011).

Acknowledgements

I would like to thank professor Txema Pitarke for introducing me to the research world and giving me the opportunity to join nanoGUNE. I acknowledge the financial support of my Ph.D. work from the ÔIkertzaileak prestatzeko doktoretza-aurreko programakoÕ promoted by the Department of Education, Universities and Research of the Basque Government.

I would also like to thank my supervisor Rainer Hillenbrand for being so enthusiastic and pushy in every aspect of the research, for teaching me so much about optics and writing, guiding me through my scientific work, and for the climbing days we spent together. I am also thankful to the whole group of nanooptics. It has being a pleasure to work with all of you during these years. I would like to especially mention my college Martin Schnell who has been my particular teacher and has helped me every single time. I also thank my college and friend Pablo Alonso who is always ready to help, discuss or just talk. To Sasha for his always valuable advises.

To the Nanodevices group and Advanced Electron Microscopy Laboratory at CIC nanoGUNE for the great collaboration. Especially to Libe Arzubiaga and Federico Golmar who have fabricate the first samples I measured, and to Andrey Chuvilin who has guide me through the FIB fabrication for some years already.

I also want to thank the administration of CIC nanoGUNE for their assistance beyond their duties. Julene has solved several "last minute" problems for me. I cannot forget to thank the rest of the colleges working at nanoGUNE. Thank you for the great atmosphere we have at nanoGUNE and outside nanoGUNE.

Tesian zehar nanoGUNEn izan dudan bizitza ez zatekeen gauza bera lagun batzuk ondoan izan ez banitu: Estitxu, Jon ander, Amets, Jokin, Txema, Olatz, Juan, Aitor, Cesar, Iban, Jon eta beste hainbeste. Eskerri asko zuei.

Nire kuadrilakoak ere eskertu nahiko nituzke, nigan sinisteagatik eta horrenbeste momentu on eman dizkidatelako. Eta batez ere beti hor eduki ditudalako, onerako eta txarrerako, diren bigarren familia bezala.

Ezingo nuke aipatu gabe utzi nire bizitzako urte hauek nire alboan igaro dituen pertsona. Zure alaitasun eta goxotasunak bost urtetan zehar argitu dizkit goizak. Eskerrik asko nire bide lagun, bikote, maitale, soka lagun eta konplize izatearren nire bizitzako zati honetan, ezin izango nuen zu gabe burutu begi eder.

Azkenik, nire guraso Jesus Mari eta Josefina, eta nire anai-arreba Unai eta Irati ere eskertu nahi ditut beti erakutsi duten ulerkortasunak eta eman didaten babesak eta laguntzak ez dutelako preziorik. Beraiengandik ikasten jarraitzen dudalako, baita momentu eskasenetan ere, eta nire euskarri trinkoena direlako. Eskerrik asko zuiei.

Orain ez nintzateke naizena izango guztia hauengatik ez balitz, eskerrik asko.

Paulo

Donostia, 2017ko ekainaren 1a

References

[1] Gutberlet, A., Schwaab, G., Birer, O., Masia, M., Kaczmarek, A., Forbert, H., Havenith, M., Marx, D., *Science* **324**, 1545-1548 (2009).

[2] Li, Z. Q., Henriksen, E. A., Jiang, Z., Hao, Z., Martin, M. C., Kim, P., Stormer, H. L., Basov, D. N., *Nature Phys.* **4**, 532-535 (2008).

[3] Griffiths, P. R., de Haseth, J. A., *Fourier Transform Infrared Spectrometry*, John Wiley & Sons: Hoboken, New Jersey, (2007).

[4] Born, M., Wolf, E., *Principles of Optics*, Cambridge University Press: Cambridge, (1999).

[5] Mühlschlegel, P., Eisler, H.-J., Martin, O. J. F., Hecht, B., Pohl, D. W., *Science* **308**, 1607-1609 (2005).

[6] Novotny, L., *Phys. Rev. Lett.* **98**, 266802 (2007).

[7] Weeber, J.-C., Krenn, J., Dereux, a., Lamprecht, B., Lacroute, Y., Goudonnet, J., *Phys. Rev. B* **64**, 045411 (2001).

[8] Maier, S. A., Kik, P. G., Atwater, H. a, Meltzer, S., Harel, E., Koel, B. E., Requicha, A. A. G., *Nat. Mater.* **2**, 229-232 (2003).

[9] Bozhevolnyi, S. I., Volkov, V. S., Devaux, E., Laluet, J.-Y., Ebbesen, T. W., *Nature* **440**, 508-511 (2006).

[10] Schuller, J. A., Barnard, E. S., Cai, W., Jun, Y. C., White, J. S., Brongersma, M. I., *Nat. Mater.* **9**, 193-204 (2010).

[11] Moskovits, M., *Rev. Mod. Phys.* **57**, 783-826 (1985).

[12] Xu, H., Bjerneld, E. J., KŠll, M., Börjesson, L., *Phys. Rev. Lett.* **83**, 4357-4360 (1999).

[13] Nie, S., Emory, S. R., *Science* **275**, 1102-1106 (1997).

[14] Kneipp, K., Yang Wang, Y., Harald Kneipp, H., Perelman, L. T., Itzkan, I., Dasari, R. R., Feld, M. S., *Phys. Rev. Lett.* **78**, 1667-1670 (1997).

[15] Neubrech, F., Pucci, A., Cornelius, T., Karim, S., Garcia-Etxarri, A., Aizpurua, J., *Phys. Rev. Lett.* **101**, 157403 (2008).

[16] Adato, R., Yanik, A. A., Amsden, J. J., Kaplan, D. L., Omenetto, F. G., Hong, M. K., Erramilli, S., Altug, H., *Proc. Natl. Acad. Sci. U. S. A.* **106**, 19227-19232 (2009).

[17] Huth, F., Govyadinov, A., Amarie, S., Nuansing, W., Keilmann, F., Hillenbrand, R., *Nano Lett.* **12**, 3973-3978 (2012).

[18] Babadjanyan, A. J., Margaryan, N. L., Nerkararyan, K. V., *J. Appl. Phys.* **87**, 3785-3788 (2000).

[19] Stockman, M., *Phys. Rev. Lett.* **93**93, 137404 (2004).

[20] Ropers, C., Neacsu, C. C., Elsaesser, T., Albrecht, M., Raschke, M. B., Lienau, C., *Nano Lett.* **7**, 2784-2788 (2007).

[21] Verhagen, E., Spasenović, M., Polman, A., Kuipers, L., *Phys. Rev. Lett.* **102**, 203904 (2009).

[22] De Angelis, F., Das, G., Candeloro, P., Patrini, M., Galli, M., Bek, A., Lazzarino, M., Maksymov, I., Liberale, C., Andreani, L. C., Di Fabrizio, E., *Nat. Nanotechnol.* **5**, 67-72 (2010).

[23] Dionne, J., Sweatlock, L., Atwater, H., Polman, A.,*Phys. Rev. B* **73**, 035407 (2006).

[24] Pile, D. F. P., Gramotnev, D. K., *Appl. Phys. Lett.* **89**, 041111 (2006).

[25] Choi, H., Pile, D. F., Nam, S., Bartal, G., Zhang, X., *Opt. Express* **17**, 7519-7524 (2009).

[26] Vedantam, S., Lee, H., Tang, J., Conway, J., Staffaroni, M., Yablonovitch, E. A., *Nano Lett.* **9**, 3447-3452 (2009).

[27] Engheta, N., *Science* **317**, 1698-1702 (2007).

[28] Maier, S., Andrews, S., Martín-Moreno, L., García-Vidal, F., *Phys. Rev. Lett.* **97**, 176805 (2006).

[29] Bousseksou, A., Babuty, A., Tetienne, J., Braive, R., Beaudoin, G., Sagnes, I., Wilde, Y. De, Colombelli, R., *Opt. Express* **20**, 13738-13747 (2012).

[30] Rusina, A., Durach, M., Nelson, K., Stockman, M., *Opt. Express* **16**, 18576-18589 (2008).

[31] Krenz, P. M., Olmon, R. L., Lail, B. A., Raschke, M. B., Boreman, G. D., *Opt. Express* **18**, 21678-21686 (2010).

[32] Schnell, M., Alonso-González, P., Arzubiaga, L., Casanova, F., Hueso, L. E., Chuvilin, A., Hillenbrand, R., *Nat. Photon.* **5**, 283-287 (2011).

[33] Balanis, C. A., *Antenna Theory;* John Wiley & Sons, Inc.: Hoboken, New Jersey (2005).

[34] Alu, A., Engheta, N., *Phys. Rev. Lett.. 101*, 043901 (2008).

[35] Schnell, M., *Infrared Nanophotonics based on Metal Antennas and Transmission Lines.* PhD thesis, University of the Basque Country (2012).

[36] Novotny, L., Hecht, B., *Principles of Nano-Optics*, Cambridge University Press: Cambridge, (2006).

[37] Straw, R. D., Andress, K., Cebik, L. B., Severns, R., Witt, F., *The ARRL Antenna Book*, (19 Edition) The American Radio League, Inc., Newington, CT, 2000).

[38] Goubau, G., *J. Appl. Phys.* **21**, 1119-1128 (1950).

[39] Biagioni, P., Huang, J. S., Hecht, B., *arXiv:1103.1568v1* [physics.optics] (2011).

[40] Orfanidis S. J., *Electromagnetic Waves and Antennas* Online book, retrieved May 2017. www.ece.rutgers.edu/ orfanidi/ewa.

[41] Dyson, J., *IRE Trans. Antennas Propag.* **7**, 181-187 (1959).

[42] Kaiser, J., *IRE Trans. Antennas Propag.* **8**, 312-323 (1960).

[43] Jackson, J. D., *Classical Electrodynamics*, John Wiley & Sons, (1975).

[44] Garcia-Etxarri, A., *Modeling of plasmonic nanoantennas for optical microscopy and surface enhanced spectroscopy.* PhD thesis, University of the Basque Country (2010).

[45] Wolf, E., Nieto-Vesperinas, M., *J. Opt. Soc. Am. A* **2**, 886-889 (1985).

[46] Gramotnev, D. K., Bozhevolnyi, S. I., *Nat. Photon.* **4**, 83-91 (2010).

[47] Barnes, W. L., Dereux, A., Ebbesen, T. W., *Nature* **424**, 824-830 (2003).

[48] Johnson, P. B. & Christy, R. W., *Phys. Rev. B* **6**, 4370 (1972).

[49] Palik, E. D., *Handbook of Optical Constants of Solids*, Academic Press, San Diego, (1985).

[50] Ordal, M. A., Long, L. L., Bell, R. J., Bell, S. E., Bell, R. R., Alexander, R. W. Jr., Ward, C. A., *Appl. Opt.* **22**, 1099-1119 (1983).

[51] Bennett, H. E., Bennett, J. M., *Optical properties and electronic structure of metals and alloys*, North-Holland, New York, (1966).

[52] Giannini, V., Fernandez-Dominguez, A. I., Heck, S. C., Maier, S. A., *Chem. Rev.* **111**, 3888-3912 (2011).

[53] Hecht, E., *Optics* (4th Edition), Addison Wesley, (2001).

[54] García de Abajo, F. J., *Rev. Mod. Phys.* **82**(1), 209-275 (2010).

[55] Coenen, T., *Angle resolved cathodoluminescence nanoscopy.* PhD thesis, University of Amsterdam (2014).

[56] Das, P., Chini, T. K., Pond, J., *J. Phys. Chem. C* **116**, 15610-15619 (2012).

[57] Nelayah, J., Kociak, M., Stéphan, O., García de Abajo, F. J., Tencé, M., Henrard, L., Taverna, D., Pastoriza-Santos, I., Liz-Marzán, L. M., Colliex, C., *Nature Phys.* **3**, 348-353 (2007).

[58] Chu, M.-W., Myroshnychenko, V., Chen, C., Deng, J.-P., Mou, C.-Y., García de Abajo, F. J., *Nano Lett.* **9**, 399-404 (2009).

[59] Koh, A., Fernández-Domínguez, A. I., McComb, D., Maier, S., Yang, J., *Nano Lett.* **11**, 1323-1330 (2011).

[60] Schmidt, F.-P., Ditlbacher, H., Hohenester, U., Hohenau, A., Hofer, F., Krenn, J. R., *Nano Lett.* **12**, 5780-5783 (2012).

[61] Huth, F., Chuvilin, A., Schnell, M., Amenabar, I., Krutokhvostov, R., Lopatin, S., Hillenbrand, R., *Nano Lett.* **13**, 1065-1072 (2013).

[62] Ghenuche, P., Cherukulappurath, S., Taminiau, T. H., Van Hulst, N. F., Quidant, R., *Phys. Rev. Lett.* **101**, 116805 (2008).

[63] Bouhelier, A., Bachelot, R., Lerondel, G., Kostcheev, S., Royer, P., Wiederrecht, G. P., *Phys. Rev. Lett.* **95**, 267405 (2005).

[64] Schuck, P. J., Fromm, D. P., Sundaramurthy, A., Kino, G. S., Moerner, W. E., *Phys. Rev. Lett.* **94**, 017402 (2005).

[65] Beversluis, M. R., Bouhelier, A., Novotny, L., *Phys. Rev. B* **68**, 115433 (2003).

[66] Viarbitskaya, S., Teulle, A., Marty, R., Sharma, J., Girard, C., Arbouet, A., Dujardin, E., *Nat. Mater.* **12**, 426-432 (2013).

[67] Wang, T., Halaney, D., Ho, D., Feldman, M. D., Milner, T. E., *Biomedical Opt. Express* **4**, 584-595 (2013).

[68] O. Schmidt, M. Bauer, C. Wiemann, R. Porath, M. Scharte, O. Andreyev, G. Schönhense, M. Aeschlimann *Applied Phisics B: Lasers and Optics* **74**, 223-227 (2002)

[69] Cinchetti, M., Gloskovskii, A., Nepjiko, S.A., Schonhense, G., Rochholz, H., Kreiter, M., *Phys. Rev. Lett.* **95**, 047601 (2005).

[70] Aeschlimann, M., Bauer, M., Bayer, D., Brixner, T., García de Abajo, F. J., Pfeiffer, W., Rohmer, M., Spindler, C., Steeb, F., *Nature* **446**, 301-304 (2007).

[71] Douillard, L., Charra, F., Korczak, Z., Bachelot R., Kostcheev, S., Lerondel, G., Adam, P.-M., Royer, P., *Nano Lett.* **8**, 935-940 (2008).

[72] Quan Sun, Q., Ueno, K., Yu, H., Kubo, A., Matsuo, Y., Misawa, H., *Light: Science & Applications* **2**, e118 (2013).

[73] Pohl, D.W., Denk, S., Ferrell, T., *Appl. Phys. Lett.* **44**, 651-653 (1984).

[74] Betzig, E., Isaacson, M., Lewis, A., *Appl. Phys. Lett.* **51**, 2088-2090 (1987).

[75] Betzig, E., Trautmann, J. K., Harris, T. D., Weiner, J. S., Kostelak, R. L., *Science* **251**, 1468-1470 (1991).

[76] Flück, E., van Hulst, N. F., Vos, W. L., Kuipers, L., *Physical Review E* **68**, 015601 (2003).

[77] Hillenbrand, R., Keilmann, F., *Applied Physics B* **73**, 239-243 (2001).

[78] Hillenbrand, R., Keilmann, F., Hanarp, P., Sutherland, D. S., Aizpurua, J., *Appl. Phys. Lett.* **83**, 368-370 (2003).

[79] Keilmann, F., Hillenbrand, R., *Phil. Trans. R. Soc. A* **362**, 787-805 (2004).

[80] Olmon, R. L., Krenz, P. M., Jones, A. C., Boreman, G. D., Raschke, M. B., *Opt. Express* **16**, 20295-20305 (2008).

[81] Tanaka, Y., Ishiguro, H., Fujiwara, H., Yokota, Y., Ueno, K., Misawa, H., Sasaki, K., *Opt. Express* **19**, 7726-7733 (2011).

[82] Inouye, Y., Kawata, S., *Opt. Lett.* **19**, 159-161 (1994).

[83] Wickramasinghe, H. K., Williams, C. C., *Apertureless near field optical microscope.* U.S. Patent, 4,947,034 (1990).

[84] Garcia-Etxarri, A., Romero, I., García de Abajo, F. J., Hillenbrand, R., Aizpurua, J., *Phys. Rev. B: Condens. Matter Mater. Phys.* **79**, 125439 (2009).

[85] Kim, D. S., Kim, Z. H., *Journal of the Korean Physical Society* **52**, 17-20 (2008).

[86] Esteban, R., Vogelgesang, R., Dorfmüller, J., Dmitriev, A., Rockstuhl, C., Etrich, C., Kern, K. *Nano Lett.* **8**, 3155-3159 (2008).

[87] Rang, M., Jones, A. C., Zhou, F., Li, Z.-Y., Wiley, B. J., Xia, Y., Raschke, M. B., *Nano Lett.* **8** 3357-3363 (2008).

[88] Knoll, B., Keilmann, F., *Optics Communications* **162**, 177-181 (1999).

[89] Huber, A. J., *Nanoscale Surface-Polariton Spectroscopy by Mid- and Far Infrared Near-Field Microscopy.* PhD thesis, Technische Universität, (2010).

[90] Hillenbrand, R., Keilmann, F., *Phys. Rev. Lett.* **85**, 3029-3032 (2000).

[91] Ocelic, N., *Quantitative Near-Field Phonon Polariton Spectroscopy.* PhD thesis, Technische Universität, (2007).

[92] Ocelic, N., Huber, A., Hillenbrand, R., *Appl. Phys. Lett.* **89**, 101124 (2006).

[93] Hillenbrand, R., *Nahfeldoptische Amplituden- und Phasenkontrastmikroskopie zur nanoskopischen Abbildung von Materialkontrast und optisch resonanten Partikeln.* PhD thesis, Technische Universität, (2001).

[94] Hillenbrand, R., Taubner, T., Keilmann, F., *Nature* **418**, 159-162 (2002).

[95] Huber, A. J., Kazantsev, D., Keilmann, F., Wittborn, J., Hillenbrand, R., *Advanced Materials* **19**, 2209-2212 (2007).

[96] Jones, A. C., Olmon, R. L., Skrabalak, S. E., Wiley, B. J., Xia, Y. N., Raschke, M. B., *Nano Lett.* **9**, 2553-2558 (2009).

[97] Schnell, M., Garcia-etxarri, A., Huber, A. J., Crozier, K. B., Borisov, A., Aizpurua, J., Hillenbrand, R., *J. Phys. Chem. C* **114**, 7341-7345 (2010).

[98] Sarriugarte, P., Schnell, M., Chuvilin, A., Hillenbrand, R., *ACS Photonics* **1**, 604 (2014).

[99] Schnell, M., Garcia-Etxarri, A., Alkorta, J., Aizpurua, J., Hillenbrand, R., *Nano Lett.* **10**, 3524-3528 (2010).

[100] Fano, U., *Physical Review* **124** (6), 1866 (1961).

[101] Faist, J., Capasso, F., Sirtori, C., West, K. W., Pfeiffer, L. N., *Nature* **390**, 589-591 (1997).

[102] Miroshnichenko, A. E., Flach, S., Kivshar, Y. S., *Rev. Mod. Phys.* **82**(3), 2257 (2010).

[103] Zhang, W., Govorov, A. O., Bryant, G. W., *Phys. Rev. Lett.* **97**, 146804 (2006).

[104] Kroner, M., Govorov, A. O., Remi, S., Biedermann, B., Seidl, S., Badolato, A., Petroff, P. M., Zhang, W., Barbour, R., Gerardot, B. D., Warburton, R. J., Karrai, K., *Nature* **451**, 311-314 (2008).

[105] Fan, J. A., Bao, K., Wu, C., Bao, J., Bardhan, R., Halas, N. J., Manoharan, V. N., Shvets, G., Nordlander, P., Capasso, F., *Nano Lett.* **10**, 4680-4685 (2010).

[106] Fan, J. A., Wu, C., Bao, K., Bao, J., Bardhan, R., Halas, N. J., Manoharan, V. N., Nordlander, P., Shvets, G., Capasso, F., *Science* **328**, 1135-1138 (2010).

[107] Verellen, N., Sonnefraud, Y., Sobhani, H., Hao, F., Moshchalkov, V. V., Dorpe, P. V., Nordlander, P., Maier, S. A., *Nano Lett.* **9**, 1663-1667 (2009).

[108] Hentschel, M., Saliba, M., Vogelgesang, R., Giessen, H., Alivisatos, A. P., Liu, N., *Nano Lett.* **10**, 2721-2726 (2010).

[109] Alonso-González, P., Schnell, M., Sarriugarte, P., Sobhani, H., Wu, C., Arju, N., Khanikaev, A., Golmar, F., Albella, P., Arzubiaga, L., Casanova, F., Hueso, L. E., Nordlander, P.,Shvets, G., Hillenbrand, R., *Nano Lett.* **11**, 3922 (2011).

[110] Jiang, S.-C., Xiong, X., Sarriugarte, P., Jiang, S.-W., Yin, X.-B., Wang, Y., Peng, R.-W., Wu, D., Hillenbrand, R., Zhang, X., Wang, M., *Physical Review B* **88**, 161104(R) (2013).

[111] Sarriugarte, P., Schnell, M., Alonso-González, P., Arzubiaga, L., Golmar, F., Casanova, F., Hueso, L. E., Hillenbrand, R., *Opt. Commun.* **285**, 3378-3382 (2012).

[112] Alonso-González, P., Albella, P., Schnell, M., Chen, J., Huth, F., Garcia-Etxarri, A., Casanova, F., Golmar, F., Arzubiaga, L., Hueso, L. E., Aizpurua, J., Hillenbrand, R., *Nat. Commun.* **3**, 684 (2012).

[113] Neuman, T., Alonso-González, P., Garcia-Etxarri, A., Schnell, M., Hillenbrand, R., Aizpurua, J., *Laser Photonics Rev.* **9**, 637-649 (2015).

[114] Schnell, M., Sarriugarte, P., Neuman, T., Khanikaev, A. B., Shvets, G., Aizpurua, J., Hillenbrand, R., *Nano Lett.* **16**, 663-670 (2016).

[115] Mandviwala, T., Lail, B., Boreman, G., *Microwave and Optical Technology Letters* **47**, 17-20 (2005).

[116] Raether, H., *Surface plasmons on smooth and rough surfaces and on gratings*, (Vol. 111), Springer, (1988).

[117] Huang, J.-S., Feichtner, T., Biagioni, P., Hecht, B., *Nano Lett.* **9**, 1897-1902 (2009).

[118] Cai, W., Shin, W., Fan, S., Brongersma, M. L., *Advanced Materials* **22**, 5120-5124 (2010).

[119] Neubrech, F., Kolb, T., Lovrincic, R., Fahsold, G., Aizpurua, J., Cornelius, T. W., Toimil-Molares, M. E., Neumann, R., Karim, S., Pucci, A., *Appl. Phys. Lett.* **89**, 253104 (2006).

[120] Holmgaard, T., Bozhevolnyi, S. I., *Phys. Rev. B* **75** (2007).

[121] Babuty, A., Bousseksou, A., Tetienne, J.-P., Moldovan Doyen, I., Sirtori, C., Beaudoin, G., Sagnes, I., De Wilde, Y., Colombelli, R., *Phys. Rev. Lett.* **104**, 226806 (2010).

[122] Tetienne, J. P., Bousseksou, A., Costantini, D., Colombelli, R., Babuty, A., Moldovan-Doyen, I., De Wilde, Y., Sirtori, C., Beaudoin, G., Largeau, L., Mauguin, O., Sagnes, I., *Appl. Phys. Lett.* **97**, 211110 (2010).

[123] Schnell, M., Garcia-Etxarri, A., Huber, A. J., Crozier, K., Aizpurua, J., Hillenbrand, R., *Nat. Photon.* **3**, 287-291 (2009).

[124] Cui, Z., *Nanofabrication: Principles, Capabilities and Limits*, Springer, Boston, MA, (2009).

[125] Isasa, M., *Spin orbitronics in metals*. PhD thesis, University of the Basque Country (2015).

[126] Haller, I., Hazakis, M., Srinivasan, R., *IBM Journal of Research and Development* **12**, 251 (1968).

[127] Dayen, J.-F., Faramarzi, V., Pauly, M., Kemp, N. T., Barbero, M., Pichon, B. P., Majjad, H., Begin-Colin, S., Doudin, B., *Nanotechnology* **21**, 335303 (2010).

[128] Huang, J.-S., Callegari, V., Geisler, P., Brüning, C., Kern, J., Prangsma, J. C., Wu, X., Feichtner, T., Ziegler, J., Weinmann, P., Kamp, M., Forchel, A., Biagioni, P., Sennhauser, U., Hecht, B., *Nat. Commun.* **1**, 150 (2010).

[129] Habteyes, T. G., Dhuey, S., Wood, E., Gargas, D., Cabrini, S., Schuck, P. J., Alivisatos, A. P., Leone, S. R., *ACS Nano* **6**, 5702-5709 (2012).

[130] Siegfried, T., Ekinci, Y., Martin, O. J.F., Sigg, H., *ACS Nano* **7**, 2751-2757 (2013).

[131] Debu, D. T., Ghosh, P. K., French, D., Herzog, J. B., *Opt. Mater. Express* **7**, 73-84 (2017).

[132] Yao, N., *Focused Ion Beam Systems: Basics and Applications*, Cambridge University Press: Cambridge, (2007).

[133] Canovic, S., Jonsson, T., Halvarsson, M., *J. Phys. Conf. Ser.* **126**, 012054 (2008).

[134] Kempshall, B. W., Schwarz, S. M., Prenitzer, B. I., Giannuzzi, L. A., Irwin, R. B., Stevie, F. A., *J. Vac. Sci. Technol. B* **19**, 749 (2001).

[135] Lofton, C., Sigmund, W., *Adv. Funct. Mater.* **15**, 1197-1208 (2005).

[136] Pors, A., Moreno, E., Martín-Moreno, L., Pendry, J. B., García-Vidal, F. J., *Phys. Rev. Lett.* **108**, 223905 (2012).

[137] Lu, Y.-J., Kim, J., Chen, H.-Y., Wu, C., Dabidian, N., Sanders, C. E., Wang, C.-Y., Lu, M.-Y., Li, B.-H., Qiu, X., Chang, W.-H., Chen, L.-J., Shvets, G., Shih, C.-K., Gwo, S., *Science* **337**, 450-453 (2012).

[138] Bak, A. O., Yoxall, E. O., Sarriugarte, P., Giannini, V., Maier, S. A., Hillenbrand, R., Pendry, J. B., Phillips, C. C., *Nano Lett.* **16**, 1609-1613 (2016).

[139] Einsle, J. F., Bouillard, J.-S., Dickson, W., Zayats, A. V., *Nanoscale Res. Lett.* **6**, 572 (2011).

[140] Marshall, M. M., Yang, J., Hall, A. R., *Scanning* **34**, 101-106 (2012).

[141] Bell, D. C., Lemme, M. C., Stern, L. A., Williams, J. R., Marcus, C. M., *Nanotechnology* **20**, 455301 (2009).

[142] Lemme, M. C., Bell, D. C., Williams, J. R., Stern, L. A., Baugher, B. W. H., Jarillo-Herrero, P., Marcus, C. M., *ACS Nano* **3**, 2674-2676 (2009).

[143] Wang, Y., Boden, S. A., Bagnall, D. M., Rutt, H. N., de Groot, C. H., *Nanotechnology* **23**, 395302 (2012).

[144] Melli, M., Polyakov, A., Gargas, D., Huynh, C., Scipioni, L., Bao, W., Ogletree, D. F., Schuck, P. J., Cabrini, S., Weber-Bargioni, A., *Nano Lett.* **13**, 2687-2691 (2013).

[145] Wang, Y., Abb, M., Boden, S. A., Aizpurua, J., de Groot, C. H., Muskens, O. L., *Nano Lett.* **13**, 5647-5653 (2013).

[146] Kim, Z. H., Leone, S. R.,*Opt. Express* **16**, 1733-1741 (2008).

[147] Maier, S. A., *Opt. Quantum Electron.* **38**, 257-267 (2006).

[148] Novotny, L., van Hulst, N., *Nat. Photon.* **5**, 83-90 (2011).

[149] Soukoulis, C. M., Wegener, M., *Nat. Photon.* **5**, 523-530 (2011).

[150] Kildishev, A. V., Boltasseva, A., Shalaev, V. M., *Science* **339**, 1232009 (2013).

[151] Tang, L., Kocabas, S. E., Latif, S., Okyay, A. K., Ly-Gagnon, D. S., Saraswat, K. C., Miller, D. A. B., *Nat. Photon.* **2**, 226-229 (2008).

[152] Pendry, J. B., *Phys. Rev. Lett.* **85**, 3966-3969 (2000).

[153] Shalaev, V. M., *Nat. Photon.* **5**, 41-48 (2007).

[154] Landy, N. I., Sajuyigbe, S., Mock, J. J., Smith, D. R., Padilla, W. J., *Phys. Rev. Lett.* **100**, 207402 (2008).

[155] Valev, V. K., Baumberg, J. J., Sibilia, C., Verbiest, T., *Adv. Mater.* **25**, 2517-2534 (2013).

[156] Papakostas, A., Potts, A., Bagnall, D. M., Prosvirnin, S. L., Coles, H. J., Zheludev, N. I., *Phys. Rev. Lett.* **90**, 107404 (2003).

[157] Vallius, T., Jefimovs, K., Turunen, J., Vahimaa, P., Svirko, Y., *Appl. Phys. Lett.* **83**, 234-236 (2003).

[158] Plum, E., Fedotov, V. A., Schwanecke, A. S., Zheludev, N. I., Chen, Y., *Appl. Phys. Lett.* **90**, 223113 (2007).

[159] Decker, M., Klein, M. W., Wegener, M., Linden, S., *Opt. Lett.* **32**, 856-858 (2007).

[160] Plum, E., Zhou, J., Dong, J., Fedotov, V. A., Koschny, T., Soukoulis, C. M., Zheludev, N. I., *Phys. Rev. B: Condens. Matter Mater. Phys.* **79**, 035407 (2009).

[161] Gansel, J. K., Thiel, M., Rill, M. S., Decker, M., Bade, K., Saile, V., von Freymann, G., Linden, S., Wegener, M., *Science* **325**, 1513-1515 (2009).

[162] Wang, B., Zhou, J., Koschny, T., Kafesaki, M., Soukoulis, C. M., *J. Opt. A: Pure Appl. Opt.* **11**, 114003 (2009).

[163] Liu, N., Liu, H., Zhu, S., Giessen, H., *Nat. Photon.* **3**, 157-162 (2009).

[164] Zhang, S., Park, Y.-S., Li, J., Lu, X., Zhang, W., Zhang, X., *Phys. Rev. Lett.* **102**, 023901 (2009).

[165] Hendry, E., Carpy, T., Johnston, J., Popland, M., Mikhaylovskiy, R. V., Lapthorn, A. J., Kelly, S. M., Barron, L. D., Gadegaard, N., Kadodwala, M., *Nat. Nanotechnol.* **5**, 783-787 (2010).

[166] Zhao, Y., Belkin, M. A., Alù, A., *Nat. Commun.* **3**, 870 (2012).

[167] Wu, C., Arju, N., Kelp, G., Fan, J. A., Dominguez, J., Gonzales, E., Tutuc, E., Brener, I., Shvets, G., *Nat. Commun.* **5**, 3892 (2014).

[168] Pendry, J. B., *Science* **306**, 1353-1355 (2004).

[169] Kwon, D.-H., Werner, P. L., Werner, D. H., *Opt. Express* **16**, 11802-11807 (2008).

[170] Schäferling, M., Dregely, D., Hentschel, M., Giessen, H., *Phys. Rev. X* **2**, 031010 (2012).

[171] Tang, Y., Cohen, A. E., *Phys. Rev. Lett.* **104**, 163901 (2010).

[172] Grossman, E. N., Sauvageau, J. E., McDonald, D. G., *Appl. Phys. Lett.* **59**, 3225-3227 (1991).

[173] Fumeaux, C., Boreman, G. D., Herrmann, W., Rothuizen, H., Kneubühl, F. K., *Appl. Opt.* **36**, 6485-6490 (1997).

[174] González, F. J., Boreman, G. D., *Infrared Phys. Technol.* **46**, 418-428 (2005).

[175] Ziegler, J. I., Haglund, R. F., *Nano Lett.* **10**, 3013-3018 (2010).

[176] Zhao, Y., Alù, A, *Phys. Rev. B: Condens. Matter Mater. Phys.* **84**, 205428 (2011).

[177] Khanikaev, A. B., Arju N., Fan, Z., Purtseladze, D., Lu, F., Lee, J., Sarriugarte, P., Schnell, M., Hillenbrand, R., Belkin, M. A., Shvets, G., *Nat. Commun.* **7**, 12045 (2016).

[178] Khanikaev, A. B., Mousavi, S. H., Wu, C., Dabidian, N., Alici, K. B., Shvets, G., *Opt. Commun.* **285**, 3423-3427 (2012).

[179] Fedotov, V. A., Schwanecke, A. S., Zheludev, N. I., Khardikov, V. V., Prosvirnin, S. L., *Nano Lett.* **7**, 1996-1999 (2007).

[180] Arju, N., Ma, T., Khanikaev, A., Purtseladze, D., Shvets, G., *Phys. Rev. Lett.* **114**, 237403 (2015).

[181] Takahashi, S., Potts, A., Bagnall, D., Zheludev, N. I., Zayats, A. V., *Opt. Commun.* **255**, 91-96 (2005).

[182] Narushima, T., Okamoto, H., *Phys. Chem. Chem. Phys.* **15**, 13805-13809 (2013).

[183] Narushima, T., Okamoto, H., *J. Phys. Chem. C* **117**, 23964-23969 (2013).

[184] Ohno, T., Miyanishi, S., *Opt. Express* **14**, 6285-6290 (2006).

[185] Drezet, A., Genet, C., Laluet, J.-Y., Ebbesen, T. W., *Opt. Express* **16**, 12559-12570 (2008).

[186] Gorodetski, Y., Niv, A., Kleiner, V., Hasman, E., *Phys. Rev. Lett.* **101**, 043903 (2008).

[187] Chen, W., Abeysinghe, D. C., Nelson, R. L., Zhan, Q., *Nano Lett.* **10**, 2075-2079 (2010).